Geofluids

Inorganic Pollutants into Groundwater: From Geochemistry to Treatment

Lead Guest Editor: Carmine Apollaro
Guest Editors: Alberto Figoli, Ilaria Fuoco, and Alessandra Criscuoli

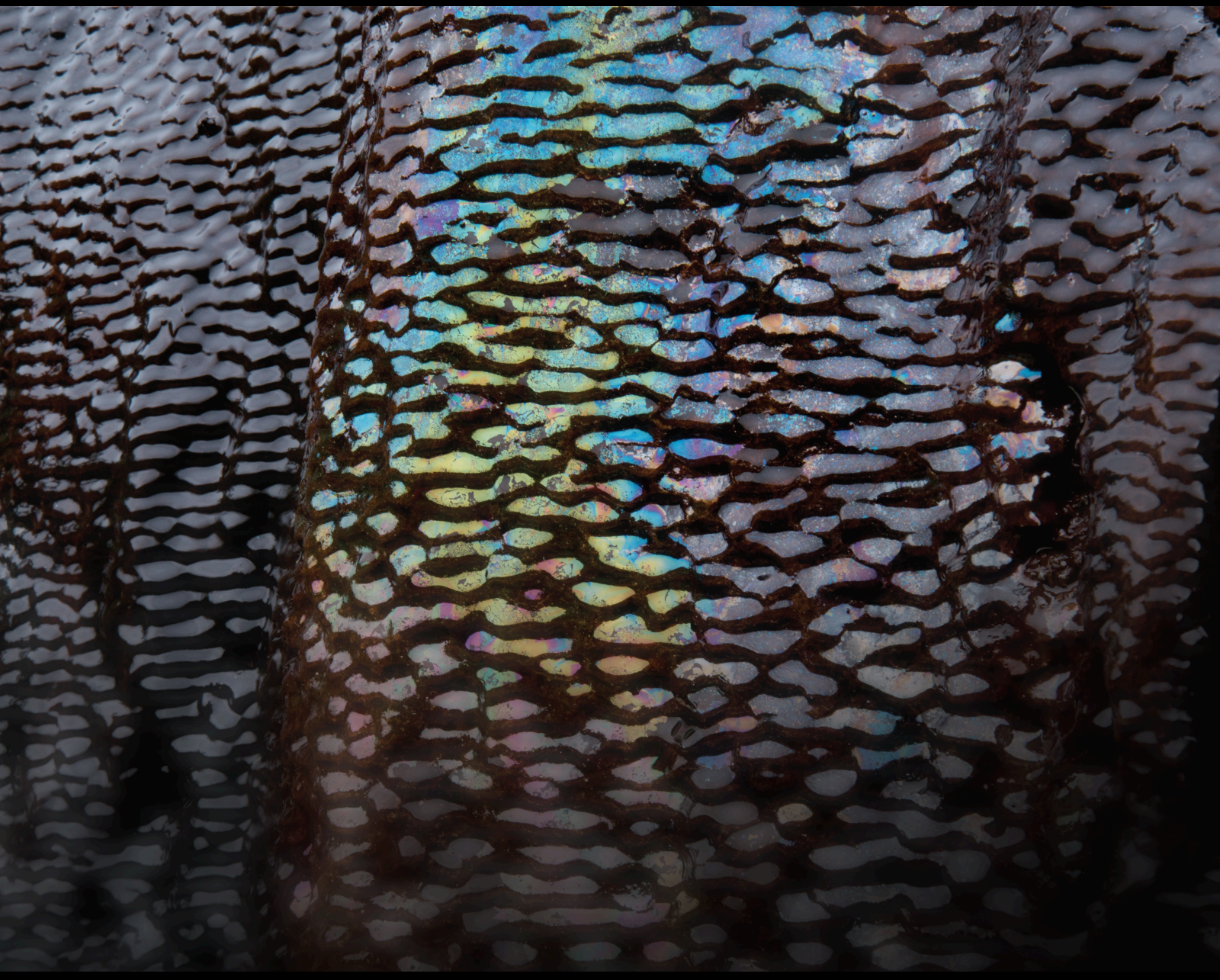

Inorganic Pollutants into Groundwater: From Geochemistry to Treatment

Geofluids

Inorganic Pollutants into Groundwater: From Geochemistry to Treatment

Lead Guest Editor: Carmine Apollaro
Guest Editors: Alberto Figoli, Ilaria Fuoco, and Alessandra Criscuoli

Contents

Hindawi
Geofluids
Volume 2022, Article ID 9846802, 3 pages
https://doi.org/10.1155/2022/9846802

Editorial

Inorganic Pollutants into Groundwater: From Geochemistry to Treatment

Carmine Apollaro,[1] **Ilaria Fuoco**,[1] **Alessandra Criscuoli**,[2] **and Alberto Figoli**[2]

[1]*Department of Biology, Ecology and Earth Sciences (DIBEST), University of Calabria, Via P. Bucci 15/B, 87036 Rende, Italy*
[2]*Institute on Membrane Technology (ITM-CNR), Via P. Bucci 17/C, 87036 Rende, Italy*

Correspondence should be addressed to Carmine Apollaro; carmine.apollaro@unical.it

Received 18 March 2022; Accepted 18 March 2022; Published 16 April 2022

Geochemical approaches, including geochemical characterization and/or geochemical modelling of the environment of interest, represent a strong tool to predict the groundwater evolution as well as the release and fate of contaminants into peculiar geological setting [1–4]. Groundwater bodies in specific geologic environments for human activities (i.e., mines, geoparks and nature reserves, agricultural, residential, or industrial areas) have to be investigated in order to ensure a safe management of working, living, and tourist spaces, as well as to ensure the monitoring and protection of water resources and human health [5–9]. Geochemical characterization includes several practices of sampling and analysis types (i.e., analyses of major and trace of inorganic/organic compounds, isotopic and radiometric investigations), whereas geochemical modelling employs several softwares to predict the migration of pollutants in groundwaters [10]. These pollutants can reach high levels into groundwaters which are used for drinking or irrigation purposes worldwide, becoming hazardous for ecosystems and human health [11–16], mostly in developing countries [17]. Their mobility depends on several parameters, first of all the conditions of geochemical environment. Knowledge of natural or anthropogenic factors responsible for water contamination can be useful to develop efficient water remediation systems able to improve the living standards in the investigated environment, optimizing the decontamination process during the application on site [18–21] and achieving the standards of quality established by the World Health Organization (WHO) [22]. Several treatment technologies, both conventional and advanced, were employed to water decontamination, and among them, the membrane processes were considered valid remediation technologies for their multiple benefits [23–26].

For these reasons, the special issue is aimed at collecting methodological and multidisciplinary contributions that include geochemical and remediation approaches, to understand, monitor, and solve contamination issues with special focus on water resources. These studies represent a target tool for a successful policy management of water resources which can be applied by local authorities or can be viewed as guidelines to be applied in other geological setting.

C. Apollaro et al. studied the groundwater bodies of the Pollino National Park sites over northern Calabria and southern Basilicata regions (southern Italy) by using the reaction path modelling of rocks dissolution. Pollino National Park represents a precious resource to be protected and enhanced also by monitoring water bodies, which are essential for the biodiversity conservation.

The main lithotypes cropping out in the study area (i.e., limestone, Mg-limestone, dolomite, serpentinite, Al-silicate fraction of calcschist, and carbonate fraction of calcschist) were taken into account, evaluating the theoretical concentration of main and minor constituents dissolved during the water-rock interaction. The computed evolution trends reproduced satisfactorily the experimental data which are in agreement with the dissolution of pertinent lithotypes. Furthermore, the water-quality check allowed to establish that the detected levels of potential harmful pollutant, like Al, Cl, F, NO_3, and SO_4, are below the limit values fixed by the WHO.

An important aspect of natural/anthropogenic contamination is the level of radioactivity into the environment, since the level of radiation constitutes a potential risk to human health. I. Guagliardi et al. investigated the equivalent dose rate of natural radionuclides (H_T) in several springs and surface soil samples coming from the Crati basin in the Calabria region (Southern Italy). The results pointed out that the highest H_T values were recorded in soil samples originating mainly from igneous-metamorphic rock alteration. Indeed, these rocks are constituted by minerals containing K, U, and Th, which represent naturally occurring radioactive elements. Likewise, the equivalent dose rates of waters well fit the elemental distribution of the same lithologies. The detected equivalent dose, nowadays, not evidence serious health risks, however the long exposure time can represent an hazardous factor for people living in surrounding area.

Geochemical characterization of waters in areas affected by agricultural and industrial activities is part of geochemical application for the groundwater quality assessment and resource management. M. Paternoster et al. investigated the quality of groundwaters in High Agri Valley (Southern Apennines, Italy) studying the chemical features of several springs and wells by coupling the hydrogeochemical investigation with multivariate statistic, saturation calculation, and isotopic information. The latter revealed a meteoric origin, whereas the results of analyses pointed out that the water-rock interaction process is the main factor influencing the water chemistry, except for few samples characterized by high SO_4^{2-}/NO_3 ratio probably due to an anthropogenic input. The results were also compared with threshold values reported by the WHO and the Italian legislation, highlighting that the studied waters are suitable for drinking and irrigation purposes, although the medium to high salinity detected can represent a potential risk for agricultural practices.

The geochemical approach coupled with numerical modelling can be applied in different fields of environmental sciences, including the management of workspaces like mines. For instance, X. Du et al. proposed an environmental evaluation model to create an objective, convenient, and precise tool applicable in coal mines. The model was based on generalized linear theory and fuzzy analytic hierarchy processes. The water quality was considered as an index factor to insert for a proper environment evaluation. Indeed, the generalized linear theory allowed to obtain the importance degree of each index factor like water, air, soil, ecological compensation, and other indexes affecting the quality of these environments. Afterwards, through the logarithmic fuzzy preference programming method, the influence of each considered index factor was accurately calculated, reducing, thus, the impact of subjectivity of the expert evaluator concerning the environmental evaluation of working spaces.

Monitoring of water quality in protected, working, and residential areas is on the basis of a correct water resource management; however, the development of new technologies for water decontamination represents the current challenge worldwide. In this trail, S. H. Ahmed et al. investigated the performance of three polyethersulfone membranes (PES1, PES2, and PES3) to evaluate the rejections of Co^{2+}, Cd^{2+}, and Pb^{2+} ions, which can reach high levels into groundwaters due to water-rock interaction processes and/or anthropogenic inputs. The experiments were performed using binary and ternary solutions containing different pollutant ratios. Co^{2+}, Cd^{2+}, and Pb^{2+} ions were well-rejected in binary solutions when their initial concentration was lower than the initial concentration of the other ion present in the same binary solution. Concerning the ternary solutions, the rejections were higher when the initial level of the pollutant into the solution was lower. Generally, the following rejection tendencies were observed: $Co^{2+} > Cd^{2+} > Pb^{2+}$. Summing up, the research provided satisfactory results concerning the decontamination of solution and the methodology can be applied in the future to solve groundwater pollution issue in areas affected by high levels of these contaminants.

Conflicts of Interest

The guest editors declare that they have no conflict of interest.

Acknowledgments

The guest editors thank all the authors and reviewers for their contributions.

Carmine Apollaro
Ilaria Fuoco
Alessandra Criscuoli
Alberto Figoli

References

[1] I. Fuoco, R. De Rosa, D. Barca, A. Figoli, B. Gabriele, and C. Apollaro, "Arsenic polluted waters: Application of geochemical modelling as a tool to understand the fate of the pollutant in crystalline aquifers," *Journal of Environmental Management*, vol. 301, article 113796, 2021.

[2] K. Toyoda, S. Nakano, S. Tanaka et al., "Geochemical identification of particulate lead pollution in shallow groundwater in inhabited areas in Kabwe, Zambia," *Applied Geochemistry*, vol. 139, article 105215, 2022.

[3] C. Christofi, A. Bruggeman, C. Kuells, and C. Constantinou, "Hydrochemical evolution of groundwater in gabbro of the Troodos Fractured Aquifer. A comprehensive approach," *A Comprehensive Approach. Applied Geochemistry*, vol. 114, article 104524, 2020.

[4] C. A. J. Appelo and D. Postma, *Geochemistry, Groundwater and Pollution*, CRC Press, London, 2004.

[5] C. Wolkersdorfer, D. K. Nordstrom, R. D. Beckie et al., "Guidance for the Integrated Use of Hydrological, Geochemical, and Isotopic Tools in Mining Operations," *Mine Water and the Environment*, vol. 39, no. 2, pp. 204–228, 2020.

[6] K. R. Beisner, J. E. Solder, F. D. Tillman, J. R. Anderson, and R. C. Antweiler, "Geochemical characterization of groundwater evolution south of Grand Canyon, Arizona (USA)," *Hydrogeology Journal*, vol. 28, no. 5, pp. 1615–1633, 2020.

[7] C. Apollaro, D. Di Curzio, I. Fuoco et al., "A multivariate non-parametric approach for estimating probability of exceeding the local natural background level of arsenic in the aquifers of Calabria region (Southern Italy)," *Science of the Total Environment*, vol. 806, Part 1, 2021.

[8] D. Zuzolo, D. Cicchella, A. Demetriades et al., "Arsenic: Geochemical distribution and age-related health risk in Italy," *Environmental Research*, vol. 182, article 109076, 2020.

[9] A. K. Tiwari, S. Orioli, and M. De Maio, "Assessment of groundwater geochemistry and diffusion of hexavalent chromium contamination in an industrial town of Italy," *Journal of Contaminant Hydrology*, vol. 225, article 103503, 2019.

[10] D. Pietrzak, "Modeling migration of organic pollutants in groundwater – Review of available software," *Environmental Modelling & Software*, vol. 144, article 105145, 2021.

[11] Z. Rahman and V. P. Singh, "The relative impact of toxic heavy metals (THMs)(arsenic (As), cadmium (Cd), chromium (Cr)(VI), mercury (Hg), and lead (Pb)) on the total environment: an overview," *Environmental Monitoring and Assessment*, vol. 191, no. 7, pp. 1–21, 2019.

[12] M. Kumar, R. Goswami, A. K. Patel, M. Srivastava, and N. Das, "Scenario, perspectives and mechanism of arsenic and fluoride Co-occurrence in the groundwater: A review," *Chemosphere*, vol. 249, article 126126, 2020.

[13] I. Mukherjee, U. K. Singh, R. P. Singh, D. Kumari, P. K. Jha, and P. Mehta, "Characterization of heavy metal pollution in an anthropogenically and geologically influenced semi-arid region of east India and assessment of ecological and human health risks," *Science of the Total Environment*, vol. 705, article 135801, 2020.

[14] O. Nikolenko, A. Jurado, A. V. Borges, K. Knöller, and S. Brouyère, "Isotopic composition of nitrogen species in groundwater under agricultural areas: a review," *Science of the Total Environment*, vol. 621, pp. 1415–1432, 2018.

[15] K. N. Palansooriya, Y. Yang, Y. F. Tsang et al., "Occurrence of contaminants in drinking water sources and the potential of biochar for water quality improvement: A review," *Critical Reviews in Environmental Science and Technology*, vol. 50, no. 6, pp. 549–611, 2020.

[16] M. Islam, D. Romić, M. Akber, and M. Romić, "Trace metals accumulation in soil irrigated with polluted water and assessment of human health risk from vegetable consumption in Bangladesh," *Environmental Geochemistry and Health*, vol. 40, no. 1, pp. 59–85, 2018.

[17] J. O. Ighalo, A. G. Adeniyi, J. A. Adeniran, and S. Ogunniyi, "A systematic literature analysis of the nature and regional distribution of water pollution sources in Nigeria," *Journal of Cleaner Production*, vol. 283, article 124566, 2021.

[18] I. Fuoco, A. Figoli, A. Criscuoli et al., "Geochemical modeling of chromium release in natural waters and treatment by RO/NF membrane processes," *Chemosphere*, vol. 254, article 126696, 2020.

[19] I. Fuoco, C. Apollaro, A. Criscuoli, R. De Rosa, S. Velizarov, and A. Figoli, "Fluoride Polluted Groundwaters in Calabria Region (Southern Italy): Natural Source and Remediation," *Water*, vol. 13, no. 12, p. 1626, 2021.

[20] A. Figoli, I. Fuoco, C. Apollaro et al., "Arsenic-contaminated groundwaters remediation by nanofiltration," *Separation and Purification Technology*, vol. 238, article 116461, 2020.

[21] S. I. Bouhadjar, H. Kopp, P. Britsch, S. A. Deowan, J. Hoinkis, and J. Bundschuh, "Solar powered nanofiltration for drinking water production from fluoride- containing groundwater - A pilot study towards developing a sustainable and low-cost treatment plant," *Journal of Environmental Management*, vol. 231, pp. 1263–1269, 2019.

[22] WHO, *Guidelines for Drinking-Water Quality: Fourth Edition Incorporating the First Addendum*, World Health Organization, Geneva, 2017.

[23] K. H. Vardhan, P. S. Kumar, and R. C. Panda, "A review on heavy metal pollution, toxicity and remedial measures: Current trends and future perspectives," *Journal of Molecular Liquids*, vol. 290, article 111197, 2019.

[24] S. Bhojwani, K. Topolski, R. Mukherjee, D. Sengupta, and M. M. El-Halwagi, "Technology review and data analysis for cost assessment of water treatment systems," *Science of the Total Environment*, vol. 651, Part 2, pp. 2749–2761, 2019.

[25] A. Yusuf, A. Sodiq, A. Giwa et al., "A review of emerging trends in membrane science and technology for sustainable water treatment," *Journal of Cleaner Production*, vol. 266, article 121867, 2020.

[26] C. Teodosiu, A. F. Gilca, G. Barjoveanu, and S. Fiore, "Emerging pollutants removal through advanced drinking water treatment: A review on processes and environmental performances assessment," *Journal of Cleaner Production*, vol. 197, pp. 1210–1221, 2018.

Hindawi
Geofluids
Volume 2021, Article ID 6664164, 15 pages
https://doi.org/10.1155/2021/6664164

Research Article

Hydrogeochemistry and Groundwater Quality Assessment in the High Agri Valley (Southern Italy)

M. Paternoster,[1,2] **R. Buccione**,[1] **F. Canora**,[3] **D. Buttitta**,[1] **S. Panebianco**,[1,4] **G. Rizzo**,[1] **R. Sinisi**,[4] **V. Summa**,[4] **and G. Mongelli**[1,4]

[1]*Department of Sciences, University of Basilicata, Vialedell'AteneoLucano 10, Campus Macchia Romana, 85100 Potenza, Italy*
[2]*National Institute of Geophysics and Volcanology (INGV), Section of Palermo, 90153 Palermo, Italy*
[3]*School of Engineering, University of Basilicata, Viale dell'Ateneo Lucano 10, Campus Macchia Romana, 85100 Potenza, Italy*
[4]*National Research Council, Institute of Methodologies for Environmental Analysis (CNR-IMAA), 85050 Tito Scalo (PZ), Italy*

Correspondence should be addressed to M. Paternoster; michele.paternoster@unibas.it

Received 22 October 2020; Revised 18 December 2020; Accepted 7 June 2021; Published 25 June 2021

Academic Editor: Orlando Vaselli

The High Agri Valley (southern Italy) is one of the largest intermontane basin of the southern Apennines affected by intensive agricultural and industrial activities. The study of groundwater chemical features provides much important information useful in water resource management. In this study, hydrogeochemical investigations coupled with multivariate statistics, saturation indices, and stable isotope composition (δD and δ^{18}O) were conducted in the High Agri Valley to determine the chemical composition of groundwater and to define the geogenic and anthropogenic influences on groundwater quality. Twenty-four sampling point (including well and spring waters) have been examined. The isotopic data revealed that groundwater has a meteoric origin. Well waters, located on recent alluvial-lacustrine deposits in shallow porous aquifers at the valley floor, are influenced by seasonal rainfall events and show shallow circuits; conversely, spring waters from fissured and/or karstified aquifers are probably associated to deeper and longer hydrogeological circuits. The *R*-mode factor analysis shows that three factors explain 94% of the total variance, and F1 represents the combined effect of dolomite and silicate dissolution to explain most water chemistry. In addition, very low contents of trace elements were detected, and their distribution was principally related to natural input. Only two well waters, used for irrigation use, show critical issue for NO_3^- concentrations, whose values are linked to agricultural activities. Groundwater quality strongly affects the management of water resources, as well as their suitability for domestic, agricultural, and industrial uses. Overall, our results were considered fulfilling the requirements for the inorganic component of the Water Framework Directive and Italian legislation for drinking purposes. The water quality for irrigation is from "good to permissible" to "excellent to good" although salinity and relatively high content of Mg^{2+} can occasionally be critical.

1. Introduction

Groundwater resource is one of the most challenging current and future issues of worldwide concern. The ever-increasing rate of population growth and the inherent water supply demand have led to intensive water exploitation. Groundwater is of great importance for domestic, drinking, irrigation, and industry purposes especially where the water resource is availability scarce. Groundwater quality depends on natural processes such as rock-water interaction, climatic conditions, geological context, and anthropogenic activities. Natural processes including the mineral precipitation or dissolution, ion-exchange, redox condition, residence time, and mixing between different water type may have a great impact on groundwater quality [1]. Anthropogenic activities such as rapid urbanization, industrialization, and intensive agricultural activities have caused a deterioration in water quality worldwide [2–5]. Groundwater contamination can be persisted a long time due to the low flow rate of groundwater in an aquifer and may involve major ions and trace elements [6]. High levels of contaminants, exceeding guideline values, can turn water to be unsuitable for drinking, irrigation, fishing,

and recreation [7], causing serious adverse effects on human and biota health [8]. The release of elements from rocks depends upon physical (temperature, residence time, flow rate) and chemical factors (namely, weathering of rock-forming minerals, precipitation of sparingly soluble secondary minerals, and presence of reactive gas species such as CO_2), i.e., [9, 10]. The redox process can have an important role in determining the partitioning between aqueous solution and solid phases, taking into account that some elements are present in nature in different oxidation states. In southern Apennines (southern Italy), the High Agri Valley (hereafter HAV) is characterized by a relevant presence of intensive agricultural activities in predominantly hilly environment due to the occurrence of groundwater and fertile soils and a unique forest heritage with a rich biodiversity that have stimulated tourism growth. In recent decades, together with an ancient rural economy based on agriculture, wood, and dairy production, new industrial activities have been undertaken. Hydrocarbon extraction, related to the largest onshore oil field in Western Europe, is the most important industrial activity and has actually an oil production capacity of about 80.000 barrels/day [11]. In the HAV, the groundwater represents an important freshwater resource, used as drinking water supply for agricultural and industrial purposes. Usually, the anthropogenic activities influencing groundwater systems contribute to a decrease in water availability, both directly through variations in aquifer recharge and indirectly through changes in groundwater quality and use. The evaluation and management of groundwater resources require an understanding of hydrogeochemical features of the aquifers.

The aim of this research, representing the first step of a comprehensive hydrogeochemical characterization of the area, is to understand the geochemical evolution of groundwater in the HAV in order to guarantee reliable supply for all purposes and define a sustainable groundwater management strategy, also considering the growing industrialization that could cause pollution phenomena. The main objectives are to (1) determine the geochemical processes controlling the chemical composition, (2) define the geogenic and anthropogenic influences on groundwater quality, and (3) compare the concentrations of some inorganic elements to values established by the World Health Organization and the Italian legislation for drinking and irrigation purposes.

2. Climate, Geology, and Hydrogeology

HAV area (Basilicata region, southern Italy) extends for about 140 km^2 and is 30 km long and 12 km wide. According to the Köppen classification, the climate of the area is of warm-summer Mediterranean type, characterized by cold-humid winter and hot-dry summer. In the study area, the mean annual precipitation value (calculated in 2005-2015 range) was of about 1000 mm/y, while the mean annual temperature was of 12.5°C. The coldest month was January with average temperature ranging between 3°C and 4°C. Hot and arid conditions during summer produce periods of drought during July and August. The climate of the area, characterized by high seasonal precipitation rates in autumn and spring and snowy winter, allows the greatest amount of the aquifer recharge. From a geological point of view, HAV is a NW-SE trending Quaternary basin located in the axial zone of the southern Apennines, an east-verging fold-and-thrust belt developed as an accretionary wedge due to the eastward migration of the compressional tectonics in the Apennine Arc (Late Oligocene-Early Pleistocene) [12, 13]. The HAV evolution, since the Middle Pleistocene, is controlled by a still active NE-SW extensional tectonic regime [14], as witnessed by NW striking high-angle normal and oblique faults bordering the basin, which represent the main seismogenic structures in the area [15, 16]. The HAV is characterized by Quaternary continental deposits overlying a Pre-Quaternary substratum (Figure 1(a)). In the south-west side of the basin, the substratum consists of Mesozoic to Cenozoic shallow-water and slope carbonates of the Campania–Lucania Platform over thrusted on coeval pelagic successions (Lagonegro Units), while to south-east the substratum is characterized by Tertiary siliciclastic sediments of the Gorgoglione Flysch and Albidona Formation [13, 17]. A Quaternary synorogenic succession, consisting of Lower Pleistocene-Holocene continental clastic sediments, mainly coarse-grained, fills the HAV basin [18] and references therein. Finally, the most recent Pleistocene and Holocene deposits are represented by terraced alluvium, alluvial fans, and recent to present-day alluvial sediments (Figure 1(a)).

The HAV hydrogeology is characterized by a high groundwater content favoured by climate conditions. Two different kinds of aquifers are recognized: fissured and/or karstified aquifers in the Apennine units of the substratum and porous multilayer aquifers developed in the Quaternary succession [19]. Both types host high volumes of groundwater storage, with the richest amount located in Pre-Quaternary substratum aquifers usually subdivided in different hydrogeological complexes according to the structural, lithological, and permeability features [20]. These aquifers mainly occur in highly fractured limestones (Carbonate Platform) and in the underlying "Calcari con Selce" Fm (Lagonegro Units), both characterized by high permeability (Figure 1(b)). Porous aquifers occur in gravelly-sandy permeable deposits of the Quaternary succession [21], where the larger groundwater body is recognized in a multilayered and semiconfined aquifer. Carbonate karst and fractured aquifers play a leading role in the overall hydrogeological system, since their groundwater resources supply the detrital-alluvial ones occurring at the valley bottom. Finally, most springs from HAV, generally showing an average flow rate greater than 5 l/s, are at the contact between permeable limestone and dolostone (Lagonegro Units and Carbonate Platform) and impermeable Plio-Pleistocene siliciclastic and recent alluvial-lacustrine deposits [22].

3. Materials and Methods

3.1. Sampling and Analyses. Twenty-four water samples were collected during a single survey carried out between March and April 2016 in the HAV. Nine of them were taken from springs of the fissured and/or karstified aquifers located on Pre-Quaternary carbonate rocks and sediments belonging to the Lagonegro Units and fifteen from wells on recent alluvial-lacustrine deposits in shallow porous aquifers at the valley floor with a phreatic level ranging from 1 to 6 meters

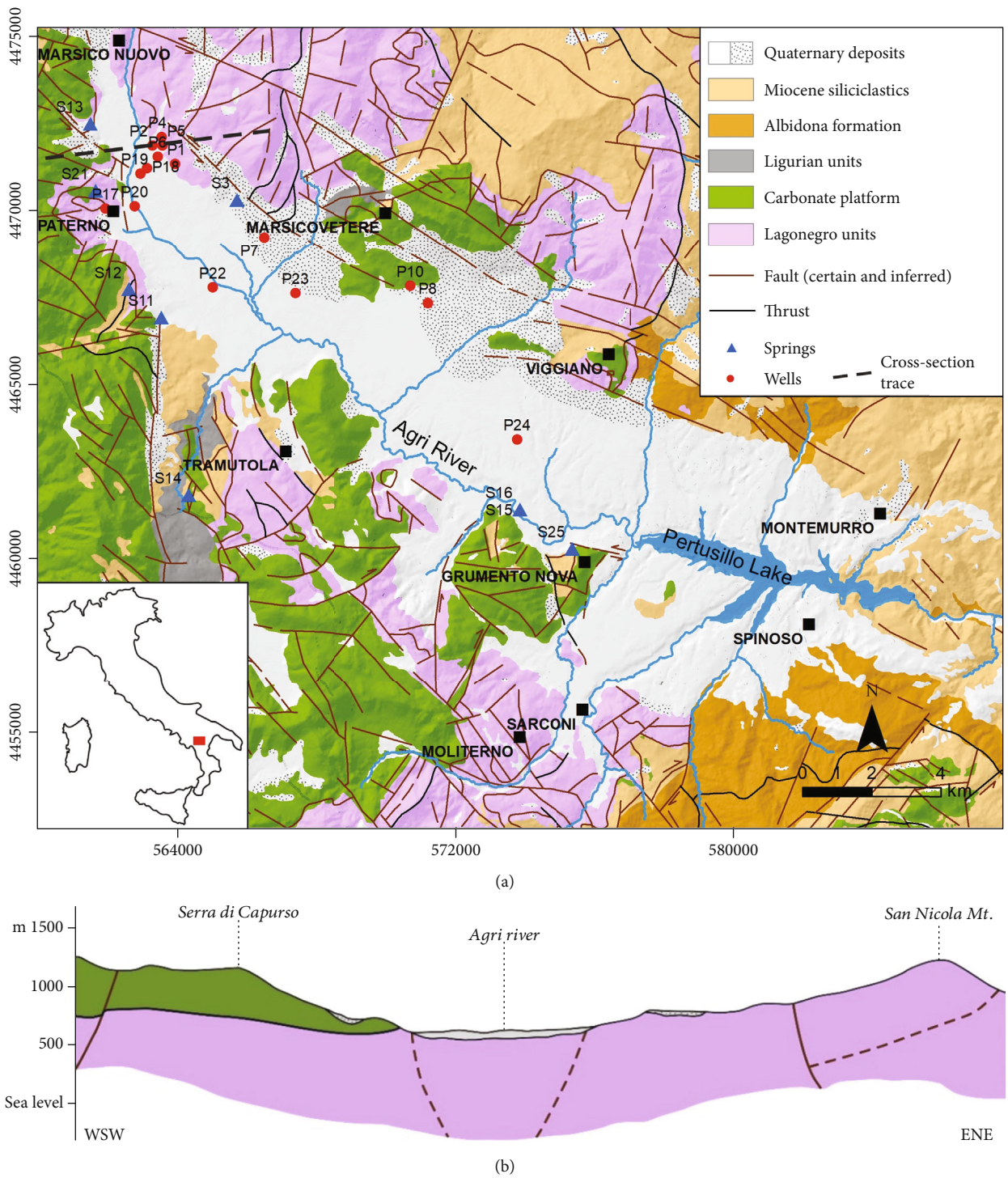

Figure 1: Geological sketch map (a) of the investigated area (modified after Giocoli et al. [15]) where localization of the sampling sites (springs and wells) is displayed. Schematic cross section (b) of the northern part of study area is drawn (modified after Carbone et al. [17]).

from the surface (Figure 1). The investigated springs are located on the right bank of the Agri River, except for S3 site, in the left river side. Most of springs, managed by the Acquedotto Lucano public agency, are used for drinking purposes, whereas well waters, mostly belonging to private individuals, are used for irrigation purposes. Temperature, pH, electric conductivity (EC, measured at 25°C), and redox potential (Eh) were measured in situ using a high-resolution multiparametric probes (Hanna Instruments HI-9828), after calibration in the laboratory by means PTB/NIST traceable standard solutions. Total alkalinity was determined in situ by titrating unfiltered samples with 0.01 N HCl, and methyl-orange was indicator. All water samples were filtered in situ at 0.45 μm membrane (MF-Millipore) and then stored in low-density

Table 1: Location (latitude and longitude by WGS84-33T), water type (W: well; S: spring), physico-chemical parameters (T, pH, Eh, TDS), major elements (from Ca^{2+} to HCO_3^-), and irrigation quality parameters (SAR, MAR, %Na, RSBC, PI) of the investigated groundwaters. Spring water is from fissured and/or karstified aquifer, while well waters from shallow porous aquifer.

ID	Lat.	Long.	Type	T °C	pH	EC μS/cm	Eh mV	TDS mg/l	Na^+ mg/l	K^+ mg/l	Ca^{2+} mg/l	Mg^{2+} mg/l	SiO_2 mg/l	Cl- mg/l	NO_3^- mg/l	NO_2^- mg/l	SO_4^{2-} mg/l	HCO_3^- mg/l	IB %	SAR meq/l	MAR %	Na %	RSBC meq/l	PI %
P1	563935	4471312	W	21	6.51	837	720	647	8.5		5.4	107	9.7	10.8	3.7	b.d.l.	14.7	488	4.1	0.2	97.0	3.9	7.7	34.0
P2	563284	4471850	W	16.5	6.8	681	760	585	9.0		12.2	91	10.6	9.1	b.d.l.	b.d.l.	26.4	427	4.1	0.2	92.5	4.6	6.4	35.9
P4	563554	4472085	W	15	7.05	522	783	434	7.9		9.7	63	8.0	7.0	b.d.l.	b.d.l.	34.0	305	0.8	0.2	91.4	5.7	4.5	43.0
P5	563572	4471846	W	19.5	6.75	869	800	812	32.8		17.8	108	14.3	32.4	58	b.d.l.	47.3	502	0.5	0.6	90.9	12.8	7.3	38.4
P6	563444	4471523	W	20	6.82	710	750	631	13.7	1.6	13.3	96	12.0	13.4	3.4	b.d.l.	40.4	439	4.0	0.3	92.2	6.9	6.5	35.9
P7	566491	4469202	W	18.5	7.05	1000	752	748	25.3	16.5	20.8	100	17.1	26.9	203	b.d.l.	61.7	293	1.3	0.5	88.8	14.1	3.8	31.7
P8	571209	4467296	W	16.5	6.95	620	770	541	7.1	1.4	11.6	82	17.3	7.9	21.0	b.d.l.	16.7	378	3.6	0.2	92.1	4.5	5.6	36.8
P10	570710	4467800	W	16.4	6.79	578	722	481	14.8	1.7	12.1	68	14.5	12.6	13.4	b.d.l.	16.0	329	4.6	0.4	90.3	9.9	4.8	43.2
P17	561946	4470037	W	19	6.9	617	755	538	10.4		18.3	77	16.4	11.9	7.5	b.d.l.	6.8	390	4.6	0.2	87.3	5.9	5.5	38.9
P18	563128	4471200	W	16.6	6.32	770	370	657	16.1	1.7	16.4	90	22.3	15.3	b.d.l.	b.d.l.	45.7	451	1.1	0.3	90.1	8.3	6.6	38.3
P19	562941	4471047	W	22.7	6.79	579	483	499	7.4	1.13	19.0	68	9.1	8.0	b.d.l.	b.d.l.	9.5	378	2.0	0.2	85.6	5.1	5.3	40.8
P20	562786	4470103	W	18.2	6.45	453	530	385	8.1	6.1	18.2	49	9.6	10.3	19.6	b.d.l.	13.8	256	3.4	0.2	81.7	9.3	3.3	45.3
P22	565018	4467747	W	18.4	7.05	566	240	504	21.0		25.2	57	13.7	6.9	b.d.l.	b.d.l.	2.8	378	3.0	0.5	78.8	13.3	4.9	49.7
P23	567389	4467585	W	19.4	6.86	765	668	679	10.6	1.1	25.7	96	10.7	8.5	3.6	b.d.l.	24.1	500	3.6	0.2	86.0	5.1	6.9	34.5
P24	573780	4463398	W	16.5	6.91	577	570	511	20.8		11.5	67	15.3	8.6	3.7	b.d.l.	6.8	378	2.4	0.5	90.6	13.0	5.6	48.7
S3	565710	4470285	S	18	7.39	365	730	330	5.3	1.1	7.8	51	6.9	6.6	2.2	b.d.l.	6.8	244	5.1	0.2	91.5	5.3	3.6	46.4
S11	563543	4466886	S	11.5	7.3	317	680	303	3.2		11.9	44	4.7	4.5	b.d.l.	b.d.l.	3.4	232	4.0	0.1	85.8	3.2	3.2	48.2
S12	562611	4467695	S	12	7.1	340	760	305	3.2		9.6	46	4.7	4.2	2.5	b.d.l.	3.5	232	4.5	0.1	88.8	3.2	3.3	47.4
S13	561505	4472467	S	11.3	7.13	346	750	307	3.7		11.0	45	5.9	5.0	b.d.l.	b.d.l.	4.2	232	4.8	0.1	87.1	3.6	3.2	47.6
S14	564327	4461796	S	11	7.11	388	675	340	3.4		14.6	49	5.2	5.1	3.4	b.d.l.	3.4	256	4.6	0.1	84.7	3.0	3.5	44.8
S15	573856	4461380	S	14.1	6.87	560	774	473	7.3	1.8	18.6	64	8.8	8.1	5.2	b.d.l.	6.9	354	2.1	0.2	85.0	5.5	4.9	41.8
S16	573856	4461380	S	16.2	7.06	500	790	424	6.3		16.1	60	8.5	6.9	4.2	b.d.l.	5.9	317	3.4	0.2	85.9	4.6	4.4	42.7
S21	561657	4470549	S	14	6.76	442	738	435	14.4	1.36	18.5	55	10.5	6.9	2.4	b.d.l.	9.6	317	3.9	0.4	83.1	10.8	4.3	47.8
S25	575348	4460258	S	13.5	6.7	585	732	484	9.9	3.17	15.9	64	11.1	9.8	10.2	b.d.l.	9.0	354	0.8	0.2	87.0	7.8	5.0	43.5
d.l.									0.9	1.0	0.5	0.6	3.0	1.6	1.9	0.9	1.5	n.d.						

EC: electrical conductivity measured at 25°C; T: temperature; Eh: redox potential; TDS: total dissolved solid; d.l.: detection limit; b.d.l.: below detection limit; IB: ionic balance; SAR: sodium adsorption ratio by Richards [26]; MAR: magnesium adsorption ratio by Raghunath [27]; %Na: sodium percentage by Todd and Mays [28]; RSBC: residual sodium bicarbonate by Gupta and Gupta [29]; PI: permeability index by Ragunath [27].

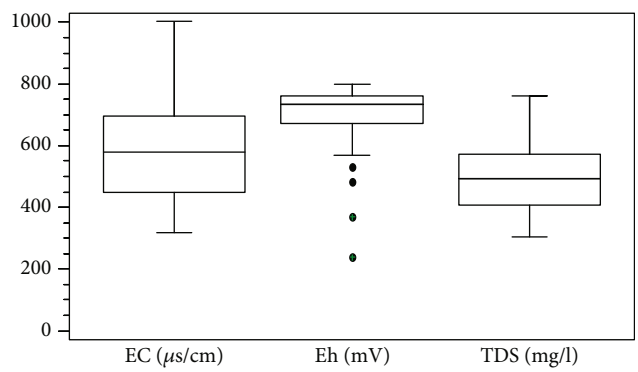

Figure 2: Box-and-whisker plots of physico-chemical parameters.

polyethylene bottles (50 and 100 ml). The bottles were filled to the top with water, capped without leaving any headspace, stored in a refrigerated container (about 4°C) during transportation to the laboratory, and then kept cool until analysis. At each sampling point, one water sample (for cation and trace elements) was collected and acidified in situ with suprapure HNO_3; a second filtered nonacidified sample was collected for anion analysis. Major anions (Cl^-, NO_3^-, NO_2^-, and SO_4^{2-}) and cations (Na^+, K^+, Mg^{2+}, and Ca^{2+}) were determined by ionic chromatography. Minor and trace elements (Li, B, Rb, Sr, Ba, V, and Cu) were determined by inductively coupled plasma–optical emission spectroscopy (ICP-OES). All trace element determinations were performed with the external standard calibration method, using NIST and SLRS standard reference materials for calibration. The precision of the analytical results was estimated by running triplicate analyses every ten samples. Uncertainty of measurements was ≤5-7% for all trace elements. Dissolved SiO_2 was measured by VIS spectrophotometry upon reaction with ammonium molybdate in acid media (and treatment with oxalic acid) to form a yellow silicomolybdate complex, whose absorbance was read at 410 nm [23]. Major element analyses were performed at the Analytical Chemical laboratory of the University of Basilicata; trace elements were determined using a Thermo Scientific™ iCAP™ 7200 at Gaudianello Company laboratory. The oxygen and hydrogen isotopic compositions were analysed at National Institute of Geophysical and Volcanology (INGV, Palermo, Italy) on unfiltered water samples using Analytical Precision AP 2003 and Finnigan MAT Delta Plus IRMS devices, respectively. The isotopic ratios are expressed as the deviation per mil (δ‰) from the reference V-SMOW. The uncertainties 1σ were ±0.1% for $\delta^{18}O$ and ±1% for δD.

3.2. Geochemical Modeling. The Geochemist's Workbench software (GWB 8.0, [24]), implemented with the Thermoddem database [25], was used to calculate saturation indices (SI) for the main mineral phases presents in the aquifer and the construction of activity diagrams. Saturation indices (SI) are defined as SI = log (IAP/Kt), where IAP is the ion activity product of the mineral–water reaction and Kt is the thermodynamic equilibrium constant at the measured temperature. Thus, SI = 0 indicates a thermodynamic equilibrium state, and values > 0 denote oversaturation and <0 undersaturation.

3.3. Irrigation Quality Parameters. In order to determine the suitability of the investigated groundwater for irrigation purposes, the following parameters were evaluated:

(i) The sodium adsorption ratio (SAR), by Richards [26]:

$$SAR = \frac{Na^+}{\sqrt{Ca^{2+} + Mg^{2+}/2}} \quad (1)$$

(ii) The magnesium adsorption ratio (MAR), by Raghunath [27]:

$$MAR = \frac{Mg^{2+}}{\left(Ca^{2+}Mg^{2+}\right)} * 100 \quad (2)$$

(iii) The sodium percentage (%Na), by Todd and Mays [28]:

$$\%Na = \frac{\left(Na^+ + K^+\right)}{\left(Ca^{2+} + Mg^{2+} + Na^+ + K^+\right.} * 100 \quad (3)$$

(iv) The residual sodium bicarbonate (RSBC), by Gupta and Gupta [29]:

$$RSCB = \left(HCO3^- - Ca^{2+}\right) \quad (4)$$

(v) The permeability index (PI), by Raghunath [27]:

$$PI = \frac{\left(Na^+ + \sqrt{HCO3^-}\right)}{\left(Ca^{2+} + Mg^{2+} + Na^+\right)} * 100 \quad (5)$$

where concentrations are expressed in meq/l.

4. Results

Temperature, pH, EC, Eh, and the total dissolved solids (hereafter TDS) and major elements are listed in Table 1 together with the geographical coordinates of the sampling points. The EC, Eh, and TDS box-and-whisker plots are shown in Figure 2. Temperatures were between 11 and 22.7°C, and overall water samples had nearly neutral pH-values. EC values ranged from 317 to 1000 μS/cm (average 583 ± 179 μS/cm). Eh values were positive (average 679 ± 142 mV). Finally, TDS ranged from 302 mg/l to 812 mg/l (average 502 ± 139 mg/l).

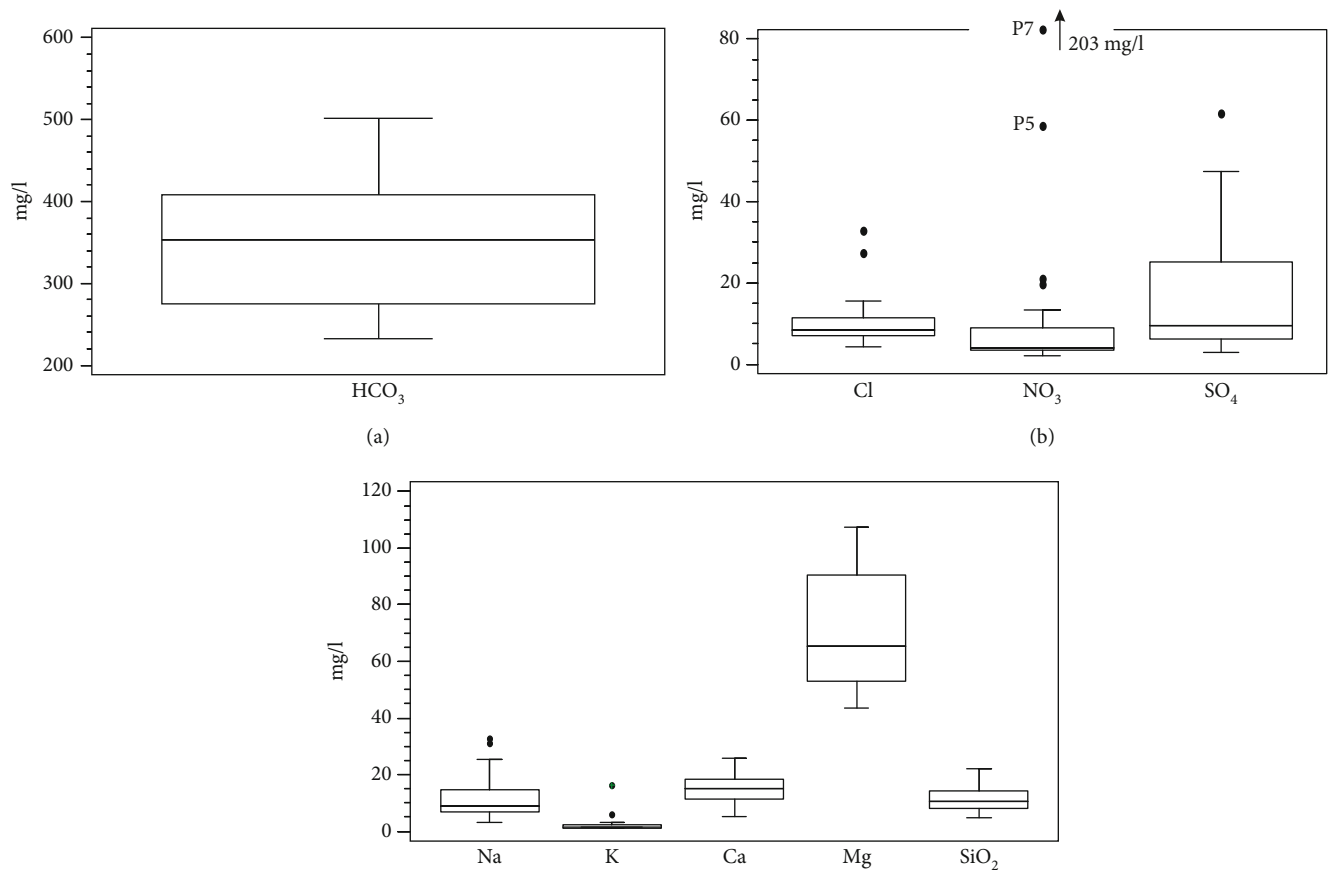

Figure 3: Box-and-whisker plots for major elements (cations and anions).

Box-and-whisker plots of the major constituents (cations and anions) are given in Figure 3.

Sulphates and magnesium count the greatest concentration variations. Among cations, Mg^{2+} is the most abundant (average 70.6 ± 20.6 mg/l), followed by Ca^{2+} (average 15 ± 5.1 mg/l), Na^{+} (11.3 ± 7.5 mg/l), and SiO_2 (11.1 ± 4.5 mg/l). K^{+} values are generally low, ranging from below instrumental detection limit (1.0 mg/l) to 3.2 mg/l, except for P7 sample having the highest value (16.5 mg/l). Bicarbonate is the main anion in solution with concentrations ranging between 232 and 502 mg/l, with an average value of 351.2 ± 86.5 mg/l. Sulphate contents are highly variable and range between 2.8 and 61.7 mg/l with an average value of 17.5 ± 16.6 mg/l. Cl^{-} concentrations are low with an average value of 10.3 ± 6.6 mg/l. Most of the investigated water samples have low NO_3^{-} contents ranging from below instrumental detection limit (1.9 mg/l) to 13.4 mg/l. Only 4 water samples, belonging to shallow porous aquifer, are outliers with NO_3 values ranging between 19.6 and 203 mg/l (P20, P8, P5, and P7 samples, respectively) (Figure 3). Trace element concentrations (Li, B, Rb, Sr, Ba, V, and Cu) are provided in Table 2, together with isotopic data and saturation indices of calcite, dolomite, anorthite, and albite.

V and Cu are characterized by very low contents and in many cases are below the detection limit (b.d.l.: 0.2 and 0.4 μg/l, respectively). Consequently, these elements will not be further included and treated in the discussion. Li and Rb are detected in most samples with values between b.d.l. and 21.2 μg/l and b.d.l. and 4.2 μg/l, respectively. Sr, B, and Ba are detected in all samples. Sr shows the greatest concentration variations from 35.2 to 593.6 μg/l, and some outliers are observed (Figure 4). B concentrations are from 3.8 to 66.1 μg/l while Ba values range from 4.9 to 123 μg/l.

Based on the Piper diagram, the investigated waters show a homogenous distribution with bicarbonate alkaline-earth composition (Figure 5).

Another useful index for water classification is Ionic Salinity or Total Ionic Salinity (TIS) that shows the sum of anion and cation total, expressed in meq/l [30]. Iso-TIS lines are reported in Figure 6 (SO_4^{2-} vs. $HCO_3^{-} + Cl^{-}$) where HAV waters falling in the 8 to 20 meq/l range because of their similar features.

The investigated waters showed $\delta^{18}O$ values between -7.2 and -8.9 ‰ and those of δD from -44 to -53 ‰. The waters from the karst and fissured aquifers generally showed more negative isotopic values (down to −8.9 and−53‰) than waters hosted by shallow porous aquifers, the latter displaying a wide range of variation, from −8.5 to −7.2‰ and from −44 to−52‰ for $\delta^{18}O$ and $\delta^{2}H$, respectively.

5. Discussion

5.1. Interelemental Relationships and Geochemical Processes. A *R*-mode factor analysis was performed to evaluate interelement relationships among some chemical-physical parameters (T and pH), major ions (Na^{+}, Ca^{2+}, Mg^{2+}, SO_4^{2-}, HCO_3^{-}), and

Table 2: Concentrations of selected minor elements, isotopic data, and saturation index (SI) in HAV groundwaters.

Sample	Li μg/l	B μg/l	Rb μg/l	Sr μg/l	Ba μg/l	V μg/l	Cu μg/l	$\delta^{18}O$ ‰ vs. V-SMOW	δD ‰ vs. V-SMOW	SI-calcite Log Q/K	SI-dolomite Log Q/K	SI-albite Log Q/K	SI-anortite Log Q/K
P1	1.9	10.5	b.d.l.	433	20.3	b.d.l.	1.2	-8.1	-46	-1.7	-1.0	-3.9	-11.1
P2	0.9	16.0	0.2	289	9.1	b.d.l.	b.d.l.	-8.3	-49	-1.1	-0.3	-1.7	-6.9
P4	b.d.l.	25.5	0.3	267	10.7	b.d.l.	0.4	-8.4	-52	-1.1	-0.2	-3.5	-10.4
P5	6.0	44.2	0.9	567	15.8	0.4	6.9	-7.8	-44	-0.9	0.0	-2.6	-10.0
P6	1.1	32.1	0.6	351	13.5	0.4	4.2	-8.0	-47	-1.0	0.0	-3.2	-10.3
P7	2.4	41.7	4.2	594	34.5	2.8	10.8	-8.4	-49	-0.7	0.3	-2.4	-9.6
P8	3.4	17.3	b.d.l.	245	37.8	0.2	0.4	-7.2	-46	-1.0	-0.1	-2.7	-9.8
P10	6.7	32.8	0.5	225	34.1	0.4	b.d.l.	-8.1	-51	-1.2	-0.6	-0.4	-5.3
P17	8.7	22.8	0.3	194	19.6	b.d.l.	2.6	-7.9	-47	-0.8	0.1	-2.9	-9.8
P18	2.1	17.4	2.0	367	20.8	b.d.l.	b.d.l.	-7.9	-48	-1.6	-1.4	-2.1	-10.1
P19	b.d.l.	15.6	0.3	204	18.7	b.d.l.	1.8	-8.0	-47	-1.6	-0.1	-4.1	-10.5
P20	b.d.l.	17.7	1.9	74	27.0	0.3	b.d.l.	-7.9	-48	-0.5	-1.6	-3.8	-10.6
P22	5.9	54.3	0.2	278	33.9	b.d.l.	1.7	-7.7	-46	-0.6	0.5	-2.7	-9.7
P23	2.9	33.9	0.5	490	89	b.d.l.	1.8	-7.8	-46	-1.0	0.4	-3.5	-10.0
P24	3.2	42.2	b.d.l.	379	123	b.d.l.	0.1	-8.5	-50	-0.8	-0.2	0.4	-4.1
S3	2.4	15.6	0.9	265	10.3	0.4	1.5	-8.9	-53	-0.8	0.3	-4.1	-10.6
S11	b.d.l.	4.7	0.8	43	6.8	1.0	b.d.l.	-8.7	-50	-1.1	0.0	-4.3	-10.4
S12	b.d.l.	b.d.l.	0.4	35	4.9	1.0	b.d.l.	-8.7	-51	-1.0	-0.5	-4.3	-10.6
S13	b.d.l.	3.8	1.1	54	8.2	0.6	b.d.l.	-8.9	-53	-0.9	-0.4	-3.9	-10.3
S14	b.d.l.	5.8	1.0	49	8.3	1.2	b.d.l.	-8.3	-49	-0.9	-0.3	-2.6	-7.4
S15	2.0	19.5	1.0	147	18.9	1.2	3.9	-7.9	-47	-0.8	-0.3	-3.4	-10.1
S16	1.3	13.9	0.8	123	15.4	1.3	0.4	-8.1	-47	-0.9	0.1	-3.7	-10.1
S21	21.2	66.1	1.0	204	45	b.d.l.	b.d.l.	-8.2	-48	-1.1	-0.7	-2.9	-10.0
S25	3.3	22.9	0.9	234	23.4	0.4	b.d.l.	-8.0	-49	-1.2	-0.8	-3.0	-10.1
d.l.	1.0	5.0	0.2	10.0	2.0	0.2	0.4						

d.l.: detection limit; b.d.l.: below detection limit.

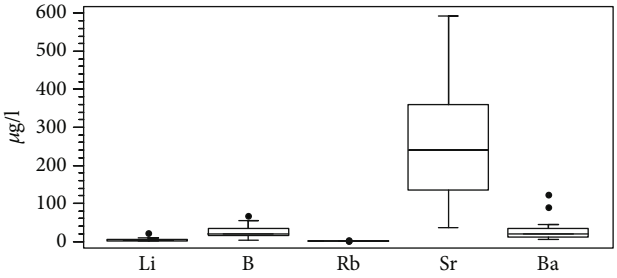

Figure 4: Box-and-whisker plot of selected trace elements.

selected trace elements (Sr, Ba, B). Factors were extracted after varimax rotation using the STATGRAPHICS 18 package. This operation was performed using a standardized correlation matrix, classical type of factoring, thereby equally weighting all the variables during factor calculations. The communalities provide an index of the efficiency of the proposed set of factors [31], and the magnitude of the communalities calculated in this study suggests that most of the original variance is still accounted for by the present set of factors. Three factors explain 94% of the total variance in the selected database (Table 3).

Usually, in terrains where the carbonate lithological facies is dominated by the occurrence of dolomite, the bicarbonate alkaline-earth hydrofacies, with higher Mg^{2+} values than Ca^{2+} one, can be ascribed to dolomite dissolution. It is well known that the dissolution of dolomite can be expressed as follows:

$$CaMg(CO_3)_2 + 2H_2O + 2CO_2 \longrightarrow Ca^{2+} + Mg^{2+} + 4HCO_3^- \quad (6)$$

and the water-dolomite interaction should release equally charged amounts of $Ca^{2+} + Mg^{2+}$ and HCO_3^-, with a $(Ca^{2+} + Mg^{2+}/HCO_3^-)$ ratio close to 1.

Accordingly, in our case, the correlation between $(Ca^{2+}+Mg^{2+}$and $HCO_3^-)$ is highly significant ($r = 0.86$, p value < 0.001, Figure 7). Only P7 sample falls away from general trend, maybe because of its anthropogenic component (see discussion below). However, both the $(Ca^{2+}+Mg^{2+}/HCO_3^-)$ and Mg^{2+}/Ca^{2+} ratios, as meq/l, are above 1, claiming for additional source(s) of Mg^{2+} in groundwater, as also suggested by the finding that several samples are oversaturated with respect to dolomite or close to the SI = 0 value (Table 2, Figure 8).

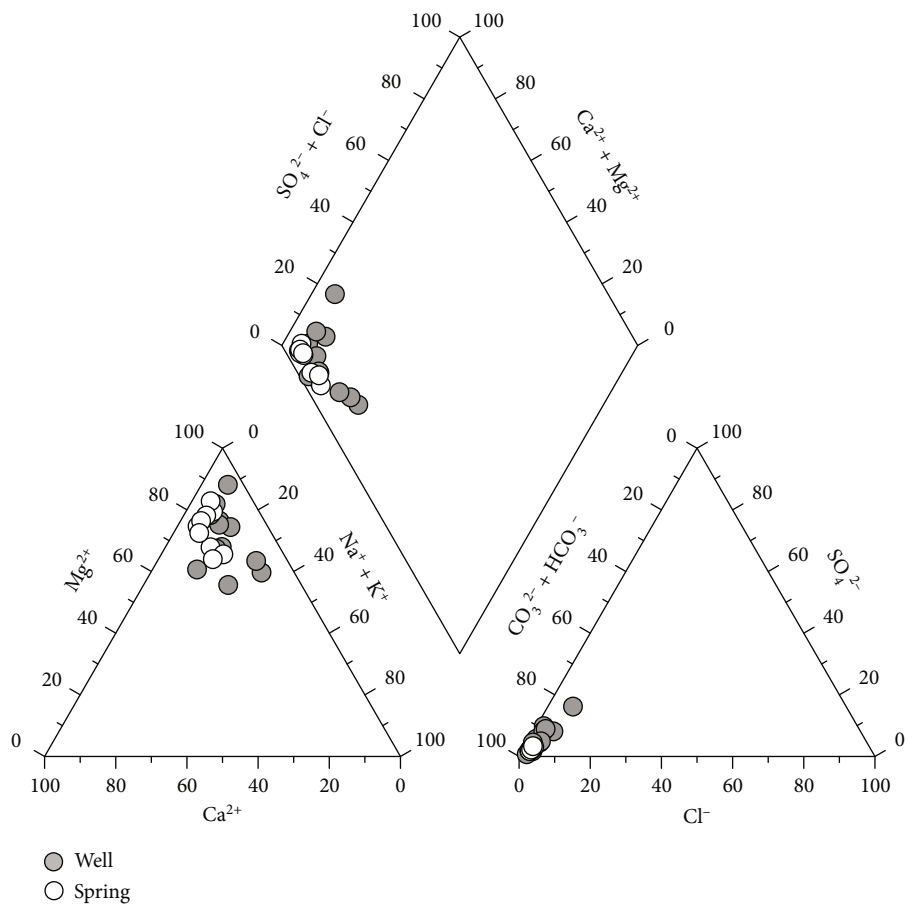

Figure 5: Piper diagram.

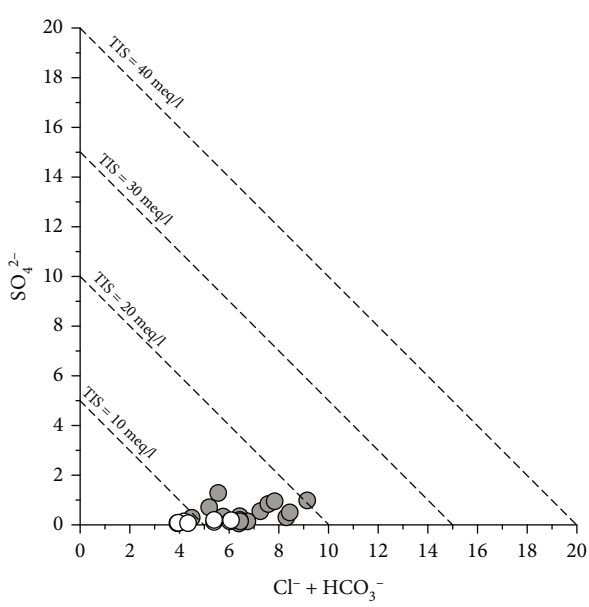

Figure 6: Correlation diagram of SO_4^{2-} vs. $HCO_3^- + Cl^-$ for the water samples. The symbols are as Figure 5.

The correlation between dissolved silica and Mg^{2+} is significant ($r = 0.65$, $p < 0.01$), clearly indicating silicate dissolution as additional source of Mg^{2+} in solution. The incongruent dissolution of silicates reacting with CO_2 derived from microorganism respiration and/or mineralization of soil organic matter can promote a Mg^{2+} surplus into the groundwater [32] and references therein. F1 thus represents the combined effect of dolomite and silicate dissolution on the release of Mg^{2+} in solution.

The second factor (F2; var.% = 15.2) includes significant and positive weightings for the largely soluble ions Na^+, Cl^-, and SO_4^{2-}. Overall, the investigated waters have Na/Cl meq/l ratio > 1, suggesting that Na^+ in groundwater may derive from weathering of mineral phases different from the common NaCl salt. The positive correlation between dissolved silica and Na^+($r = 0.66$, $p < 0.01$) associated with negative values of the feldspars SI (albite and anorthite, Table 2) suggests that the silicate incongruent dissolution is ongoing process allowing the release of Na^+ in solution.

Further, the log a $(H_4SiO_4)_{aq}$ vs. log a (Na^+/H^+) activity diagram (Figure 9) shows that the studied waters are in equilibrium with kaolinite, a T-O clayey mineral with a minor cation exchange capacity with respect to other clays, that does not include in its lattice interlayered cations such as Na^+. This, in turn, means that kaolinite cannot contribute to narrow down the Na^+ content in HAV groundwater. As

Table 3: Matrix of factor weights after varimax rotation using the STATGRAPHICS 18 package.

	Factor 1	Factor 2	Factor 3
T (°C)			
pH			
Na^+ (mg/l)		0.68	
Ca^{2+} (mg/l)			
Mg^{2+} (mg/l)	0.83		
HCO_3^-(mg/l)	0.92		
Cl^- (mg/l)		0.88	
SO_4^{2-}(mg/l)		0.85	
B (μg/l)			0.88
Sr (μg/l)			
Ba (μg/l)			
Total variance (%)	67.6	15.2	11.2
Cumulative variance (%)	67.6	82.8	94

Numbers are weights of the variables in the extracted factors. Variables having weights < 0.65 are omitted.

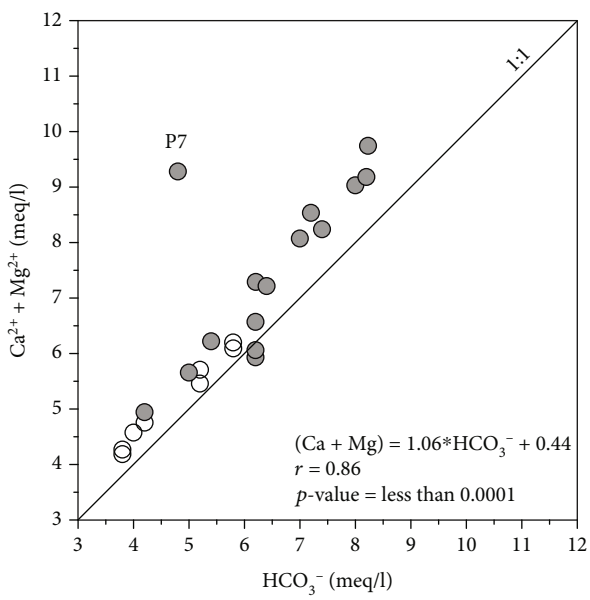

Figure 7: Binary plot of Ca^{2+} + Mg^{2+} vs. HCO_3^- concentrations. The symbols are as Figure 5.

for Cl^-, its geogenic abundance in groundwater increases with groundwater age [33], and excluding salt dissolution and marine spray supply at inland [34] and references therein, Cl^- may mostly derive from anions exchange at the clay mineral edges. In fact, depending on the pH of solution and due to protonation reactions at the broken bonds of both octahedral and tetrahedral layers, the clay mineral edges may be positively charged, promoting anions adsorption, e.g., [35].

The likely lack of sulphate minerals (anhydrite and gypsum) in HAV lithologies excludes a SO_4^{2-} origin through salt solubilization. Although oxidative reaction affecting suphides (e.g., pyrite FeS_2) dispersed in rocks, even in small amounts, may represent a source for SO_4^{2-} in groundwater, the use of

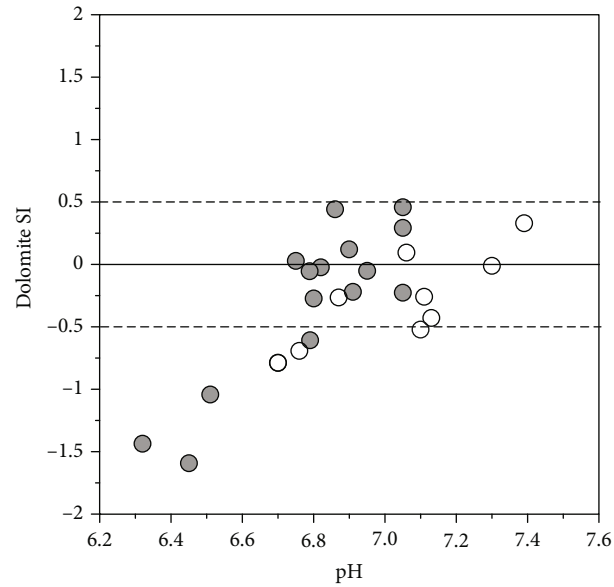

Figure 8: Diagram of the saturation indexes of dolomite (SI) and the pH values. The symbols are as Figure 5.

N-rich fertilizers may also originate most of the SO_4^{2-} in solution from the recycling of the groundwater used in irrigation. As shown in Figure 10 (NO_3^- vs. SO_4^{2-}), two different trends are clearly recognized. In the first one, involving exclusively well waters (except for S25 sample), the NO_3^-/SO_4^{2-} ratio is close to 1, and NO_3^- contents are generally >4 mg/l. P5 and P7 samples have the highest NO_3^- and SO_4^{2-} values. Although there are no baseline data on the NO_3^- geogenic level in the area, it is known that nitrate concentrations above 4 mg/l can be referred to anthropogenic contamination, e.g., [36, 37]. In our case, this supports the idea of an anthropogenic origin for SO_4^{2-}, mostly due to agriculture fertilizers. The second trend is outlined by a few wells showing larger SO_4^{2-} contents and low NO_3^- contents and suggests a possible geogenic origin for SO_4^{2-} due to oxidative reaction affecting suphides.

In the third factor (F3; var.% = 11.2), only boron has a significant weight. Boron contents in groundwater may be affected by anthropogenic activities [38] and interaction with evaporite levels, e.g., [39] and references therein. In the aqueous environment, B is a very mobile element occurring as boric acid ($B(OH)_3$) in dilute aqueous solution at pH < 7 and as prevailing metaborate anion ($B(OH)_4^-$)at pH > 10, e.g., [40] and references therein. Boron may have several possible natural and anthropogenic sources in inland aquifers including, for instance, leaching of geologic materials as well as domestic wastewater, e.g., [41] and references therein. The low B concentration observed in the HAV groundwater (well below 100 μg/l) appears to exclude any significant anthropogenic source. F3 thus likely accounts for the solubilization of B by leaching of sedimentary deposits of marine and non-marine origin, e.g., [42] and references therein.

5.2. Isotopic Constraints. Water isotopes are used to define water origin, recharge areas, circulation paths, and mixing or exchange processes [43–45]. The δD and δ^{18}O values are displayed in Figure 11, together with the Northern Calabria

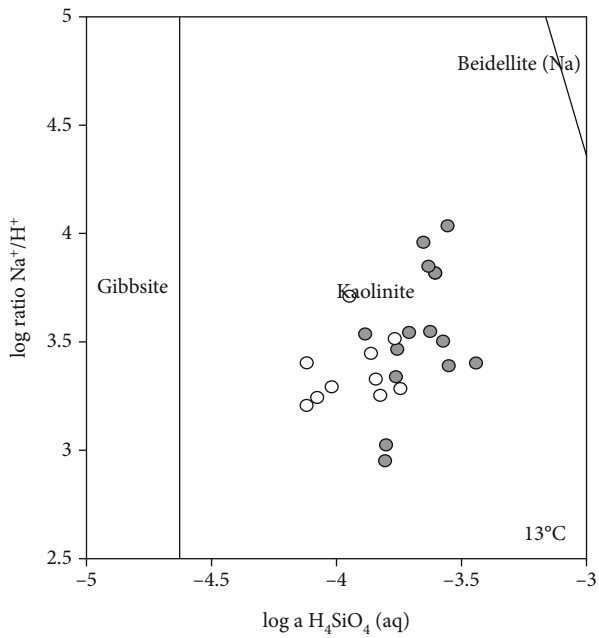

Figure 9: Activity plot of log a (H_4SiO_4) vs. log a (Na^+/H^+). The symbols are as Figure 5.

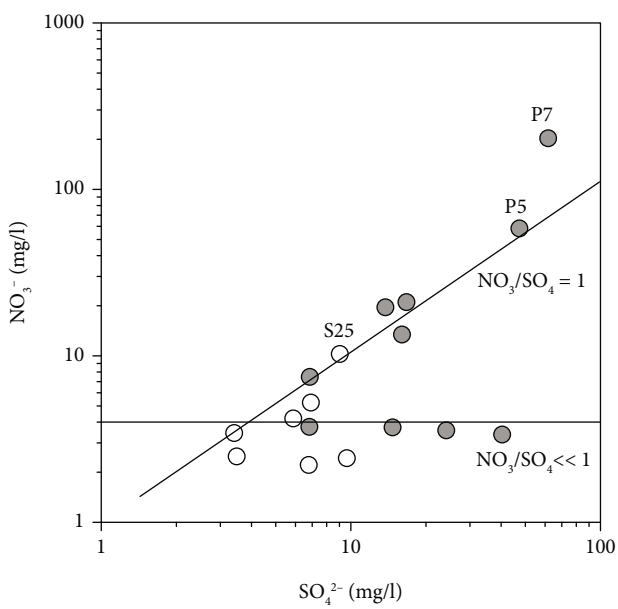

Figure 10: Relationships between SO_4^{2-} and NO_3^- contents in HAV water samples. The water samples with NO_3^- values lower than detection limit (1.9 mg/l) are not reported. P5 and P7 water samples have higher NO_3^- values. The NO_3^- geogenic level (equal to 4 mg/l) has been drawn. The symbols are as Figure 5.

Meteoric Water Line (NCMWL: $6.22 * \delta^{18}O + 5.21$ [46]), the Southern Italy Meteoric Water Line (SIMWL: $6.7 * \delta^{18}O + 5.2$ [47]), and the Global Meteoric Water Line (GMWL: $\delta D = 8.17 * \delta^{18}O + 10.35$ [48]). Spring waters are well-correlated ($r = 0.95$, p value < 0.0001, Figure 11(a)) and fall between SIMWL and NCMWL, while well waters show a wider data distribution ($r = 0.66$, p value $= 0.013$, Figure 11(b)) falling between GMWL and NCMWL. Both water types are fed by rainwater and have a meteoric origin.

The isotope data variation, measured in well waters, is probably linked to seasonal rainfall effect since the shallow porous aquifer has a relatively short and surface hydrogeological circuits through the gravelly-sandy permeable deposits of the quaternary succession.

Spring waters from karst and fissured aquifers showing a narrow range of O and ^2H isotopic values can be used to deduce the mean elevation of the recharge area through the equation proposed for southern Italy by Vespasiano et al. [46]:

$$\delta^{18}O = -0.00194 \times Hi - 5.91, \quad (7)$$

and a range of 1030 to 1540 meter a.s.l mean elevation of the recharge areas has been estimated. The inferred range is consistent with the elevation of the springs located in the highly fissured limestones (Carbonate Platform) and in the underlying "Calcari con Selce" Fm (Lagonegro Units). In addition, S11, S12, and S13 springs with more negative isotope data have longer and deeper hydrogeological circuit likely due to the local geological complexity affecting the recharge area to the west and north-west [17].

5.3. Groundwater for Irrigation and Drinking Uses. The groundwater quality is of fundamental relevance for irrigation and drinking purposes [3], also in the northern bank of the Mediterranean, affected by climate change evolving toward semiarid to arid conditions, e.g., [49] and references therein. The amount of dissolved ions affects the agricultural productivity influencing both the growth of plants and soil structure [50]. Some important irrigation quality parameters (such as SAR, MAR, %Na, RSBC, and PI) are largely used for determining the suitability of groundwater for a proper agricultural uses [8, 51, 52] and references therein. Irrigation water quality parameters of the analysed groundwater are shown in Table 1.

The %Na vs. EC plot [53] provides a mostly adopted method for rating irrigation water. In Figure 12, the HAV groundwater falls in the "excellent to good" and to a lesser extent in the "good to permissible" fields. Similarly, the PI indicates that the HAV groundwater is suitable for irrigation, being ranked as class I (PI: 30-50%; total concentration: 13-39 meq/l). However, in the SAR vs. EC diagram [26], the HAV groundwater is ranked as C2S1 and C3S1 (medium to high salinity hazard and low sodium hazard, Figure 12).

Excess salinity reduces the osmotic activity of plants limiting the absorption of water and nutrients from the soil of exchange able sodium, e.g., [54]. This suggests that efforts, including leaching and proper drainage, are needed in order to control the salinity hazard, especially for those waters, representing a significant part of HAV groundwater dataset, having EC higher than 750 μs/cm.

Accordingly, some concerns also arise from the RSBC values, mostly related to the relatively high HCO_3^- content, that in most samples is >5 meq/l, implying that HAV

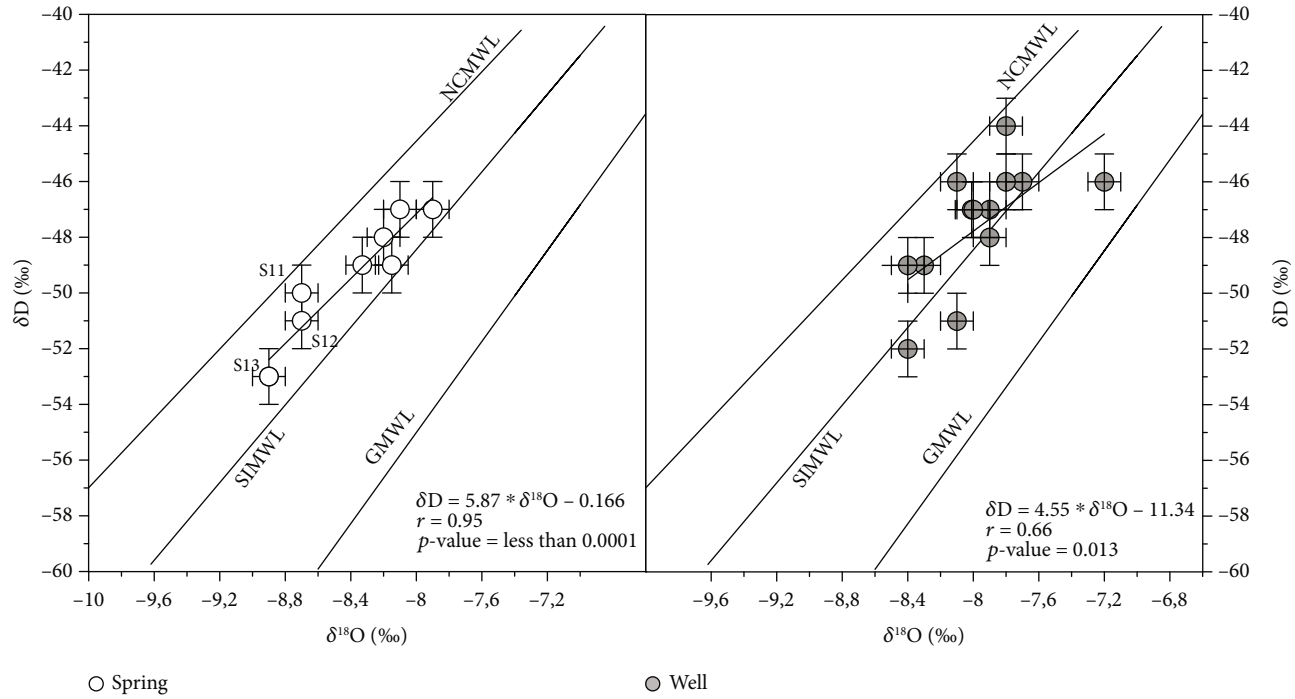

Figure 11: $\delta^{18}O$ and δD of the groundwater samples, as compared with meteoric water lines (Northern Calabria Meteoric Water Line (NCMWL), $6.22 * \delta^{18}O + 5.21$, [46]; Southern Italy Meteoric Water Line (SIMWL), $6.7 * \delta^{18}O + 5.2$, [47]; Global Meteoric Water Line (GMWL), $\delta D = 8.17 * \delta^{18}O + 10.35$, [48]).The uncertainties 1σ ($\pm 0.1\%$ for $\delta^{18}O$ and $\pm 1\%$ for δD) were reported.

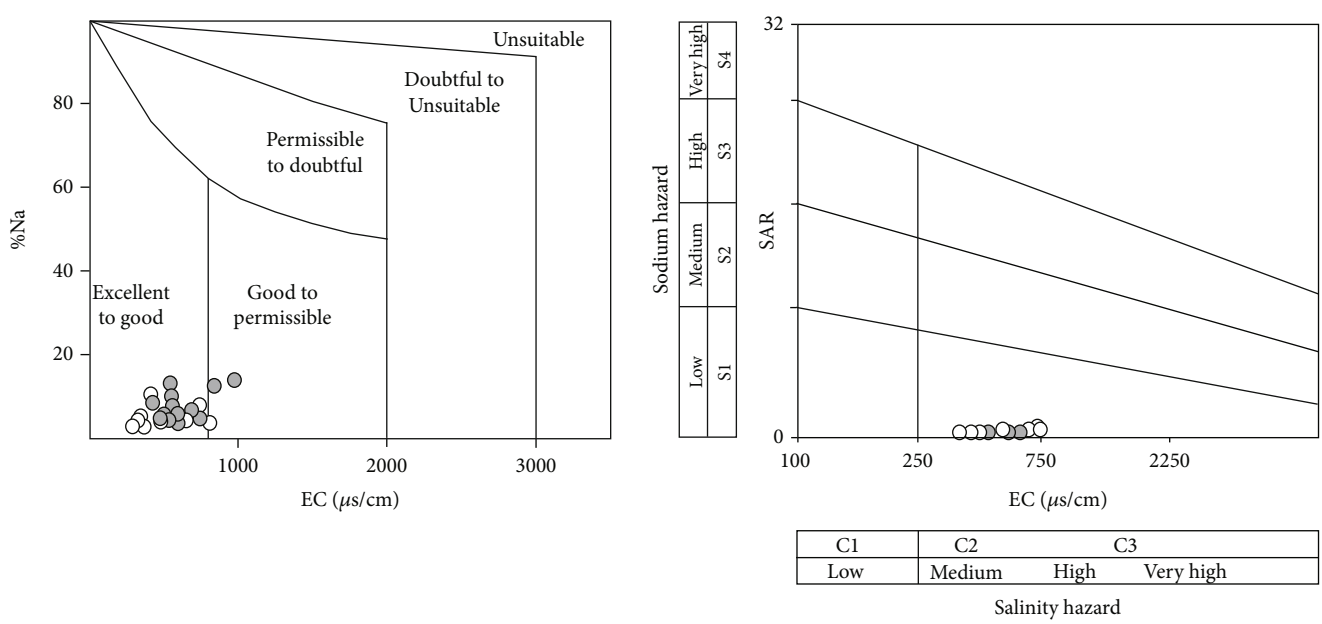

Figure 12: Plots of calculated values of %Na and SAR vs. EC of groundwater samples (after Wilcox [53] and [26], respectively). The symbols are as Figure 5.

groundwater cannot be classified as fully satisfactory for irrigation purposes according to Gupta and Gupta [29]. RSBC exceeding 5 meq/l may cause an alkalizing effect, claiming for a bicarbonate neutralization when long-term irrigation purposes are required [55]. An additional alkalizing effect is also due to high Mg^{2+} contents in groundwater. Usually, Ca^{2+} and Mg^{2+} are in equilibrium in most waters, and Raghunath [27] and Gupta and Gupta [29] suggested that MAR values exceeding 50% indicate magnesium hazard as soils become more alkaline [56], favoring the decrease of phosphorous availability [57]. In the HAV groundwater, MAR is always >70% indicating magnesium hazard and suggesting long-term magnesium monitoring in the area in order to plan alkalinity mitigation policies.

Table 4: Drinking water quality standard of WHO [60] and Italian legislation (D. Lgs. 31/2001, [58]).

Parameter/element	WHO (2004)		D. Lgs. 31/2001
	Desirable limit (DL)	Maximum permissible limit (MPL)	Maximum admissible concentrations (MAC)
pH	7-8.5	9	-
EC (μS/cm)	500	1500	-
TDS (mg/l)	500	1500	-
Cl^- (mg/l)	200	600	250
SO_4^{2-} (mg/l)	200	400	250
HCO_3^- (mg/l)	-	240	-
NO_3^- (mg/l)	-	50	50
NO_2^- (mg/l)	-	3	0.5
Ca^{2+} (mg/l)	75	200	-
Mg^{2+} (mg/l)	50	150	-
Na^+ (mg/l)	-	200	200
K^+ (mg/l)	-	12.0	-
Cu (mg/l)	-	1.0	1.0
Ba (mg/l)	-	2.0	-
B (mg/l)	-	0.5	1.0
Sr (mg/l)	-	0.5	-
V (mg/l)	-	-	0.05

-: no data.

In Italy, groundwater quality for drinking use is regulated by D. Lgs 31/2001 [58] (acceptance of the 98/83/EU directive [59]) which provides for the measurement of indicator parameters (such as odor, color, taste, pH, and hardness) and chemical and microbiological parameters. In this study, a preliminary assessment of groundwater quality for drinking use was proposed considering only some indicator and chemical parameters analysed. The drinking water quality was compared with the conditions set by the World Health Organization 2004 (hereafter WHO 2004 [60]) and the Italian legislation (D. Lgs. 31/2001). The relative maximum admissible concentrations (hereafter MAC) imposed for protecting of groundwater resources by the Italian legislation [58], and the desirable limit (DL) and maximum permissible limit (MPL) prescribed by WHO for drinking purposes are shown in Table 4.

Most water samples have TDS below DL of 500 mg/l as defined by the WHO, and overall HAV groundwater has TDS below MPL of 1500 mg/l as defined by the WHO specification for drinking water. In most samples, HCO_3^- exceeds the MPL defined by the WHO (240 mg/l). Na^+, Cl^-, and SO_4^{2-} are below the respective MPL (Na^+ = 200 mg/l; Cl^- = 600 mg/l; SO_4^{2-} = 400 mg/l).

NO_3^- contents are always below the MAC of 50 mg/l except for two water samples (P5 and P7) having very high NO_3^- values (58 and 203 mg/l, respectively). Some environmentally relevant trace elements, including B, V, and Cu, are characterized by very low contents, below the respective MAC and MPL. Ba and B are below the guideline values provided by the WHO for drinking water whereas Sr^{2+} exceeds the MPL (0.5 mg/l) in two water samples (P5 and P7). Our data allows to state that P5 and P7 water samples, used only for irrigation use, show critical issue for Sr^{2+} and NO_3^- concentrations. As previously said, high NO_3^- values are well-related to SO_4^{2-} contents and are linked to human activities, including mainly agricultural activities.

As to strontium values, it is well known that Sr-bearing minerals (mainly carbonate and sulphate) are distributed in a number of rock types, and Sr^{2+} release from minerals and rocks to water by weathering processes is very common [61]. Strontium, in fact, readily reacts with water and oxygen to form insoluble mineral phases or create complexes with carbonate and silicate depending on the water mineralization. Therefore, high Sr^{2+} concentrations may indicate an anthropogenic input by agricultural activities such as the use of fertilizers, carbonate additives, manure (i.e., cattle and poultry) and dumping, and industrial wastes [62]. Excluding P5 and P7 samples, a good and positive correlation between Sr^{2+} and HCO_3^- is evident for the analysed dataset ($r = 0.75$, $p < 0.01$), suggesting that Sr^{2+} contents are linked to carbonate phases. Conversely, as P5 and P7 waters show high NO_3^- and SO_4^{2-} contents, in addition to the Sr^{2+} ones, a contribution from agricultural practices cannot be excluded for these waters. Although a microbiological characterization is required for defining the overall groundwater quality, based on the analysed inorganic component, all HAV groundwaters are suitable for drinking use, except for two well waters.

6. Conclusions

Groundwater is an essential water resource for drinking and irrigation uses in the HAV. In this study, hydrogeochemistry coupled with multivariate statistics, saturation indices, and stable isotope composition was used to assess the geochemical processes controlling the groundwater chemistry. Consequently, groundwater quality and its suitability for drinking and agricultural use were evaluated. All the examined groundwater has a meteoric origin although some springs show long and deep flow than the other ones. The main geochemical process affecting water chemistry is the dolomite and silicate dissolution that is also controlled by the concentration and distribution of trace elements. The SO_4^{2-}/NO_3^- ratios suggest that an anthropogenic contamination, mostly associated with the use of agriculture fertilizers, cannot be excluded for some water samples (P5 and P7 samples). The suitability of water for drinking purposes was evaluated by comparing different chemical parameters with those reported by the World Health Organization [29] and the Italian legislation guidelines. Our results demonstrate that most of HAV groundwater is chemically suitable for drinking use with respect to the analysed inorganic chemical elements. As to agricultural use, the % Na and PI indicate that groundwater is generally useful for irrigation, although SAR, MAR, and RSBC highlight a medium to high salinity hazard. In light of the recent increase in human activities (i.e., industrialization and intensive agricultural practices), this study represents a warning for the local authorities providing significant insights to delineate a successful policy for management of groundwater resources.

Data Availability

The data used to support the findings of this study are included within the article.

Disclosure

Part of the paper is related to Maria Assunta Musto Master degree thesis (University of Basilicata, Potenza-Italy).

Conflicts of Interest

There are no conflicts of interest to declare.

Authors' Contributions

All the authors have approved the manuscript and agree with submission to your esteemed journal.

Acknowledgments

The authors are indebted to Prof. ssa Giuliana Bianco and Dr. Raffaella Pascale for their support during chemical analysis at University of Basilicata. This research has been supported by a grant (RIL2009-Unibas) of G. Mongelli and M. Paternoster and partially by the project "Detection and tracking of crustal fluid by multi-parametric methodolo-gies and technologies" of the Italian PRIN-MIUR programme (grant no. 20174X3P29).

References

[1] X. Wang, L. Zhang, Z. Zhao, and Y. Cai, "Heavy metal pollution in reservoirs in the hilly area of southern China: distribution, source apportionment and health risk assessment," *Sci. Total Environ.*, vol. 634, pp. 158–169, 2018.

[2] S. Melki, E. L. Mabrouk, A. Asmi, M. O. B. Sy, and M. Gueddari, "A geochemical assessment and modeling of industrial groundwater contamination by orthophosphate and fluoride in the Gabes-North aquifer, Tunisia," *Environmental Earth Sciences*, vol. 79, no. 6, 2020.

[3] S. Melki, E. L. Mabrouk, A. Asmi, and M. Gueddari, "Inferred industrial and agricultural activities impact on groundwater quality of Skhira coastal phreatic aquifer in Southeast of Tunisia (Mediterranean region)," *Geofluids*, vol. 2019, 19 pages, 2019.

[4] G. Vespasiano, G. Cianflone, C. B. Cannata, C. Apollaro, R. Dominici, and R. De Rosa, "Analysis of groundwater pollution in the Sant'Eufemia Plain Calabria–South Italy," *Italian Journal of Engineering Geology and Environment*, vol. 16, no. 2, pp. 5–15, 2016.

[5] G. Vespasiano, G. Cianflone, A. Romanazzi et al., "A multidisciplinary approach for sustainable management of a complex coastal plain: the case of Sibari Plain (Southern Italy)," *Marine and Petroleum Geology*, vol. 109, pp. 740–759, 2019.

[6] S. Parisi, M. Paternoster, F. Perri, and G. Mongelli, "Source and mobility of minor and trace elements in a volcanic aquifer system: Mt. Vulture (southern Italy)," *Journal of Geochemical Exploration*, vol. 110, no. 3, pp. 233–244, 2011.

[7] S. Muhammad, M. T. Shah, and S. Khan, "Health risk assessment of heavy metals and their source apportionment in drinking water of Kohistan region, northern Pakistan," *Microchemical Journal*, vol. 98, no. 2, pp. 334–343, 2011.

[8] M. B. Alaya, S. Saidi, T. Zemni, and F. Zargouni, "Suitability assessment of deep groundwater for drinking and irrigation use in the Djeffara aquifers (Northern Gabes, South-Eastern Tunisia)," *Environment and Earth Science*, vol. 71, no. 8, pp. 3387–3421, 2014.

[9] C. Apollaro, A. Caracausi, M. Paternoster et al., "Fluid geochemistry in a low-enthalpy geothermal field along a sector of southern Apennines chain (Italy)," *Journal of Geochemical Exploration*, vol. 219, p. 106618, 2020.

[10] M. Paternoster, G. Oggiano, R. Sinisi, A. Caracausi, and G. Mongelli, "Geochemistry of two contrasting deep fluids in the Sardinia microplate (western Mediterranean): relationships with tectonics and heat sources," *Journal of Volcanology and Geothermal Research*, vol. 336, pp. 108–117, 2017.

[11] R. Buccione, E. Fortunato, M. Paternoster et al., "Mineralogy and heavy metal assessment of the Pietra del Pertusillo reservoir sediments (Southern Italy)," *Environmental Science and Pollution Research*, vol. 28, no. 4, pp. 4857–4878, 2021.

[12] G. Cello, R. Gambini, S. Mazzoli, A. Read, E. Tondi, and V. Zucconi, "Fault zone characteristics and scaling properties of the Val d'Agri Fault System (southern Apennines, Italy)," *Journal of Geodynamics*, vol. 29, no. 3-5, pp. 293–307, 2000.

[13] E. Gueguen, M. Bentivenga, R. Colaiacovo, S. Margiotta, V. Summa, and I. Adurno, "The Verdesca landslide in the Agri Valley (Basilicata, Southern Italy): a new geological and geomorphological framework," *Natural Hazards and Earth System Sciences*, vol. 15, no. 11, pp. 2585–2595, 2015.

[14] M. Schiattarella, P. Di Leo, P. Beneduce, and S. I. Giano, "Quaternary uplift vs tectonic loading: a case study from the Lucanian Apennine, southern Italy," *Quaternary International*, vol. 101-102, pp. 239–251, 2003.

[15] A. Giocoli, T. A. Stabile, I. Adurno et al., "Geological and geophysical characterization of the southeastern side of the High Agri Valley (southern Apennines, Italy)," *Natural Hazards and Earth System Sciences*, vol. 15, no. 2, pp. 315–323, 2015.

[16] T. A. Stabile, A. Giocoli, V. Lapenna, A. Perrone, S. Piscitelli, and L. Telesca, "Evidence of low-magnitude continued reservoir-induced seismicity associated with the Pertusillo artificial lake (southern Italy)," *Bulletin of the Seismological Society of America*, vol. 104, no. 4, pp. 1820–1828, 2014.

[17] S. Carbone, S. Catalano, S. Lazzari, F. Lentini, and C. Monaco, "Presentazione della carta geologica del Bacino del Fiume Agri (Basilicata)," *Memorie della Società Geologica Italiana*, vol. 47, pp. 129–143, 1991.

[18] S. I. Giano, V. Lapenna, S. Piscitelli, and M. Schiattarella, "Electrical imaging and self-potential surveys to study the geological setting of the quaternary slope deposits in the Agri High Valley (southern Italy)," *Annali di Geofisica*, vol. 43, pp. 409–419, 2000.

[19] G. Spilotro, F. Caporale, F. Canora, M. Di Cagno, G. Leandro, and M. Moreno, "Idrodinamica della piana alluvionale dell'Alta Val d'Agri," in *Le risorse idriche sotterranee dell'Alta Val d'Agri*, A. Colella, Ed., Collana Editoriale di Studi e Ricerche dell'Autorità Interregionale di Bacino della Basilicata, n. 3, Potenza, 2003.

[20] M. Civita, M. De Maio, and B. Vigna, "Studio delle risorse sorgive degli acquiferi carbonatici dell'Alta Val D'Agri," in *Le risorse idriche sotterranee dell'Alta Val d'Agri*, A. Colella, Ed., Collana Editoriale di Studi e Ricerche dell'Autorità Interregionale di Bacino della Basilicata, n. 3, Potenza, 2003.

[21] A. Colella, V. Lapenna, and E. Rizzo, "La struttura sepolta del bacino dell'Alta Val d'Agri (Pleistocene, Basilicata)," in *Le risorse idriche sotterranee dell'Alta Val d'Agri*, A. Colella, Ed., Collana Editoriale di Studi e Ricerche dell'Autorità Interregionale di Bacino della Basilicata, n. 3, Potenza, 2003.

[22] M. Paternoster, A. Scarfiglieri, and G. Mongelli, "Groundwater chemistry in the high Agri Valley (southern Apennines, Italy)," *Geo Acta*, vol. 4, pp. 25–41, 2005.

[23] L. M. L. Nollet, *Handbook of Water Analysis*, CRC press, 2nd edition, 2000.

[24] C. M. Bethke, "The Geochemist's Workbench® Release 8.0 (four volumes)," in *Hydrogeology Program*, University of Illinois, Urbana, Illinois, 2010.

[25] P. Blanck, A. Lassin, P. Piantone et al., "Thermoddem: a geochemical database focused on low temperature water/rock interactions and waste materials," *Applied Geochemistry*, vol. 27, no. 10, pp. 2107–2116, 2012.

[26] L. A. Richards, "Diagnosis and Improvement of Saline Alkali Soils," in *Agriculture, vole 160. Handbook 60*, US Department of Agriculture, Washington, 1954.

[27] H. M. Raghunath, *Groundwater*, Wiley, New Delhi, 1987.

[28] D. K. Todd and L. W. Mays, *Groundwater Hydrology*, Wiley, New York, 3rd edition, 2005.

[29] S. K. Gupta and I. C. Gupta, *Management of Saline Soils and Water*, Oxford and IBM Publ. Co, New Delhi, 1987.

[30] C. Apollaro, V. Tripodi, G. Vespasiano et al., "Chemical, isotopic and geotectonic relations of the warm and cold waters of the Galatro and Antonimina thermal areas, southern Calabria, Italy," *Marine and Petroleum Geology*, vol. 109, pp. 469–483, 2019.

[31] J. C. Davis, *Statistics and Data Analysis in Geology. Vol. 646*, John Wiley & Sons, New York, 1986.

[32] F. Frondini, O. Vaselli, and M. Vetuschi Zuccolini, "Consumption of atmospheric carbon dioxide through weathering of ultramafic rocks in the Voltri Massif (Italy): quantification of the process and global implications," *Geosciences*, vol. 9, no. 6, p. 258, 2019.

[33] J. R. Degnan, B. D. Lindsey, J. P. Levitt, and Z. Szabo, "The relation of geogenic contaminants to groundwater age, aquifer hydrologic position, water type, and redox conditions in Atlantic and Gulf Coastal Plain aquifers, eastern and south-central USA," *Science of the Total Environment*, vol. 723, p. 137835, 2020.

[34] G. Mongelli, S. Monni, G. Oggiano, M. Paternoster, and R. Sinisi, "Tracing groundwater salinization processes in coastal aquifers: a hydrogeochemical and isotopic approach in the Na-Cl brackish waters of northwestern Sardinia, Italy," *Hydrology and Earth System Sciences*, vol. 17, no. 7, pp. 2917–2928, 2013.

[35] G. H. Bolt and M. G. M. Bruggenwert, *Soil Chemistry. A: Basic elements*, Elsevier, Amsterdam, Netherlands, 1978.

[36] I. S. Babiker, A. A. Mohamed, H. Terao, K. Kato, and K. Ohta, "Assessment of groundwater contamination by nitrate leaching from intensive vegetable cultivation using geographical information system," *Environment International*, vol. 29, no. 8, pp. 1009–1017, 2004.

[37] G. Mongelli, M. Paternoster, and R. Sinisi, "Assessing nitrate origin in a volcanic aquifer using a dual isotope approach," *International journal of Environmental Science and Technology*, vol. 10, no. 6, pp. 1149–1156, 2013.

[38] E. Giménez and I. Morell, "Utilisación del boro comoindicatoro de contaminacion en la Plana de Castellon," *Hidrogeologica y Recursos Hidraulicos XVI (IV)*, vol. 16, pp. 285–292, 1992.

[39] O. Hebrard, S. Pistre, N. Cheynet, J. Dazy, C. Batiot-Guilhe, and J. L. Seidel, "Origine des eaux des émergences karstiques chlorurées du Languedoc-Roussillon," *Comptes Rendus Geoscience*, vol. 338, no. 10, pp. 703–710, 2006.

[40] S. Cuccuru, F. Deluca, G. Mongelli, and G. Oggiano, "Granite and andesite-hosted thermal water: geochemistry and environmental issues in northern Sardinia, Italy," *Environmental Earth Sciences*, vol. 79, no. 11, p. 257, 2020.

[41] P. M. Buszka, J. Fitzpatrick, L. R. Watson, and R. T. Kay, "Evaluation of ground-water and boron sources by use of boron stable-isotope ratios, tritium, and selected water-chemistry constituents near Beverly Shores, Northwestern Indiana," *U.S. Geological Survey Scientific Investigations Report 2007–5166, U.S. Department of the Interior U.S. Geological Survey*, p. 46, 2007.

[42] M. Paternoster, "Boron isotopes in the Mount Vulture groundwaters southern Italy: constraints for the assessment of natural and anthropogenic contaminant sources," *Geofluids*, vol. 2019, Article ID 9107636, 2019.

[43] R. N. Clayton, I. Friedman, D. L. Graf, T. K. Mayeda, W. F. Meents, and N. F. Shimp, "The origin of saline formation waters: 1. Isotopic composition," *Journal of Geophysical Research*, vol. 71, no. 16, pp. 3869–3882, 1966.

[44] I. Clarke and P. Fritz, *Environmental Isotopes in Hydrogeology*, Lewis Publishers, New York, 1997.

[45] M. Paternoster, M. Liotta, and R. Favara, "Stable isotope ratios in meteoric recharge and groundwater at Mt. Vulture volcano, southern Italy," *Journal of Hydrology*, vol. 348, no. 1-2, pp. 87–97, 2008.

[46] G. Vespasiano, C. Apollaro, R. De Rosa et al., "The Small Spring Method (SSM) for the definition of stable isotope-elevation relationships in Northern Calabria (Southern Italy)," *Applied Geochemistry*, vol. 63, pp. 333–346, 2015.

[47] A. Longinelli and E. Selmo, "Isotopic composition of precipitation in Italy: a first overall map," *Journal of Hydrology*, vol. 270, no. 1-2, pp. 75–88, 2003.

[48] F. Schemmel, T. Mikes, B. Rojay, and A. Mulch, "The impact of topography on isotopes in precipitation across the Central Anatolian Plateau Turkey," *American Journal of Science*, vol. 313, no. 2, pp. 61–80, 2013.

[49] G. Mongelli, A. Argyraki, M. L. García Lorenzo, M. Wasif Shammout, M. Paternoster, and V. Simeone, "Groundwater quality in the Mediterranean region," *Geofluids*, vol. 2019, Article ID 7269304, 19 pages, 2019.

[50] P. Ravikumar, K. Venkatesharaju, and R. K. Somashekar, "Major ion chemistry and hydrochemical studies of groundwater of Bangalore South Taluk, India," *Environmental Monitoring and Assessment*, vol. 163, no. 1-4, pp. 643–653, 2010.

[51] M. Salifu, F. Aidoo, M. Saah Hayford, D. Adomako, and E. Asare, "Evaluating the suitability of groundwater for irrigational purposes in some selected districts of the Upper West region of Ghana," *Applied Water Science*, vol. 7, no. 2, pp. 653–662, 2017.

[52] K. S. Rawat, S. K. Singh, and S. K. Gautam, "Assessment of groundwater quality for irrigation use: a peninsular case study," *Applied Water Science*, vol. 8, no. 8, 2018.

[53] L. V. Wilcox, *Classification and Use of Irrigation Waters*, USDA. Circ 969, Washington, DC, USA, 1955.

[54] T. Subramani, L. Elango, and S. R. Damodarasamy, "Groundwater quality and its suitability for drinking and agricultural use in Chithar River Basin, Tamil Nadu, India," *Environmental Geology*, vol. 47, no. 8, pp. 1099–1110, 2005.

[55] A. Shahabi, M. J. Malakouti, and E. Fallahi, "Effects of bicarbonate content of irrigation water on nutritional disorders of some apple varieties," *Journal of Plant Nutrition*, vol. 28, no. 9, pp. 1663–1687, 2005.

[56] S. K. Gautam, C. Maharana, D. Sharma, A. K. Singh, J. K. Tripathi, and S. K. Singh, "Evaluation of groundwater quality in the Chotanagpur plateau region of the Subarnarekha River basin, Jharkhand State, India," *Sustainability of Water Quality and Ecology*, vol. 6, pp. 57–74, 2015.

[57] M. Al-Shammiri, A. Al-Saffar, S. Bohamad, and M. Ahmed, "Waste water quality and reuse in irrigation in Kuwait using microfiltration technology in treatment," *Desalination*, vol. 185, no. 1–3, pp. 213–225, 2005.

[58] R. Italiana, "Decreto Legislativo 2 febbraio 2001, n. 31 Attuazione della direttiva 98/83/CE relativa alla qualità delle acque destinate al consumo umano," *Gazzetta Ufficiale della Repubblica Italiana*, vol. 52, 2001.

[59] EU Directive, 1998/83/EC, "Council Directive of 3 November 1998 on the quality of water intended for human consumption," *Official Journal of the European Union L 330*, pp. 32–54, 1998.

[60] World Health Organization, *Guidelines for Drinking Water Quality: Training Pack*, WHO, Geneva, 2004.

[61] G. Malina, "Ecotoxicological and environmental problems associated with the former chemical plant in Tarnowskie Gory, Poland," *Toxicology*, vol. 205, no. 3, pp. 157–172, 2004.

[62] P. Negrel and H. Pauwels, "Interaction between different groundwaters in Brittany catchments (France): characterizing multiple sources through strontium- and sulphur isotope tracing," *Water, Air, & Soil Pollution*, vol. 151, no. 1–4, pp. 261–285, 2004.

Hindawi
Geofluids
Volume 2021, Article ID 6617283, 8 pages
https://doi.org/10.1155/2021/6617283

Research Article

Environmental Estimation of Radiation Equivalent Dose Rates in Soils and Waters of Northern Calabria (Italy)

Ilaria Guagliardi,[1] Tommaso Caloiero,[1] Ernesto Infusino,[1,2] Giovanni Callegari,[1] and Nicola Ricca[1]

[1]*National Research Council of Italy, Institute for Agricultural and Forest Systems in the Mediterranean (CNR-ISAFOM), 87036 Rende, Italy*
[2]*University of Calabria, Department of Environmental Engineering (DIAm), Rende, Italy*

Correspondence should be addressed to Tommaso Caloiero; tommaso.caloiero@isafom.cnr.it

Received 23 October 2020; Revised 7 December 2020; Accepted 15 April 2021; Published 27 April 2021

Academic Editor: Jinze Xu

In this study, the equivalent dose rate of natural radionuclides (H_T) in 99 spring water and surface soil samples was determined using an alpha, beta, and gamma high sensitivity detector up within a Geiger-Muller tube and with an external probe NaI (Tl). The samples were collected in the Crati basin (southern Italy), and during sample collection, water quality parameters were detected in situ and at the University of Calabria laboratories. A Pearson correlation coefficient analysis was applied to identify and clarify the relationships between water physical-chemical properties and soil and water radioactivity. Results show that the mean H_T for spring waters is 97.07 μSv/h. Furthermore, the mean H_T for surface soils is 97.92 μSv/h, thus evidencing higher mean H_T values than worldwide ones reported in a previous literature. Low correlation coefficients were detected between water H_T and conductivity and pH. On the contrary, a reasonable correlation was found between H_T in spring water and in soil. This relationship is associated with some rocks of the Sila Massif and of Coastal Chain, i.e., plutonic and metamorphic crystalline rocks. Finally, the estimation of the health risk was calculated: results did not evidence serious dangers for people living in the studied environment. The results from this survey for the H_T evaluation provide an extensive assessment of the background exposure levels in the investigated area.

1. Introduction

Knowledge of environmental natural radioactivity is essential to assess the current level of radiation exposure of the population and the degree of radioactive pollution in the environment in the future [1]. In fact, environmental radioactivity is the major source of radioactivity absorbed by people worldwide [2, 3] and cannot be avoided. Moreover, considering geochemical studies, it represents a significant source of information. Indeed, radiometric data can be used to coherently interpret correlations between radioelement distribution and other elements and to support the interpretation of petrogenetic or pedogenetic associations [4–6]. The evaluation of the environment natural radioactivity is also paramount to progressively monitor possible changes in natural background activity, as a result of radioactivity release [6].

Due to natural and man-made sources, a different level of radioactivity can be identified in the earth's crust [7, 8]. Naturally occurring radioactive materials include radioactive decay "chains" beginning with ^{238}U, ^{235}U and ^{232}Th, along with ^{40}K, ^{37}Rb, and other radioactive isotopes [9]. In particular, ^{238}U constitutes 99.3% of the isotopes of uranium found in nature, and thus, ^{235}U (0.7%), which provides a relatively insignificant radiation dose, is not surveyed further [10].

The distribution of naturally occurring radionuclides (principally ^{238}U, ^{232}Th, and their daughter products) and ^{40}K (among other radioactive elements) is strictly related to the distribution of rocks originating them and depends on the processes connected with their concentration [11]: it is caused by the decay of radionuclides derived from minerals. Consequently, the radioactivity amount in the soil depends on geology, soil type, soil moisture, organic matter, soil pH,

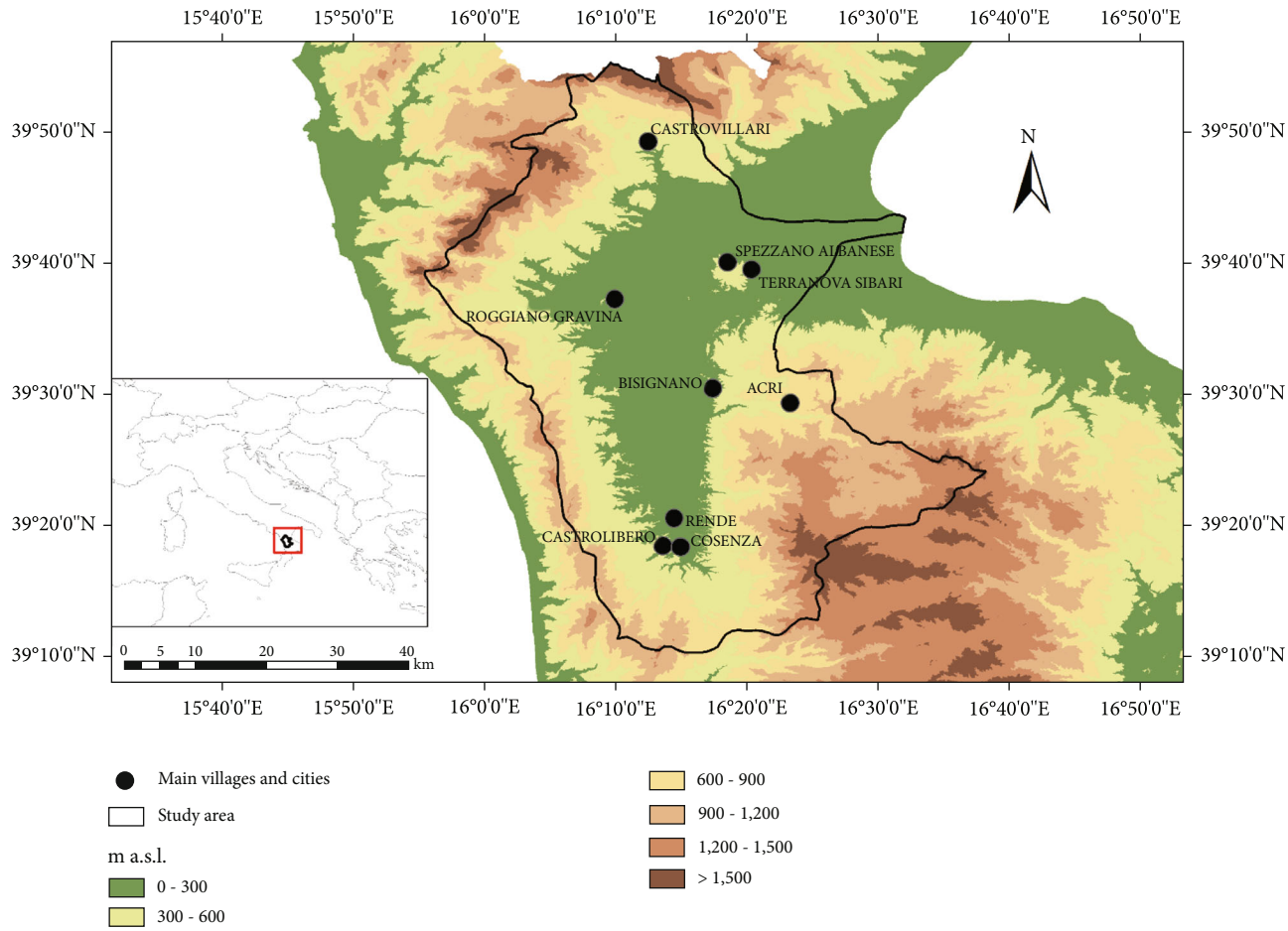

Figure 1: Crati river basin.

and climate with regard to the pluviometric and the thermometric regime of a region [12, 13]. Therefore, the concentrations of radionuclides vary widely depending on the location. Geologically, given the increasing uranium content of a rock with the silica content, high radiation levels can be generally found in igneous rocks, such as granite. In fact, some minerals which can be enriched in uranium and thorium (e.g., ilmenite, zircon, garnet, magnetite, rutile, and monazite) constitute the common mineral suites of these rocks. On the other hand, in some rock-forming, such as orthoclase, and accessory heavy minerals, the presence of potassium largely occurs. Lower levels are related to sedimentary rocks but with some peculiarity. In fact, in some shale and phosphate rocks a rather high content of radionuclides can be detected [14].

Environmentally, the soil on the earth's crust can be considered a radioactive threat because it is a source of continuous exposure for the population and because, considering agricultural soil, it allows radionuclides to enter the food chain and thus to contaminate humans through crops [15, 16]. Indeed, the soil-to-plant transfer can be considered a paramount process since; in the long run, radioelements enter the human food chains through the uptake of plant roots.

In addition, natural radioactive decay series can be dissolved in water and then move to surface water reservoirs, thus contributing to public radiation exposure [17]. This occurs especially, when aquatic organisms and plants keep radioisotopes coming from river soil and sediment [3].

Globally, an average radioactive dose from natural sources equal to about 2.4 mSv/y has been estimated. The exposure can be external, deriving from direct radiation, both cosmic and terrestrial, or internal, originating from the possible inhalation or ingestion of terrestrial and cosmogenic radionuclides which can be found in air, water, food, and soil. In particular, considering the world population, results of the assessments of the whole radiation dose evidenced that this is due to natural and artificial sources in fractions of about 96% and 4%, respectively [18].

The absorbed dose rates can be evaluated directly, thus allowing an even more extensive estimation of the background exposure levels in the study areas. Results of the spectrometric measurements show that, in both outdoors and indoors, the three items of the external radiation field, ^{238}U, ^{232}Th, and ^{40}K contributed equally to the externally incident gamma radiation dose to individual [19].

The dose received by each single members of the population can significantly vary considering the different sources. In fact, while all the population can be affected by some sources of radiation, in other cases, only few individuals can be exposed. For example, considering natural radioactivity, this can be found in all the soils, thus exposing all the

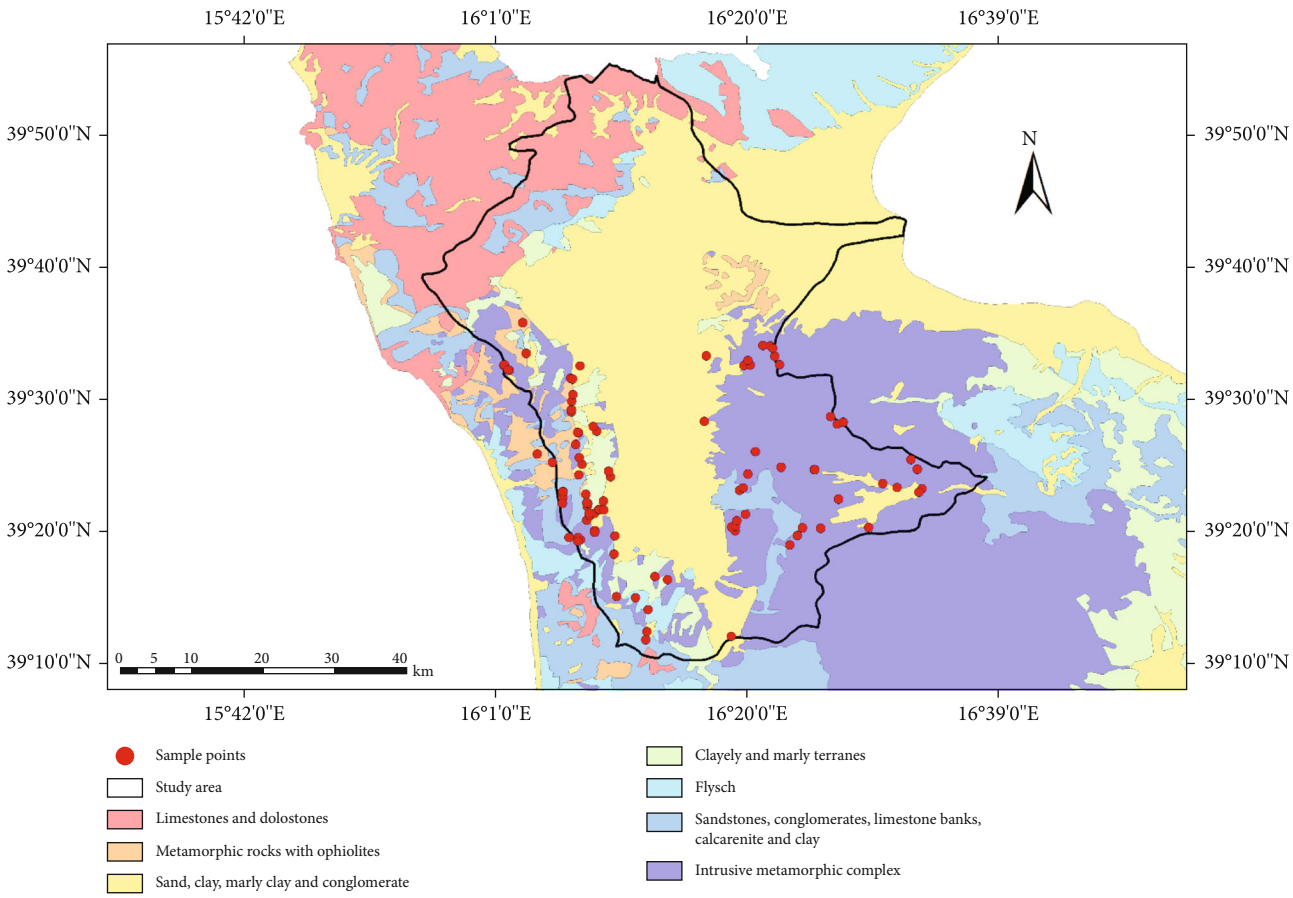

Figure 2: Lithological map of the study area and sample points.

population to some radiation dose. Conversely, considering the case of medical exposures, only people directly involved in medical treatment with radiation can receive a radiation dose [10].

Since the present study represents the first examination of a more detailed environmental survey, it offers an interesting and informative source to delineate the natural radiation equivalent dose rates in soils and waters of the Calabria region, located in southern Italy. Its preliminary findings illustrate a global overview of the study area setting and show that there are many future investigations needed. In particular, exploring and mapping the activity of the naturally occurring radionuclides are necessary and required in order to have information about the environment radiation level to assess the interaction between ionizing radiation and the human body. Thus, the survey performed in this study is aimed at quantifying the dose of radiation exposure, obtained from environmental radiation, in order to detect the possible risks for the public health caused by radiations from natural sources. Moreover, data obtained in this survey can contribute to the global data bank on radioactivity, thus allowing a more detailed evaluation of the mean values of the dosimetric quantities at global scale. The contribution to this data bank is especially important since these data allow a better understanding of the effects of low-level radiation in human health.

2. Site Characterization

The Crati basin is the largest and most important basin in the Calabria region [20]. It has an area of 2447.7 km^2 and a perimeter of about 320 km, with an elevation ranging from sea level to 2258 m a.s.l. and an average altitude of 597 m a.s.l. (Figure 1). Due to its dimension, the hydrographical system flowing in the basin includes waters deriving from several geological formations. The climate of the basin is largely influenced by its orography and its position in the middle of the Mediterranean basin [21–23]. Indeed, a hot summer Mediterranean climate, with very warm dry summers and mild rainy winters, characterizes the basin following the Köppen-Geiger classification [24].

The Crati basin is a depressed block of the crust bordered by parallel faults and circumscribed by the Sila Massif to the east, the Coastal Chain to the west and south, and the Pollino group to the north which represent the three morphostructural highs of the northern Calabria. The first one is composed by plutonic and metamorphic crystalline rocks, the second one by crystalline and sedimentary rocks, and the last one by carbonate and siliciclastic sedimentary rocks.

Geologically, it is branded by a succession of pliocenic sediments overlaying on Paleozoic intrusive-metamorphic complex (Figure 2). The lithological composition of this last one is characterized by paragneiss, biotite schists, and gray

phyllitic schists with quartz, chlorite, and muscovite, frequently affected by a weathering process [25].

The Coastal Chain shows, along its margins, the Miocene deposits characterized by the presence of basal conglomerate passing to sand, sandstone, calcarenite, and clay; the Messinian evaporite deposits is composed of conglomerate, marl, limestone, and clay with intercalated gypsum. Basal microconglomerate and sandstone evolving to clay characterize the Early Pliocene deposits. Polygenic conglomerate passing to marly clay, sand, and sandstone followed by marly clay, regressive sand, and conglomerate distinguishes the Upper Pliocene-Pleistocene sequences. Over these last ones, terraced marine deposits of Middle Pleistocene occur. Lastly, Holocene alluvial deposits crop out along the main river plains [26].

As evidenced in the regional soil map at 1 : 250,000 scale [27] the leading soil types of the study area vary from poorly to moderately differentiated soils, such as Fluvisols, Leptosols, Arenosols, Cambisols, Calcisols, Umbrisols, and Phaeozems to more developed Vertisols and Luvisols [28] and Entisols, Inceptisols, Mollisols, Vertisols, and Alfisols [29]. Intermediate soil properties between the ones typical of cold and subtropical climates characterize the Calabria region [30]. These features yield a manifest seasonality in radionuclides given the marked contrasts in temperature and relative humidity [31].

Concerning the spring waters in the study area and according to Gaglioti et al. [32], they are bicarbonate alkaline-earth and chloride-sulphate alkaline-earth waters. These findings reflect the global lithological environment of the study area. In fact, in the Coastal Chain, it mainly constituted calcareous and carbonatic rocks (providing high Ca^{2+}, Mg^{2+}, and HCO^{3-} ion concentration in water), while in the Sila Massif it is constituted by intrusive magmatic or metamorphic rocks (providing high SO_4^{2-} and Cl^- ion concentration in water).

3. Methodology

3.1. Sample Collection and Measurement Set-Up. In this study, 99 spring water and surface soil samples were analysed. Given the dimension of the basin (about 2400 km^2), the number of sampled points reflects the several outcropping geological formations in the study area.

In these sample locations, the equivalent dose rate of natural radionuclides (H_T) was determined at 1 m above the ground using an α, β, and γ high sensitivity detector up within a Geiger-Muller tube and with an external probe NaI (Tl).

During the sample collection, water quality parameters (temperature, pH, and conductivity) were detected in situ and at the University of Calabria laboratories. Air temperature was also measured. The technical specifications of the measurement apparatus are indicated in Table 1.

Table 1: Technical specifications of the radiation detector.

Inside Geiger-Muller detector	
Energy range	0.06–3 MeV
Accrual of environmental equivalent dose	10 μSv/h–100 mSv/h
Environmental equivalent dose	10 μSv–1 Sv
Sensitivity with ^{137}Cs source	0.3 cps/μSv.h-1
Weight	0.5 kg
Dimensions	92 × 62 × 52 mm
Detector NaI (Tl) diam. 40 × 40 *mm. External probe*	
Energy range	0.04–3 MeV
Accrual of environmental equivalent dose	0.03 to 100 μSv/h
Environmental equivalent dose	0.03 μSv–0.3 Sv
Sensitivity with ^{137}Cs source	900 cps/μSv.h-1
Weight	1.2 kg
Dimensions	diam. 60 × 320 mm
General characteristics	
Intrinsic measurement error	±20%
Protection class	IP64
Autonomy	24 h
Operating temperature	-30° to +50°
Relative moisture at 35° and below the compensation limit	Up to 95%
Beam	Extensible
Power source	Internal batteries MI-MH 6 V AC, 50 Hz 220 V DC 12 V
Radio interference	CEI/IEC CISPR 22 : 1997
Electromagnetic compatibility	CEI/IEC 61000-4-2 : 1995 - IEC 61000-4-3 : 1995

3.2. Equivalent Dose and Health Risk. The radiation dose, when reaching body tissues and organs, chains itself with the part of the body affected, the exposure pathway; therefore, no adsorbed Becquerel of radioactivity vehicles the same equal radiation dose as another. In order to assess the differences of the various radiations, which have dissimilar biological impacts, the unit "equivalent dose" (symbol H_T), whose measuring unit is the Sieverts (Sv), has been conventionally adopted. Quantitatively, the equivalent dose has a higher biological significance than the absorbed dose.

To calculate the H_T, a multiplication of the absorbed dose to the organ or tissue (DT) with the radiation weighting factor, wR, is required. wR is strictly associated to the type and energy of the incident radiation. Its value is 1 for X-rays, gamma rays, and beta particles and higher for protons (wR = 5), neutrons (wR is between 5 and 20 depending on energy), alpha particles, and heavy fragments (wR = 20) [33].

The estimation of fatal cancer risk for an individual, $\widehat{R}_i$, is defined by equation (1) [34]:

$$\widehat{R}_i = aH_T, \tag{1}$$

where a is the risk factor equal to 0.05 Sievert for terrestrial gamma radiation dose [35] and H_T is the equivalent dose rate.

Table 2: Main descriptive statistics of the measured parameters.

Statistics	Air T (°C)	Water T (°C)	pH	Conductivity (S/cm)	Water H_T (μSv/h)	Soil H_T (μSv/h)
Minimum	14.00	9.90	6.09	23.10	31.00	31.00
Maximum	32.00	32.00	8.59	1984.00	175.00	147.00
Mean	23.94	16.70	7.01	227.42	97.07	97.92
Median	24.00	16.20	6.96	170.30	95.00	95.00
St. Dev.	4.75	4.00	0.54	242.47	27.19	25.31
Skewness	-0.01	1.41	0.68	4.54	0.25	-0.01
Kurtosis	-0.87	3.01	0.02	28.41	0.17	-0.74

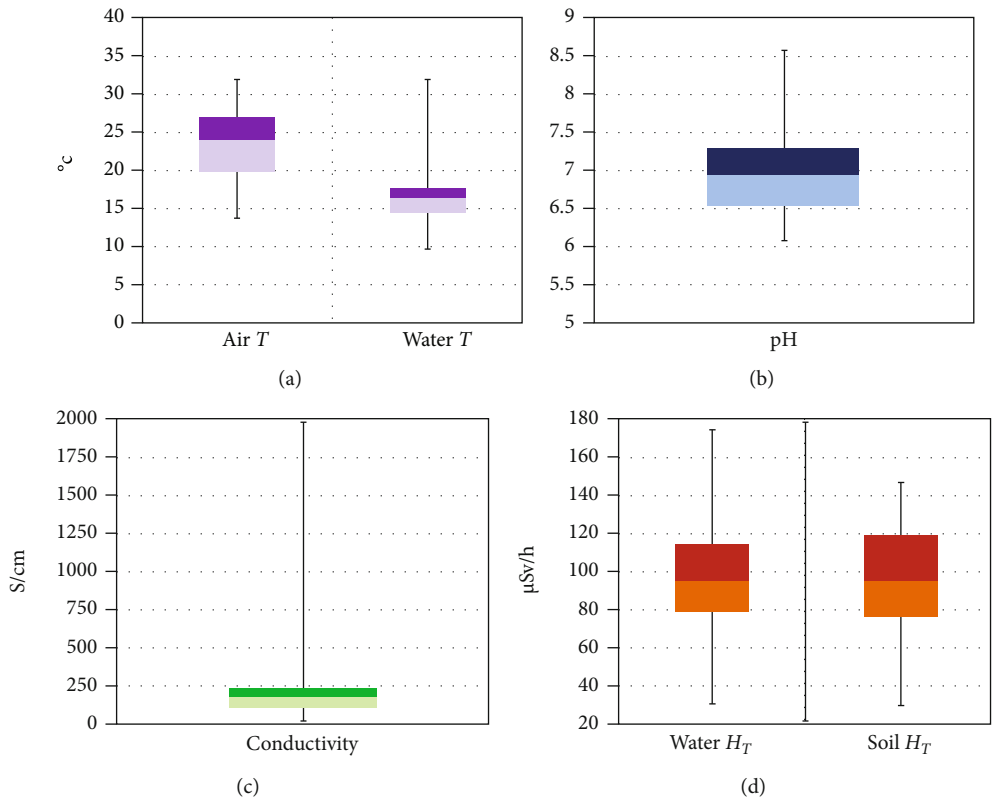

Figure 3: Boxplots of measured parameters.

4. Results and Discussion

Results show that the mean H_T for spring waters is 97.07 μSv/h, with a maximum value of 175 μSv/h and a minimum of 31 μSv/h (Table 2). Furthermore, the mean H_T for surface soils is 97.92 μSv/h, with a maximum value of 147 μSv/h and a minimum of 31 μSv/h (Table 2).

The main descriptive statistics of measured parameters are shown in Figure 3.

The Pearson correlation coefficient analysis was applied to identify the relationships between water physical-chemical properties, soil, and water radioactivity.

Low correlation coefficients were detected between the water H_T and conductivity and pH, with R^2 values equal to 0.057 and 0.1, respectively. On the contrary, a reasonable correlation was found between H_T in water and soil. This relationship is associated with some rocks (plutonic and metamorphic crystalline) of the Sila Massif and of the Coastal Chain, upon which the Crati basin soils are imposed.

According to Guagliardi et al. [13], a strong control on radioactivity can be assessed by considering the foremost pedogenetic features showed in the soil map of the Calabria region [27]. The soil sampling locations involved several soil types and geological background. The highest H_T values have been detected in locations characterized by soil type that originates mainly from igneous-metamorphic rocks (Figure 4) or in fairly young soils such as Fluvisols, Leptosols, and Cambisols. On the contrary, in older soils constituted on conglomerates and sands (Luvisols and Arenosols), lower values were mainly recorded.

In the Sila Massif, primary minerals constituting rocks contain K, U, and Th. Monazite, zircon, and K-feldspar are

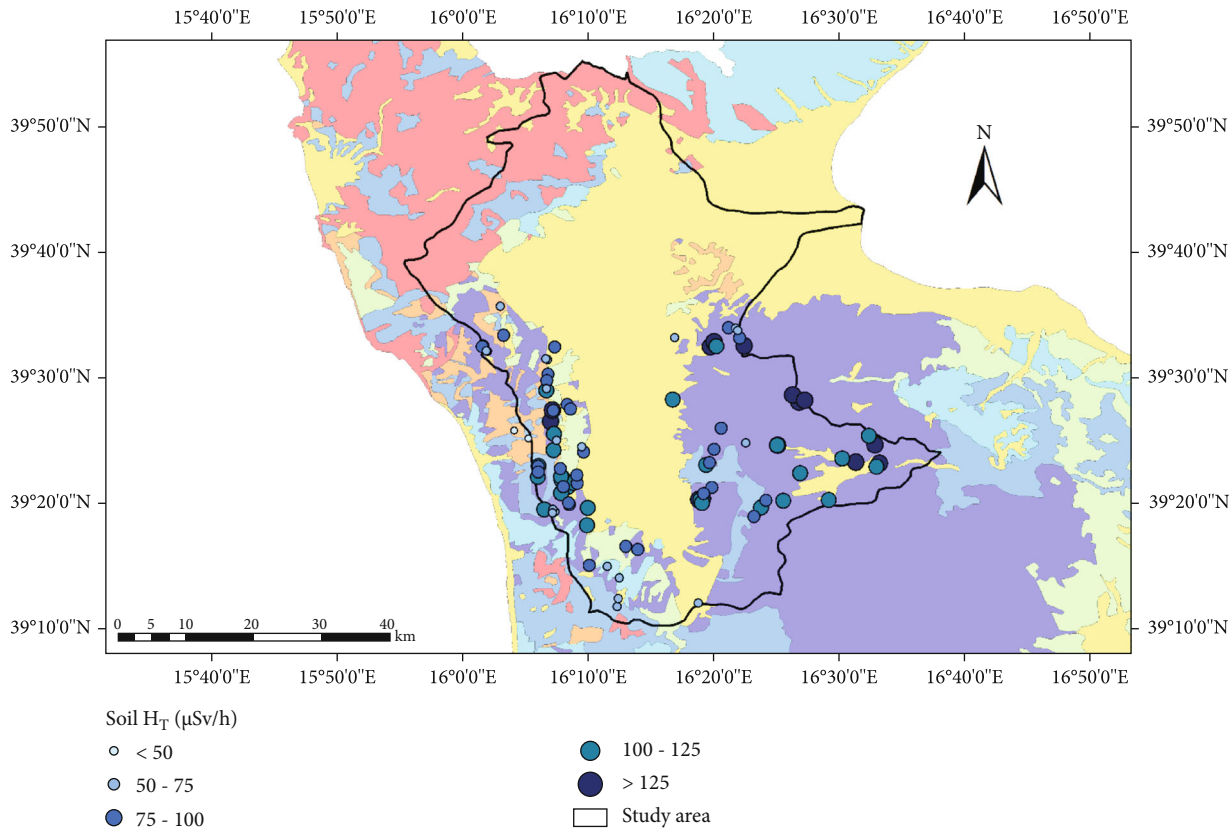

Figure 4: Dot map of equivalent dose rate in soils.

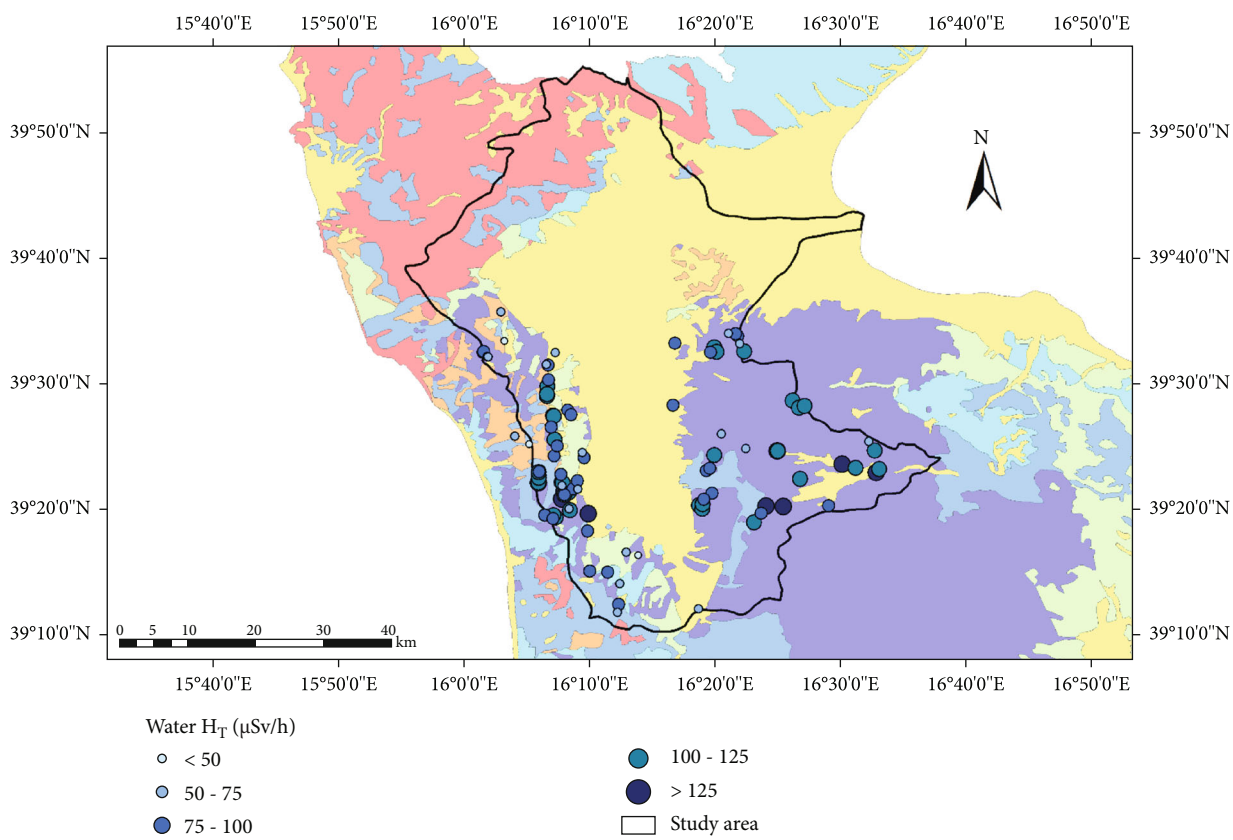

Figure 5: Dot map of equivalent dose rate in waters.

responsible of the apparent activity of the radionuclides. Specifically, in monazite, primarily radionuclides from the ^{232}Th series and from the ^{238}U series occur. Plagioclase and total feldspar content are related to U activities. Likewise, the primary minerals (such as K-feldspars, muscovite, and biotite) and the neo-formed phyllosilicate clays such as illite, which is a common weathering product of primary micas [36], contains potassium.

Similar outcomes can be assessed for the equivalent dose rates in waters (Figure 5). According to Gaglioti et al. [32], the sampled waters have origin in the calcareous and carbonatic rocks of the Coastal Chain and intrusive magmatic or metamorphic rocks of the Sila Massif, and consequently, their equivalent dose rates well fit the elemental distribution of the undergoing lithologies.

In order to assess the health effects, the soil radiation dose rate in the studied locations was calculated considering the UNSCEAR [19] recommendation using a factor of 0.007 to obtain units of radiation dose (in μSv/h) from an absorbed dose rate in air (in μGy/h). The soil radiation dose rate in the study area ranged from 4429 μGy/h to 21000 μGy/h with the mean value of 13989 μGy/h. The range of this value falls within the average world value of 5700 μGy/h [19], but the mean one is 2 times higher than it.

The mean effective dose in the soil area is 97.92 μSv/h. Using equation (1), this value will cause fatal cancer risk of about 43×10^6 per year to each individual in the area.

Nowadays, as a result of several studies performed worldwide, it has been generally recognized that, for radiation exposure doses lower than 100 mSv, statistically significant cancer excess has not been detected [37–43]. The health hazard evaluation shows that no significant radiological impact of the population occurs in the study area. This does not exempt the scientific community from paying attention to these issues because even if there is a dosage of low-level radiation below which no damage occurs, a long-term exposure can cause health damage.

5. Conclusions

Ionizing radiation from natural and anthropogenic sources concurs to human exposure and therefore constitutes a potential risk to human health.

The results from this survey for the H_T assessment provide a preliminary evaluation of the background exposure levels in the Crati basin in the Calabria region. For both soil and water, the highest H_T values were found at locations with soil types that originate mainly from igneous-metamorphic rocks and/or in relatively young soils. Conversely, the lowest values occur in older soils imposed on conglomerates and sands.

These equivalent dose rates do not pose a serious radioactive health hazard to the population living in the environment. However, exposure to the dose level over a long period can constitute a serious health risk. The results can reliably serve as reference values for the assessment of the equivalent dose due to natural radioactivity in the environment.

Data Availability

The data that support the findings of this study are available from the corresponding author upon reasonable request.

Conflicts of Interest

The authors declare that they have no conflicts of interest.

References

[1] M. M. Saç, F. Ortabuk, M. N. Kumru, M. İçhedef, and Ş. Sert, "Determination of radioactivity and heavy metals of Bakirçay river in Western Turkey," *Applied Radiation and Isotopes*, vol. 70, no. 10, pp. 2494–2499, 2012.

[2] A. K. Amanjeet, S. Kumar, J. Singh, P. Singh, and B. S. Bajwa, "Assessment of natural radioactivity levels and associated dose rates in soil samples from historical city Panipat, India," *Journal of Radiation Research and Applied Sciences*, vol. 10, no. 3, pp. 283–288, 2017.

[3] M. A. Saleh, A. T. Ramli, Y. Alajerami, and A. S. Aliyu, "Assessment of natural radiation levels and associated dose rates from surface soils in Pontian district, Johor, Malaysia," *Journal of Ovonic Research*, vol. 9, pp. 17–27, 2013.

[4] I. Guagliardi, G. Buttafuoco, and C. Apollaro, "Using gamma-ray spectrometry and geostatistics for assessing geochemical behaviour of radioactive elements in the lese catchment (southern Italy)," *International Journal of Environmental Research*, vol. 7, pp. 645–658, 2013.

[5] IAEA, *Guidelines for Radioelement Mapping Using Gamma Ray Spectrometry Data, IAEA–TECDOC–1363*, International Atomic Energy Agency, Vienna, 2003.

[6] M. M. Mehade Hasan, M. I. Ali, D. Paul, M. A. Haydar, and S. M. A. Islam, "Natural radioactivity and assessment of associated radiation hazards in soil and water samples collected from in and around of the Barapukuria 2×125 MW coal fired thermal power plant, Dinajpur, Bangladesh," *Journal of Nuclear and Particle Physics*, vol. 4, pp. 17–24, 2014.

[7] N. Akhtar, M. Tufail, M. Ashraf, and M. M. Iqbal, "Measurement of environmental radioactivity for estimation of radiation exposure from saline soil of Lahore, Pakistan," *Radiation Measurements*, vol. 39, no. 1, pp. 11–14, 2005.

[8] A. Faanu, O. K. Adukpo, L. Tettey-Larbi et al., "Natural radioactivity levels in soils, rocks and water at a mining concession of Perseus gold mine and surrounding towns in Central Region of Ghana," *SpringerPlus*, vol. 5, no. 1, 2016.

[9] T. M. Missimer, C. Teaf, R. G. Maliva, A. Danley-Thomson, D. Covert, and M. Hegy, "Natural radiation in the rocks, soils, and groundwater of Southern Florida with a discussion on potential health impacts," *International Journal of Environmental Research and Public Health*, vol. 16, no. 10, p. 1793, 2019.

[10] P. A. Colgan, C. Organo, C. Hone, and D. Fenton, *Radiation Doses Received by the Irish Population*, Radiological Protection Institute of Ireland, Dublin, 2008.

[11] I. Guagliardi, D. Zuzolo, S. Albanese et al., "Uranium, thorium and potassium insights on Campania region (Italy) soils: sources patterns based on compositional data analysis and fractal model," *Journal of Geochemical Exploration*, vol. 212, p. 106508, 2020.

[12] I. Guagliardi, N. Rovella, C. Apollaro et al., "Modelling seasonal variations of natural radioactivity in soils: a case study

in southern Italy," *Journal of Earth System Science*, vol. 125, no. 8, pp. 1569–1578, 2016.

[13] I. Guagliardi, N. Rovella, C. Apollaro et al., "Effects of source rocks, soil features and climate on natural gamma radioactivity in the Crati valley (Calabria, Southern Italy)," *Chemosphere*, vol. 150, pp. 97–108, 2016.

[14] I. El-Taher and J. H. Al-Zahrani, "Radiaoctivity measurements and radiation dose assessments in soil of Al-Qassim region, Saudi Arabia," *Indian Journal of Pure & Applied Physics*, vol. 52, pp. 147–154, 2014.

[15] I. Guagliardi, G. Buttafuoco, and N. Ricca, "Modelling seasonal variations of natural radionuclides in agricultural soils," in *In Proceedings of the 3S Web of Conferences*, vol. 1, 2013b.

[16] H. D. Van, T. D. Nguyen, A. Peka, M. Hegedus, A. Csordas, and T. Kovacs, "Study of soil to plant transfer factors of 226Ra, 232Th, 40K and 137Cs in Vietnamese crops," *Journal of Environmental Radioactivity*, vol. 223-224, 2020.

[17] S. J. Al-Kharouf, I. F. Al-Hamarneh, and M. Dababneh, "Natural radioactivity, dose assessment and uranium uptake by agricultural crops at Khan Al-Zabeeb, Jordan," *Journal of Environmental Radioactivity*, vol. 99, no. 7, pp. 1192–1199, 2008.

[18] M. P. Chougankar, K. P. Eppen, and T. V. Ramachandran, "Profiles of doses to population living in the high background radiation areas in Kerala," *Journal of Environmental Radioactivity*, vol. 71, pp. 275–297, 2004.

[19] UNSCEAR, *Sources and Effects of Ionizing Radiation*, Report of the United Nations Scientific Committee on the Effects of Atomic Radiation to the General Assembly, United Nations, New York, 2000.

[20] R. Coscarelli, R. Gaudio, and T. Caloiero, "Climatic trends: an investigation for a Calabrian basin (southern Italy)," in *In Proceedings of the International Symposium The basis of civilization. Water science?*, vol. 286, pp. 255–266, IAHS, Wallingford, IAHS Publications, 2004.

[21] G. Buttafuoco, T. Caloiero, N. Ricca, and I. Guagliardi, "Assessment of drought and its uncertainty in a southern Italy area (Calabria region)," *Measurement*, vol. 113, pp. 205–210, 2018.

[22] G. Pellicone, T. Caloiero, and I. Guagliardi, "The De Martonne aridity index in Calabria (Southern Italy)," *Journal of Maps*, vol. 15, no. 2, pp. 788–796, 2019.

[23] G. Pellicone, T. Caloiero, G. Modica, and I. Guagliardi, "Application of several spatial interpolation techniques to monthly rainfall data in the Calabria region (southern Italy)," *International Journal of Climatology*, vol. 38, no. 9, pp. 3651–3666, 2018.

[24] H. E. Beck, N. E. Zimmermann, T. R. McVicar, N. Vergopolan, A. Berg, and E. F. Wood, "Present and future Koppen-Geiger climate classification maps at 1-km resolution," *Scientific Data*, vol. 5, no. 1, 2018.

[25] I. Guagliardi, N. Ricca, and D. Cicchella, "From rock to soil: geochemical pathway of elements in Cosenza and Rende area (Calabria, southern Italy)," *Rendiconti Online della Società Geologica Italiana*, vol. 38, pp. 55–58, 2016.

[26] G. Iovine, I. Guagliardi, C. Bruno et al., "Soil-gas radon anomalies in three study areas of Central–Northern Calabria (Southern Italy)," *Natural Hazards*, vol. 91, pp. 193–219, 2018.

[27] ARSSA, *I suoli della Calabria. Carta dei suoli in scala 1:250000 della Regione Calabria. Monografia divulgativa: Programma Interregionale Agricoltura-Qualità*, Rubbettino Ed., Catanzaro, 2003.

[28] IUSS Working Group WRB, *International Soil Classification System for Naming Soils and Creating Legends for Soil Maps*, no. 106, 2014World Soil Resources Reports, FAO, Rome, 2014.

[29] Soil Survey Staff, *Keys to Soil Taxonomy*, United States Department of Agriculture (USDA), Natural Resources Conservation Service (NRCS), Washington DC, 2014.

[30] M. Llaurado, M. Vidal, G. Rauret, C. Roca, J. Fons, and V. R. Vallejo, "Radiocaesium behaviour in Mediterranean conditions," *Journal of Environmental Radioactivity*, vol. 23, no. 1, pp. 81–100, 1994.

[31] A. Baeza, J. Paniagua, M. Rufo, J. Guilléna, and A. Sterling, "Seasonal variations in radionuclide transfer in a Mediterranean grazing-land ecosystem," *Journal of Environmental Radioactivity*, vol. 55, no. 3, pp. 283–302, 2001.

[32] S. Gaglioti, E. Infusino, T. Caloiero, G. Callegari, and I. Guagliardi, "Geochemical characterization of spring waters in the Crati River Basin, Calabria (Southern Italy)," *Geofluids*, vol. 2019, Article ID 3850148, 2019.

[33] ICRP, *The 2007 Recommendations of the International Commission on Radiological Protection*, ICRP Publication 103, Pergamon Press, New York, 2007.

[34] J. L. Alvarez, *Ionizing Radiation Risk Assessment*, V. Molak, Ed., Fundamental of Risk Analysis and Risk Management, CRC Press, New York, 1997.

[35] ICRP, *Recommendations of the International Commission on Radiological Commission*, ICRP Publication 60, Pergamon Press, New York, 1990.

[36] I. Velde and A. Meunier, *The Origin of Clay Minerals in Soils and Weathered Rocks*, Springer-Verlag, Berlin, 2008.

[37] Electric Power Research Institute, *Program on Technology Innovation: Evaluation of Updated Research on the Health Effects and Risks Associated with LD Ionizing Radiation*, Electric Power Research Institute, Palo Alto, CA, 2009.

[38] American Association of Physicists in Medicine, *AAPM Position Statement on Radiation Risks from Medical Imaging Procedures*, 2011, http://www.aapm.org/org/policies/details.asp?id=318&type=PP.

[39] E. Cardis, M. Vrijheid, and M. Blettner, "The 15-country collaborative study of cancer risk among radiation workers in the nuclear industry: estimates of radiation-related cancer risks," *Radiation Research*, vol. 167, no. 4, pp. 396–416, 2007.

[40] M. Vrijheid, E. Cardis, and M. Blettner, "The 15-country collaborative study of cancer risk among radiation workers in the nuclear industry: design, epidemiological methods and descriptive results," *Radiation Research*, vol. 167, no. 4, pp. 361–379, 2007.

[41] D. B. Richardson, E. Cardis, R. D. Daniels et al., "Risk of cancer from occupational exposure to ionising radiation: retrospective cohort study of workers in France, the United Kingdom, and the United States (INWORKS)," *British Medical Journal*, vol. 351, 2015.

[42] K. Leuraud, D. B. Richardson, E. Cardis et al., "Ionising radiation and risk of death from leukaemia and lymphoma in radiation-monitored workers (INWORKS): an international cohort study," *Lancet Haematology*, vol. 2, pp. 276–281, 2015.

[43] A. Vaiserman, A. Koliada, O. Zabuga, and Y. Socol, "Health impacts of low-dose ionizing radiation: current scientific debates and regulatory issues," *Dose Response*, vol. 16, 2018.

Hindawi
Geofluids
Volume 2021, Article ID 6655711, 17 pages
https://doi.org/10.1155/2021/6655711

Research Article

Geochemical Modeling of Water-Rock Interaction Processes in the Pollino National Park

C. Apollaro,[1] I. Fuoco,[1] L. Bloise,[2] E. Calabrese,[2] L. Marini,[1,3] G. Vespasiano,[1] and F. Muto[1]

[1]*Department of Biology, Ecology and Earth Sciences (DiBEST), University of Calabria, Via Ponte Bucci, Cubo 15B, 87036 Arcavacata di Rende, Italy*
[2]*UNESCO Geopark Office Pollino National Park Authority, Complesso Monumentale S.M. della Consolazione 85038 Rotonda, Italy*
[3]*Steam Srl, Via Ponte a Piglieri 8, 56121 Pisa, Italy*

Correspondence should be addressed to I. Fuoco; ilaria.fuoco@unical.it

Received 20 October 2020; Revised 3 December 2020; Accepted 11 December 2020; Published 11 January 2021

Academic Editor: Francesco Frondini

This work is aimed at reconstructing the water-rock interaction processes controlling the geochemical characteristics of the shallow or relatively shallow groundwaters of the Pollino National Park, based on the data acquired for 105 water samples from local springs. Reaction path modeling of rock dissolution was carried out in a purely stoichiometric mode for the main lithotypes cropping out in the study area, that is, limestone, Mg-limestone, dolomite, serpentinite, Al-silicate fraction of calcschist, and carbonate fraction of calcschist. Reaction path modeling was carried out in a purely stoichiometric mode, considering the rocks of interest as materials of known stoichiometry and unknown thermodynamic properties. Calculations were carried out assuming a closed system for secondary solid phases whereas an open system was assumed for gases, O_2(g) and CO_2(g). Comparison of the results of geochemical modeling and the analytical data acquired for the groundwaters of the Pollino National Park shows that concentrations of major solutes, SiO_2, Li, Al, and Fe of the different chemical types of waters, are explained by the dissolution of pertinent lithotypes. Moreover, the detected concentrations of Al, Cl, F, NO_3, and SO_4 are within the threshold values recommended by WHO.

1. Introduction

The water-rock interaction process controls the physical and chemical-mineralogical transformations of all rock types and consequently the release of dissolved constituents to groundwaters (e.g., [1–4]). The resulting concentrations of major solutes in groundwaters depend on the chemical features of the initial rainwater, the geological setting, and the extent of the water-rock interaction process, which is related to the residence time in the aquifer system. When the groundwaters travel along their hydrogeological path from the recharge to discharge areas, diverse chemical reactions take place, including (i) dissolution-precipitation reactions, (ii) ion exchange (adsorption/desorption) processes, and (iii) redox reactions [5]. These processes, often occurring simultaneously, can be predicted by means of the geochemical modeling or more precisely via the reaction path modeling of water-rock interaction.

Reaction path modeling is a powerful geochemical tool proposed by Helgeson and coworkers in the late 1960s. [6] described the relationships of the irreversible water-rock mass transfer processes on the basis of the fundamental principles of thermodynamics and chemical kinetics. Helgeson and coworkers created PATHI, the first software code for reaction path modeling, and used it to predict different geochemical processes (e.g., [7]). Afterwards, several software packages were developed, such as EQ3/6 [8], SOLVEQ/-CHILLER [9], and PHREEQC [10]. Today, using these software packages, it is possible to investigate several processes of geochemical interest, including weathering (e.g., [11–29]). The study of the rock-to-water release of chemical components and of the chemical evolution of groundwaters allows

one to widen also the knowledge of complex hydrogeological systems.

Because of its large extension over northern Calabria and southern Basilicata regions and its peculiar geological setting, the Pollino National Park hosts a complex hydrogeological system comprising several aquifers, each one with its own geological, hydrogeological, and hydrogeochemical characteristics. In this paper, the main aquifers of the Pollino National Park were studied performing the reaction path modeling of rock dissolution for six different lithotypes cropping out in the study area, which are limestones, Mg-limestones, dolomites, serpentinites, Al-silicate fraction of calcschists, and carbonate fraction of calcschists. This geochemical modeling exercise was carried out adopting an innovative approach, that is, allowing the precipitation of a few secondary solid phases only, namely, opal-CT (low-temperature disordered cristobalite with intergrowth of tridymite layers) or chalcedony, amorphous or crystalline $Al(OH)_3$, and amorphous or crystalline Fe(III)-oxy-hydroxide (HFO). In this way, it was possible to reproduce the whole range of alkalinities measured in local groundwaters, while this target would not have been achieved by allowing the precipitation of carbonate minerals.

Afterwards, the theoretical trends of rock dissolution were compared with the experimental data of 105 groundwaters sampled in the Pollino National Park area and it was ascertained that the concentrations of major solutes, SiO_2, Li, Al, and Fe of local groundwaters, are satisfactorily explained by the dissolution of the considered lithotypes, thus proving the effectiveness not only of the reaction path modeling but also of the adopted approach concerning the secondary solid phases. We are convinced that this approach can also be exported to other areas.

2. Geological and Hydrogeological Background

The Pollino National Park area is part of the southern Apennine fold-and-thrust belt. It is formed by a fold-and-thrust belt-foredeep system that has recorded the east-directed thrust transport and the development and deformation of progressively younger turbiditic deposits to the east. The geology of the area includes a Paleogene Subduction Complex (the Calabro-Lucanian Flysch Unit or the Liguride Complex of Southern Italy), the Middle Miocene foreland strata of the Cilento Group and younger sequences, and the Mesozoic to Miocene carbonate platform and slope (inner Alburni-Cervati-Pollino Units and the Monti della Maddalena Unit); the Campano-Lucanian Ranges, including the Mesozoic to Upper Miocene deep-sea sequences of the Lagonegro and Sicilide Units, the outer platform sequences (Monte Alpi Unit), and the Miocene foreland strata; the Lucanian-Apulia lowland, including the Pliocene to Quaternary clastics; and the Apulian Swell, a Mesozoic to Quaternary carbonate platform [30–34].

The Meso-Cenozoic carbonate successions of the southern Apennines are in contact with the uplifted crystalline rocks of the northern Calabrian Terranes [35–36] (through a regional extensive shear zone identified as the Pollino Line [37–40]).

According to some authors, the stratigraphic and structural lineaments of the area showed the occurrence of main imbricate units; from bottom to top, they are as follows: the metamorphic Lungro-Verbicaro Unit, which consists of a lower terrigenous interval of Early Triassic age, made up of phyllites and metarenites with carbonate intercalations and an upper carbonatic interval. These deposits are followed by metalimestones, marly metalimestones, and dolomites [41]. Carnian layers show a significant increase of siliciclastic beds intercalated with metadolomites, metalimestones, and evaporites. The metalimestones are generally coarse and crystalline and locally exhibit stratification. On top of this lithological interval are red siliceous slates and radiolarite beds passing to coarse carbonate conglomerates and breccias, metapelites. Siliciclastic metadolomites and evaporate strata prevail to the SW, whereas to the NE, the succession is dominated by the carbonate of the Pollino Unit. This carbonate succession overthrust the Pollino-Ciagola Unit resulting in the tectonic window in the Orsomarso Mts. area. The unit comprises carbonate deposits with large and variable stratigraphic gaps occurring in these slope facies successions. The Late Triassic is almost everywhere represented by thick-bedded, white-to-light gray dolomites. The dolomites grade upward to limestones calcareous dark, well-bedded, generally cyclic limestones with characteristic fossiliferous content. They are covered by calcarenites [42] and by Miocene siliciclastic turbiditic deposits which include marls, pelites, and quartz arenites [42, 43].

In the northern part of the study area, carbonate units are overthrust by nappes belonging to continental and oceanic domains. Remnants of crystalline basement rocks such as gneiss and granite outcrop at the top of tectonic assemblage or result englobed in the ophiolite-bearing nappes of the Liguride Complex. The complex comprises ophiolite-bearing units made up of serpentinites, gabbros, and pillow basalts; the metamorphic Frido Unit; and the unmetamorphosed North Calabrian Unit [44]. The latter crops out in the proximity of the NE sector of the Pollino Massif, in the Calabria-Lucania border area. The Frido Unit is constituted by blackish schists, metarenites, greenish quartzites, and calcschists. The rocks incorporate the ophiolitic rocks and thrust on the Calabro-Lucanian Flysch Unit [31]. This is the lowermost geometric unit of the Liguride Complex [44] and crops out extensively in the northeastern part of the area, which tectonically lies on the carbonate units. It consists of a thick alternation of gray-brown flaked shales, quartz siltites and quartz sandstones, marly calcilutites, and calcarenites. As a whole, it shows the structural and textural characteristics of a broken formation and tectonically incorporates blocks of the ophiolite-bearing rocks and relatively sedimentary cover and blocks of the Crete Nere Formation, consisting of black shales, quartz siltites, cherty limestones, and calcilutites and marly limestones with intercalations of grayish argillites. Oligocene to Miocene deposits consisting of turbiditic calcareous and terrigenous flysch have been considered together with the sedimentary succession of Jurassic-Miocene age (Figure 1).

On the top of the entire tectonic edifice rests the terrigenous succession of Upper Miocene-Pleistocene marine and continental intramountain basins [45, 46].

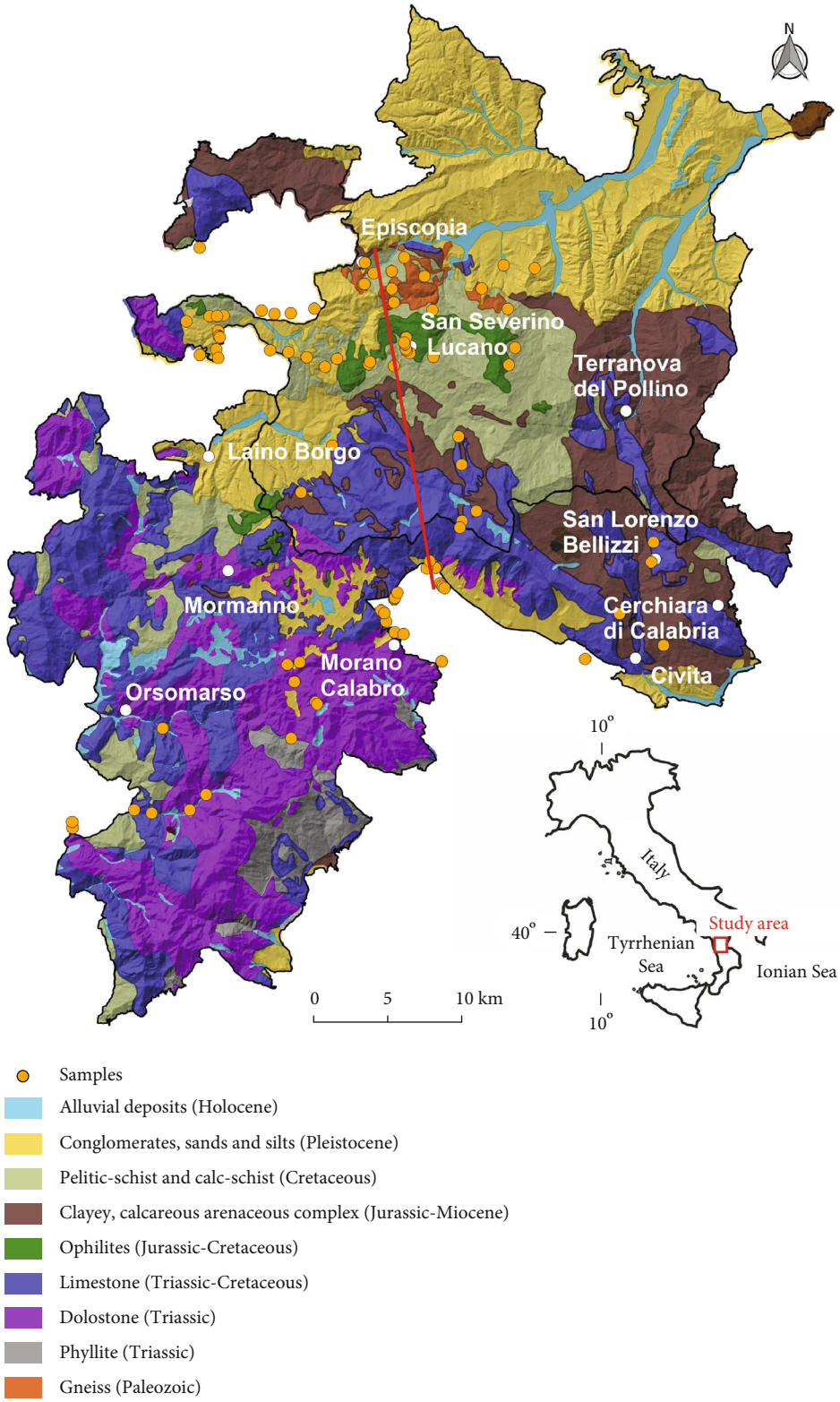

Figure 1: Lithological map of the Pollino National Park area. In the figure, the trace (red line) of the schematic geological section (see Figure (Figure 9) and the location of all considered samples are reported.

The fold-and-thrust system is the result of accretionary wedge overthrust and collisional processes that realized eastern and western thrust propagation [45, 47–50]. The latest tectonic event is characterized mostly by strike-slip faulting and associated positive and negative structures [39, 51]. The fault systems (i.e., NW-SE, N-S, and NE-SW oriented)

are responsible for the severe dissection of the mountain belt into discrete crustal blocks alternating structural high to elongated structural depressions.

The study area is characterized by hydrogeological complexes which highlight differences in terms of flow rates and depth. Throughout the area, it is possible to recognize three main hydrogeological complexes:

(i) Carbonate-dolomitic complex

(ii) Crystalline-metamorphic complex

(iii) Terrigenous-calcareous in flysch facies complex

The carbonate-dolomitic complex includes aquifers hosted in limestones, dolostones, chert-bearing limestones, and marly limestones. The complex represents one of the main sources of drinking water supplies in Calabria, Southern Italy [52–58]. These lithotypes, due to the brittle characters and the sin- and postorogenic tectonic evolution, identify a dominant fractured cleavage permeable aquifer. Moreover, due to their typical chemical composition, they are subject to karst phenomena through which the action of dissolving rainwater tends to expand the network of preexisting fractures. These characteristics promote high infiltration processes with values between 85% and 95% [52]. The main spring flow rates in the order of hundreds l/s [59, 60] are located in the proximity of the hydrogeological boundaries constituted of fine and impermeable deposits or along the main faults that play the role of the flow zone and/or permeability threshold [52, 59, 60].

The Liguride Units, except for the respective sedimentary covers, can be grouped in the crystalline-metamorphic complex [52]. This group, if compared with the carbonate-dolomitic complex, represents a minor hydrogeological structure. The aquifers are directly linked both to the thickness of gneisses and granites (alteration) and to the state of fracturing of the rock mass. Low-grade metamorphites represent a water system conditioned by fracturing and above all by vertical lithological anisotropy.

There are also aquifers of lesser importance, represented by lithostratigraphic units included in basin sedimentary succession and flysch facies, well represented in the study area. These aquifers are affected by the alternation of fine and coarse materials and tend to give multiaquifer water systems with higher productivity in the conglomeratic-arenaceous intervals.

3. Materials and Methods

3.1. Water Sampling and Analysis. A total of 62 water samples from the Pollino National Park area were collected during the present study and analyzed for major components. The sampling methodologies were already described by [61–66]; however, a brief description is reported here. In the field, the physicochemical parameters like temperature, pH, oxidation-reduction potential (Eh), and electrical conductivity (EC) were determined by using a previously calibrated multiparametric probe (Hanna Instruments HI-9828) whereas total alkalinity was determined by acidimetric titration using HCl 0.05 N as the titrating agent and methyl orange as the indicator. Each water sample was filtered in the field via a 0.45 μm pore-size membrane filter. Samples for the determination of cations, SiO_2, and trace elements were acidified by the addition of pure acid (1% HNO_3) whereas samples for the determination of anions were stored without further treatment. The concentrations of Na^+, K^+, Mg^{2+}, Ca^{2+}, F^-, Cl^-, SO_4^{2-}, and NO_3^- were determined by high-performance liquid chromatography (HPLC, Dionex DX 1100). Some trace elements such as Fe and Al were determined by a quadrupole inductively coupled plasma-mass spectrometer (ICP-MS, PerkinElmer/SCIEX, ELAN DRC-e) with a collision reaction cell capable of reducing or avoiding the formation of polyatomic spectral interferences. Data quality was evaluated by charge balance for major ions (±10%) and by running NIST 1643f standard reference solution for trace elements with deviation from certified concentration below the ±10%. Moreover, the concentration of SiO_2 was measured by means of VIS spectrophotometry. These 62 water samples were added to previous data collection provided by [67] (the reader should refer to the original work for the methods of water sampling and analysis used by authors), and all 105 samples were used in this work (Table S1 in Supplementary Materials).

3.2. Geochemical Modeling. Reaction path modeling of rock dissolution was performed using the software package EQ3/6 [8] and a revised version of the thermodynamic database of [68].

Reaction path modeling of rock dissolution was carried out in a purely stoichiometric mode, referring to the reaction progress variable, ξ, without any time provision, that is, leaving aside the kinetics of the irreversible water-rock mass exchanges. This means that at each ξ step, a corresponding amount of the solid reactant is added to the system made up of the aqueous solution and secondary solid phases if any. The added solid reactant is dissolved, and the aqueous solution is reequilibrated with the instantaneously precipitating product phases if any [69].

Although reaction path modeling in a stoichiometric mode implies that all rock-forming minerals are assumed to dissolve at the same rate (which is surely not true), in this approach, it is not necessary to specify for the relevant minerals neither the surface areas, which are nothing but educated guesses in many cases, nor the dissolution-precipitation rates, which are constrained by laboratory experiment results often diverging from field data. To be noted also, the stoichiometric approach is reasonable for monomineralic rocks like the carbonate rocks and the serpentinites.

In the adopted approach, the rocks of interest are considered "special reactants," that is, materials of known stoichiometry and unknown thermodynamic properties [69]. Following the indications of the EQ3/6 manuals, concentrations of chemical elements in special reactants were expressed in mol/kg.

Calculations were carried out assuming a closed system for secondary solid phases. This means that the precipitating solid phases remain in the considered system and are in equilibrium with the aqueous solution for the whole duration of

Table 1: Elemental composition of the six solid reactants considered in reaction path modeling of rock dissolution.

Element	Dolomite mol/kg	Mg-limestone mol/kg	Limestone mol/kg	Carbonate-calcschist mol/kg	Al-silicate calcschist mol/kg	Serpentinite mol/kg
H	—	—	—	—	—	1.24E + 01
Li	2.26E − 04	8.62E − 04	3.92E − 04	7.20E − 04	9.51E − 03	4.49E − 04
C	1.96E + 01	1.87E + 01	1.94E + 01	7.45E + 00	—	—
O	3.93E + 01	3.79E + 01	3.93E + 01	1.49E + 01	2.69E + 01	3.16E + 01
Na	6.91E − 01	2.44E − 01	1.58E + 00	5.39E − 01	4.58E − 01	1.86E + 00
Mg	9.55E + 00	1.64E + 00	2.46E − 01	1.64E − 01	8.71E − 01	9.20E + 00
Al	5.97E − 03	1.08E − 01	6.91E − 03	—	4.57E + 00	3.57E − 01
Si	4.72E − 02	1.66E − 01	2.12E − 01	—	8.27E + 00	6.25E + 00
S	—	—	—	—	—	6.42E − 04
Cl	—	—	—	—	—	3.07E − 03
K	1.67E − 03	1.72E − 02	2.02E − 03	3.76E − 02	8.28E − 01	1.12E − 03
Ca	9.35E + 00	1.68E + 01	1.76E + 01	6.53E + 00	1.82E − 01	1.04E − 01
Fe	2.45E − 03	1.58E − 02	3.38E − 03	1.43E − 01	1.17E + 00	1.33E + 00

the simulation. Hence, they can be redissolved if the aqueous solution becomes undersaturated.

An open system was instead assumed for gases, namely, O_2(g) and CO_2(g). In other terms, the system is considered to be connected to two infinitely large gas reservoirs, one of O_2(g) and the other of CO_2(g), which fix the partial pressure of these two gases to the chosen values. Indeed, simulations were performed at a constant temperature of 12°C, log f_{CO_2} of -2.6 log bar and log f_{O_2} of -25 log bar.

3.2.1. The Solid Reactants. Six different solid reactants were considered: a limestone, an Mg-limestone, a dolomite, and a serpentinite, as well as the carbonate and Al-silicate end-members of a calcschist. These six rocks were sampled in the Pollino National Park. The chemical composition was obtained by means of Scanning Electron Microscopy-Energy-Dispersive Spectra (SEM-EDS) analysis and through X-ray fluorescence spectroscopy (XRF) analysis performed during this study in the laboratories of DiBEST, University of Calabria, and provided by previous investigations [15, 70, 71]. The computed elemental compositions of the six solid reactants are given in Table 1.

3.2.2. The Solid Products. To keep the model to a simple level, only few oxy-hydroxides were allowed to precipitate as secondary (alteration) phases, including a silica mineral, an aluminum hydroxide, and a ferric oxy-hydroxide (HFO). Among the different silica minerals, chalcedony precipitation was allowed when the availability of SiO_2 is low, that is, during the dissolution of the carbonate rocks (dolomite, Mg-limestone, limestone, and the carbonate fraction of the calcschist), whereas opal-CT production was permitted when the availability of SiO_2 is high, that is, during the dissolution of the serpentinite and the Al-silicate fraction of the calcschist. As a general rule, the amorphous oxy-hydroxides of Al and Fe(+3) have a higher solubility than their crystalline and higher precipitation rate as well. Owing to the lower solubility, the crystalline phases should precipitate before the amorphous oxy-hydroxides, but this event usually does not take place because the precipitation kinetics of crystalline phases is slow. Owing to the lack of precipitation of the crystalline phases, the aqueous solution may become supersaturated with the amorphous phases, which precipitate readily due to their fast precipitation kinetics. Actually, the process is more complicated, comprising the reversible, rapid growth of small polymers and the subsequent formation of slowly reacting large polymers before the precipitation of ferric oxy-hydroxides (e.g., [72]). Based on these considerations, two distinct runs were performed for each solid reactant, allowing the precipitation of amorphous $Al(OH)_3$ and amorphous HFO, in a series of runs, and permitting the production of gibbsite and crystalline HFO in a separate series of simulations. Chalcedony, opal-CT, gibbsite, amorphous $Al(OH)_3$, and crystalline and amorphous HFO were assumed to be pure minerals.

3.2.3. Initial Aqueous Solutions. The concentrations of major dissolved constituents in the initial aqueous solution were reconstructed based on the results of the chemical analyses of rainwater periodically sampled in the Cosenza area, apart from total carbonate concentration which was assumed to be constrained by the electrical charge balance. Aluminum concentration was obtained by forcing equilibrium with gibbsite. The concentration of Fe in rainwater, $C_{Fe,RW}$, was computed using the simple relation:

$$C_{Fe,RW} = C_{Fe,SW} \cdot \left(\frac{C_{Cl,RW}}{C_{Cl,SW}}\right), \quad (1)$$

where $C_{Cl,RW}$ and $C_{Cl,SW}$ are the average Cl concentration of rainwater and seawater, respectively, and $C_{Fe,SW}$ is the concentration of Fe in average seawater. The adopted average seawater composition is from [73]. Equation (1) is based on

Table 2: Elemental composition of the initial aqueous solution for $T = 12^{\circ}C$, pH = 6.80, and Eh = 837 mV.

Element	mg/kg·sol	mol/kg
Al	$4.73E-05$	$1.75E-09$
C	$5.10E+00$	$4.25E-04$
Ca	$6.00E+00$	$1.50E-04$
Cl	$1.70E+00$	$4.80E-05$
Fe	$7.00E-04$	$1.25E-08$
K	$1.80E-01$	$4.60E-06$
Li	$1.00E-05$	$1.44E-09$
Mg	$7.00E-01$	$2.88E-05$
N	$2.26E-01$	$1.61E-05$
Na	$1.50E+00$	$6.52E-05$
S	$1.07E+00$	$3.33E-05$
Si	$1.17E+00$	$4.16E-05$

a reasonable approximation since rainwaters in near-coastal regions, like the Pollino National Park, are essentially heavily diluted seawater [74]. The log P_{CO2} of the initial aqueous solution was assumed to be -2.6, which is close to the mean value of spring waters. Having specified both the P_{CO2} and the total carbonate concentration, pH is fixed and turns out to be 6.80. The redox potential was constrained by the log P_{O2} of -0.678, which is the mean atmospheric value. Results of the EQ3 run for the initial aqueous solution are given in Table 2.

3.2.4. The Refurbishing of the Thermodynamic Database. As already mentioned above, reaction path modeling of rock dissolution was carried out referring to the thermodynamic database of [68], which was modified adopting the solubilities of chalcedony and opal-CT given by [75]. Moreover, the equilibrium constant values of the dissolution reaction of the oxy-hydroxides of Al and Fe^{3+} were adjusted to suitably selected values in order to bracket the measured total concentrations of these dissolved constituents.

4. Results and Discussion

4.1. Water Chemistry. The considered spring waters have outlet temperatures ranging from 4.5 to 17.1°C, with mean 11.1°C, median 11.4°C, and standard deviation 2.3°C. These different outlet temperatures are partly controlled by the distinct elevation, from 212 to 1536 m asl, and partly reflect the different sampling periods. These groundwaters are scarcely mineralized, as indicated by the relatively low values of the electrical conductivity, varying from 67 to 841 μS/cm, with mean 426 μS/cm, median 402 μS/cm, and standard deviation 140 μS/cm. The highest conductivities were recorded for the three samples of the sulfide-bearing Abatemarco springs (codes 16, 17, and A24), which are also characterized by unusual low Eh S(-2)-S(0) values, -139 to -150 mV (calculated by geochemical modeling), and chemistry. The Eh values measured by means of the Pt electrode for all the other springs are in the interval +34 to +305 mV, with mean +154 mV, median +157 mV, and standard deviation 65 mV. These relatively high redox potentials are indicative of prevailingly oxidizing conditions, as expected for shallow waters. However, it is unlikely that measured Eh values are controlled by one of the two electroactive redox couples to which the Pt electrode is sensitive, i.e., the Fe(+2)-Fe(+3) and S(-2)-S(0) systems [76], owing to the low concentrations of iron and reduced sulfur species in these aqueous solutions. The pH values oscillate around the neutrality conditions, from 6.83 to 8.86, with mean 7.65, median 7.6, and standard deviation 0.40. The logarithm of the computed CO_2 partial pressure, which depends largely on pH, varies from -3.65 to -1.60, with mean -2.39, median -2.37, and standard deviation 0.42 (all in log bar). Eighty-three samples have log P_{CO2} values within the range of worldwide soils, -2.70 to -1.40 log bar [77], indicating that CO_2 is chiefly contributed to water by processes occurring in soils, such as the decay of organic matter and root respiration. The remaining twenty-two samples have lower log P_{CO2} values, but all except one are higher than the mean atmospheric log P_{CO2}, -3.50 log bar. Therefore, it is likely that these low log P_{CO2} values are controlled by gas exchanges between the aqueous solutions and the atmosphere.

As shown by the triangular diagram of major anions (Figure 2(a)), bicarbonate is the prevailing anion in all the waters apart from the three samples of the sulfide-bearing Abatemarco springs (codes 16, 17, and A24), which have comparable concentrations of SO_4 and HCO_3. The almost-ubiquitous prevalence of bicarbonate suggests that the mineralization of most waters is chiefly controlled by rock dissolution driven by conversion of CO_2 into HCO_3^- ion.

In the triangular diagram of main cations (Figure 2(b)), all the water samples are distributed near the axis connecting the vertices of Ca and Mg, since the sum of the relative concentrations of Na and K is less than 20 eq% apart from sample A21. This sample has the lowest conductivity, 67 μS/cm, but unusually higher concentrations of Na and Cl, 25 and 24 eq%, respectively, which are probably related to the marine-atmospheric component. In other words, sample A21 is rainwater scarcely modified by water-rock interaction. Based on the Ca/(Ca+Mg) molar ratio, it is possible to recognize thirty calcic waters, with values higher than 0.75, sixty-three calcic-magnesian waters, with values in the interval 0.50 to 0.75, and twelve magnesian waters with values lower than 0.50.

Taking into account the indications provided by the two triangular diagrams of Figure 2, the considered spring waters were provisionally ascribed to the following three chemical types: Ca-HCO_3, Ca(Mg)-HCO_3, and Mg-HCO_3.

The diagram of Figure 2(b) also shows the expected compositions for (i) dissolution of calcite, coinciding with the Ca vertex, (ii) dissolution of dolomite, located along the axis connecting the vertices of Ca and Mg at equal distance from both vertices, and (iii) dissolution of magnesite, coinciding with the Mg vertex. Therefore, one might be tempted to conclude that the Ca-HCO_3 waters originate by prevailing dissolution of calcite and subordinate dissolution of dolomite, the Ca(Mg)-HCO_3 waters are generated by predominant dissolution of dolomite accompanied by minor dissolution of

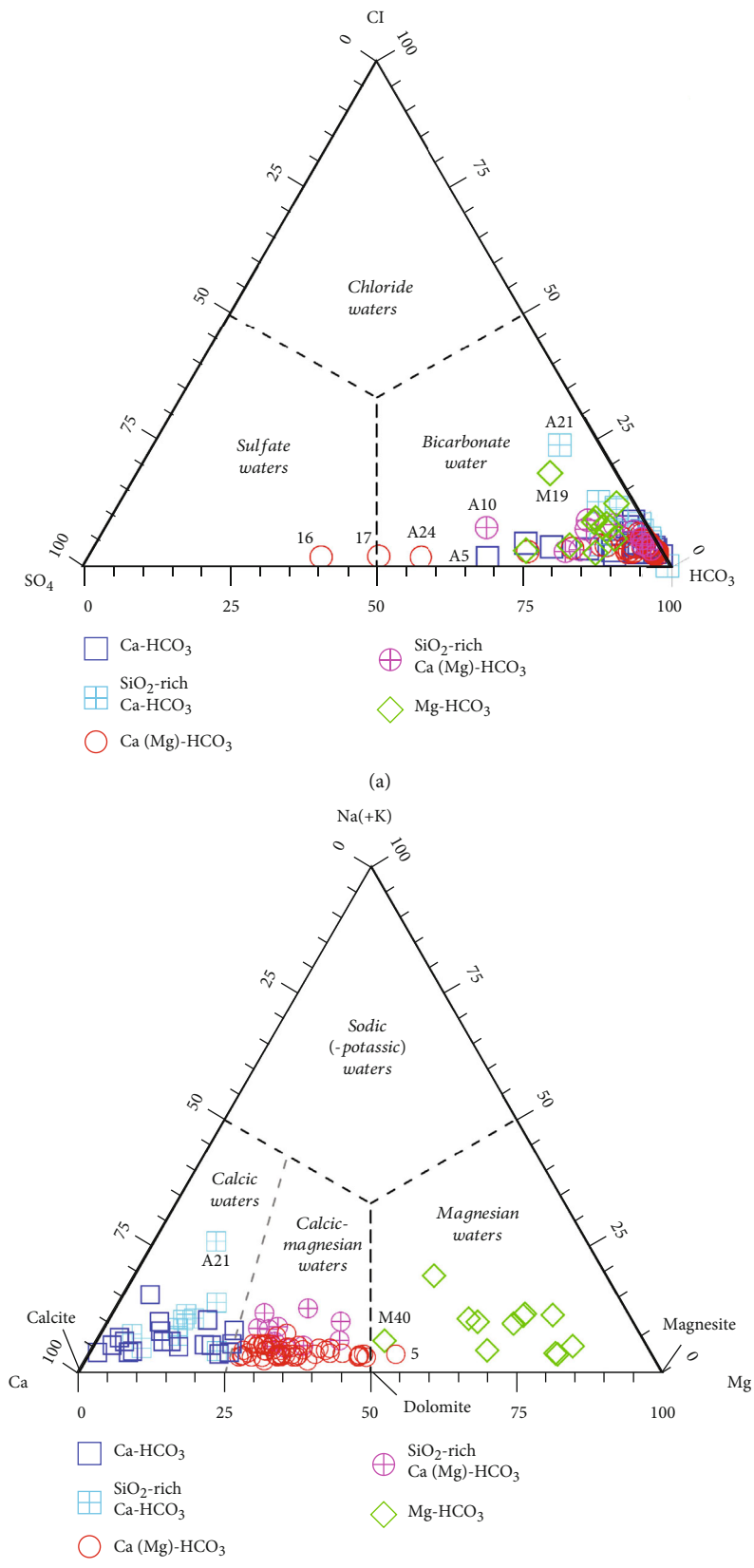

Figure 2: Triangular diagrams of the main anionic (a) and cationic (b) constituents for the spring waters of the Pollino National Park (concentration in equivalent units).

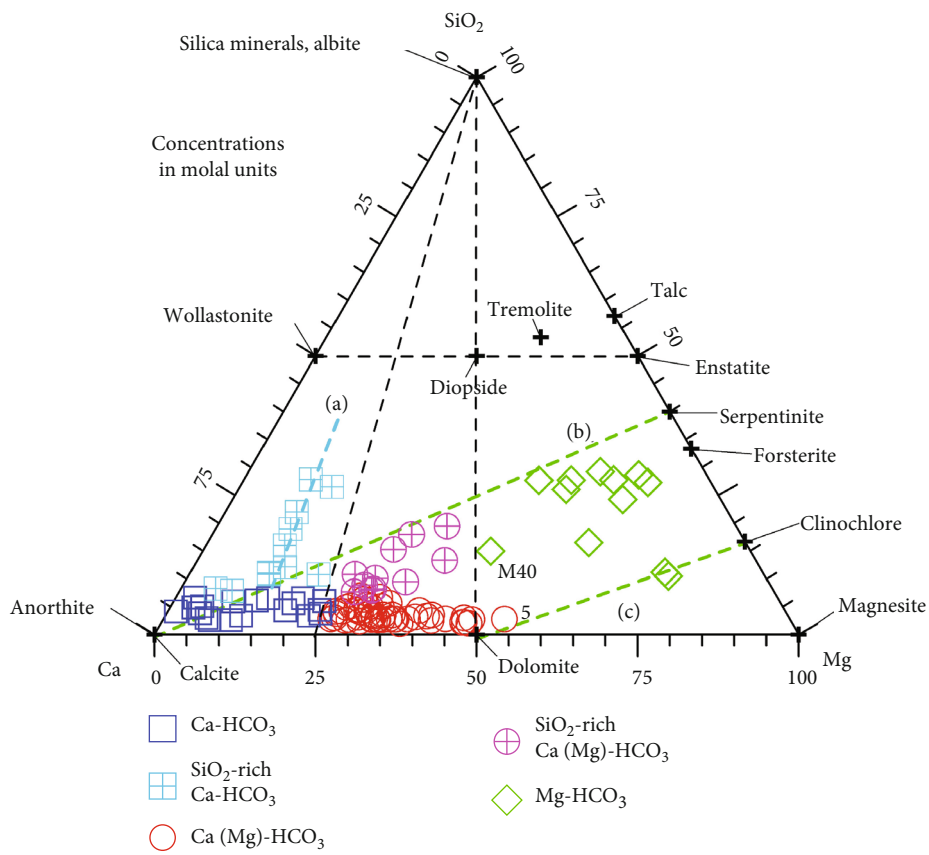

Figure 3: Triangular diagram of Ca-Mg-SiO_2, for the spring waters of the Pollino National Park (concentrations in molal units).

calcite, and the Mg-HCO_3 waters are produced by dissolution of magnesite and dolomite in different proportions. These inferences may be right for the Ca-HCO_3 and Ca(Mg)-HCO_3 waters originated by the interaction of meteoric waters with carbonate rocks only, but they are probably wrong for the Ca-HCO_3 and Ca(Mg)-HCO_3 waters deriving by the interaction of meteoric waters with both carbonate rocks and Al-silicate rocks or with mixed rocks like the calcschists, comprising a carbonate fraction and an Al-silicate fraction, or even with Al-silicate rocks only, given the fact that they often contain veins of calcite or dolomite. To be noted also, the Ca-HCO_3 and Ca(Mg)-HCO_3 waters somehow related to Al-silicate rocks are expected to be rather common because these lithotypes extend over vast sectors of the Pollino National Park area (Figure 1). Furthermore, the Mg-HCO_3 waters are unlikely to be produced by the dissolution of magnesite, since monomineralic rock bodies exclusively made up of magnesite (or almost so), analogous to limestones and dolomites, are rare [78, 79].

The waters probably affected by the dissolution of Al-silicate rocks were selected based on values of the TIS/SiO_2 ratio lower than 50, where TIS is the acronym of total ionic salinity, representing the sum of the concentrations of major cations and anions, in meq/kg, and SiO_2 concentration is expressed in mmol/kg. Most of the springs discharging these waters are found in areas where Al-silicate rocks crop out. After this further classification step, the spring waters were finally attributed to one of the following five chemical types: Ca-HCO_3, SiO_2-rich Ca-HCO_3, Ca(Mg)-HCO_3, SiO_2-rich Ca(Mg)-HCO_3, and Mg-HCO_3.

To elucidate the role played by the dissolution of Al-silicate rocks, it is advisable to take into consideration the triangular diagram of Ca-Mg-SiO_2 (Figure 3), in which the chemical characteristics of the spring waters of interest are compared with the compositions expected for dissolution not only of carbonate minerals but also of several Si-bearing minerals, which are probably present in local Al-silicate rocks, such as quartz, talc, enstatite, serpentine, forsterite, clinochlore, tremolite, diopside, wollastonite, anorthite, and albite. The dissolution reactions of considered minerals are based on the following two hypotheses [80]. (1) The water-rock interaction processes, in which carbonate and silicate minerals are dissolved, can be assimilated to acid-base titrations, in which the minerals act as bases, while aqueous CO_2 is the acid that controls the process and is converted into HCO_3^- ion. (2) Aluminum released by the dissolution of the primary Al-silicates, such as clinochlore and plagioclases, is entirely incorporated into precipitating kaolinite, although other secondary Al-bearing solid phases may form instead of it, leading to different water compositions [16].

Even though several other Si-bearing minerals might be present in local rocks in addition to those considered so far, the latter ones are sufficient for explaining the chemistry of the water samples of interest. In fact, in Figure 3, most Si-rich Ca-HCO_3 waters are positioned along trend (a), which is controlled by the dissolution of quartz and/or other silica

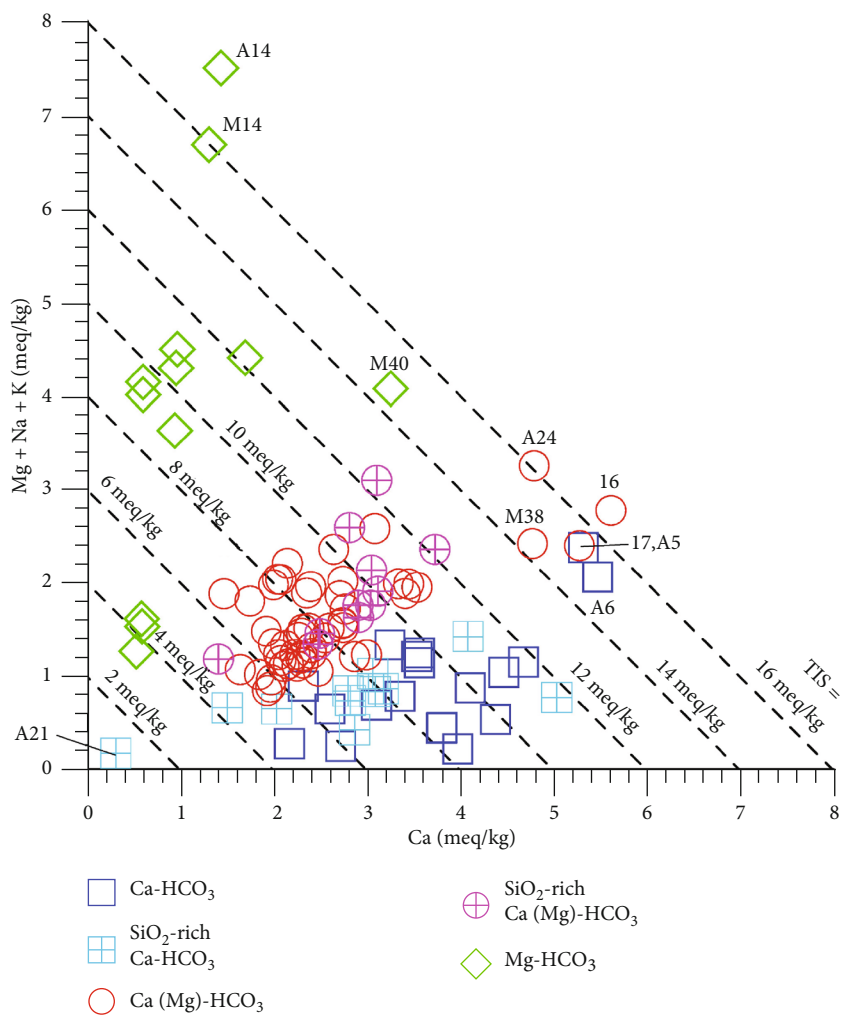

Figure 4: Correlation diagram of Ca vs. Mg+Na+K for the spring waters of the Pollino National Park in which the isolines of total ionic salinity (iso-TIS lines) are reported.

minerals and/or albite, suggesting that these waters probably interact, at least partially, with acid rocks or, alternatively, with chert-bearing limestones. The Si-rich Ca(Mg)-HCO_3 waters and the Mg-HCO_3 waters are positioned between the serpentine-calcite tie line (b) and the clinochlore-dolomite tie line (c), suggesting that their chemical characteristics are probably controlled by the dissolution of these four minerals. However, the possible contribution of forsterite dissolution cannot be excluded because it would determine water compositions intermediate between those controlled by serpentine and clinochlore dissolution. Also, magnesite dissolution represents a plausible option, at least for the Mg-HCO_3 waters characterized by high Mg/SiO_2 ratios. The Si-rich Ca(Mg)-HCO_3 waters probably interact, at least partially, with mafic or ultramafic rocks.

Since the triangular plots of Figures 2 and 3 do not convey any information on total ionic salinity, this parameter is inspected by means of the correlation diagram of Ca vs. Mg +Na+K (Figure 4), in which the TIS values of the considered spring waters can be appreciated by comparing the position of each sample with the lines of slope -1 which are iso-TIS lines (see [81] for further details). It turns out that most spring waters have TIS of 3.6 to 12.9 meq/kg, irrespective of the chemical type they belong to, apart from sample A21 which has TIS of 1 meq/kg only and nine samples with TIS of 14.4 to 18.4 meq/kg, including the sulfide-bearing Abatemarco springs (codes 16, 17, and A24). Finally, the acquired chemical information showed that the concentrations of Al, Cl, F, NO_3, and SO_4 are within the threshold values recommended by the World Health Organization (WHO) [82] which established the guidelines for drinking water quality.

4.2. Reaction Path Modeling. Results of reaction path modeling onto precipitating HFO are reported adopting alkalinity as a proxy for the reaction progress variable [16]. This choice is based on the fact that progressive rock dissolution can be considered a sort of acid-base titration, in which the base is the rock and the acid is $CO_{2(aq)}$, which is converted to HCO_3^- ion, as pointed out long ago by [80].

4.2.1. The Precipitating Solid Phases. Based on the simulations performed in this work, the precipitating solid phases during the gradual dissolution of the limestone, the Mg-limestone, the dolomite, and the serpentinite, as well as the

Table 3: Precipitating solid phases during the simulations of the progressive dissolution of the limestone, the Mg-limestone, the dolomite, and the serpentinite, as well as the carbonate and Al-silicate endmembers of the calcschist considered in this work.

Dissolving rock	Type of precipitating minerals	Precipitating minerals
Limestone	Amorphous	$Al(OH)_3$(am), HFO(am)
Limestone	Crystalline	Gibbsite, HFO(cr)
Mg-limestone	Amorphous	$Al(OH)_3$(am), HFO(am)
Mg-limestone	Crystalline	Gibbsite, HFO(cr)
Dolomite	Amorphous	$Al(OH)_3$(am)
Dolomite	Crystalline	Gibbsite, HFO(cr)
Calcschist, Al-silicate endmember	Amorphous	$Al(OH)_3$(am), HFO(am), opal-CT
Calcschist, Al-silicate endmember	Crystalline	Gibbsite, HFO(cr), opal-CT
Calcschist, carbonate endmember	Amorphous	HFO(am)
Calcschist, carbonate endmember	Crystalline	HFO(cr)
Serpentinite	Amorphous	$Al(OH)_3$(am), HFO(am), opal-CT
Serpentinite	Crystalline	Gibbsite, HFO(cr), opal-CT

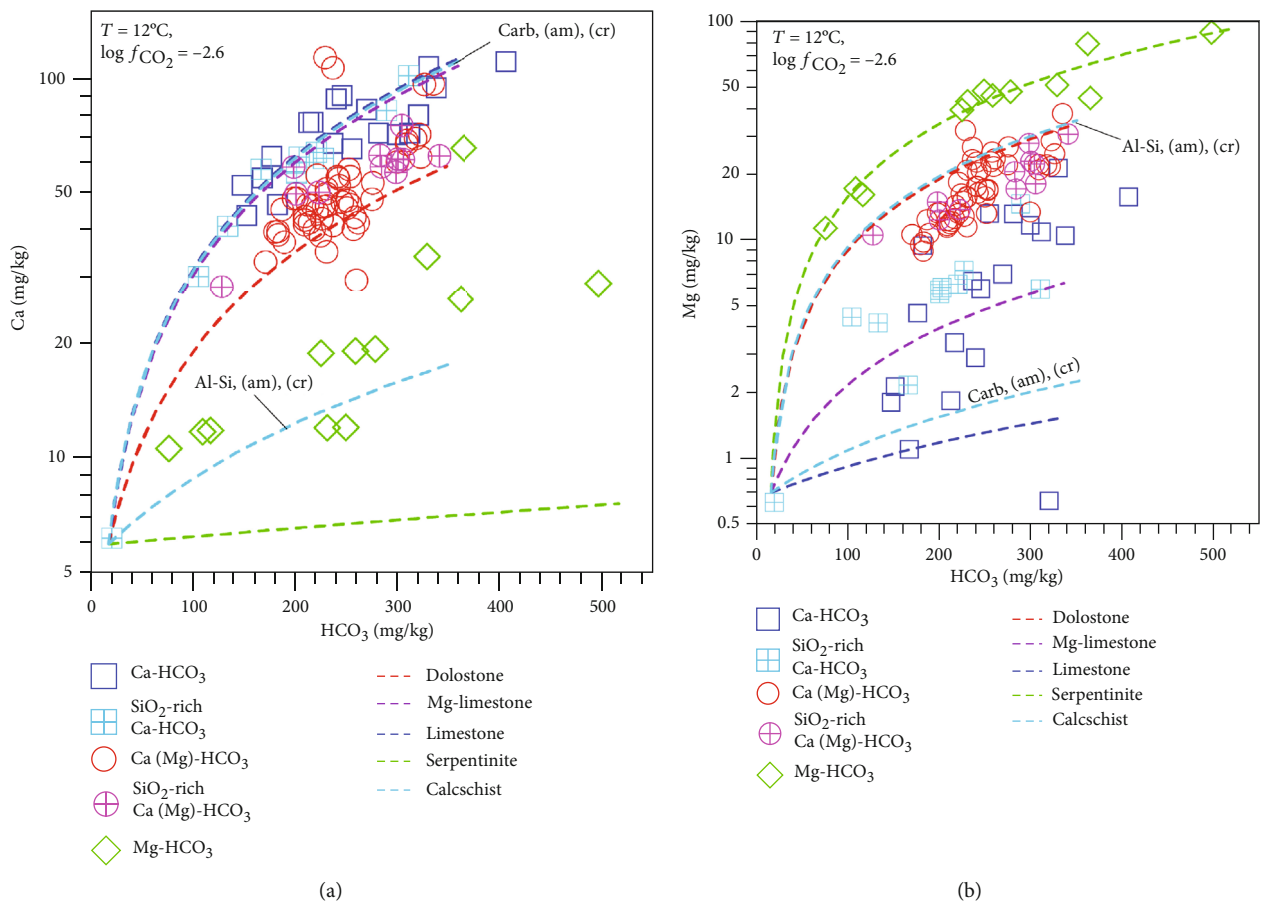

Figure 5: Correlation diagrams of alkalinity (expressed in mg HCO_3/kg) vs. (a) calcium and (b) magnesium during the progressive dissolution of different rocks (see legend) according to the simulations elaborated in this work.

carbonate and Al-silicate endmembers of the calcschist are summarized in Table 3.

Table 3 shows that amorphous or crystalline HFO forms as secondary minerals in all the simulations, except the dolomite dissolution with possible precipitation of amorphous minerals, in which the aqueous solution does not attain saturation with amorphous HFO. Amorphous $Al(OH)_3$ and gibbsite precipitate in all the simulations apart from the dissolution of the carbonate endmember of the calcschist, which was assumed to be Al- and Si-free. Opal-CT is a solid phase only in the simulations in which the serpentinite and the Al-silicate endmember of the calcschist are dissolved.

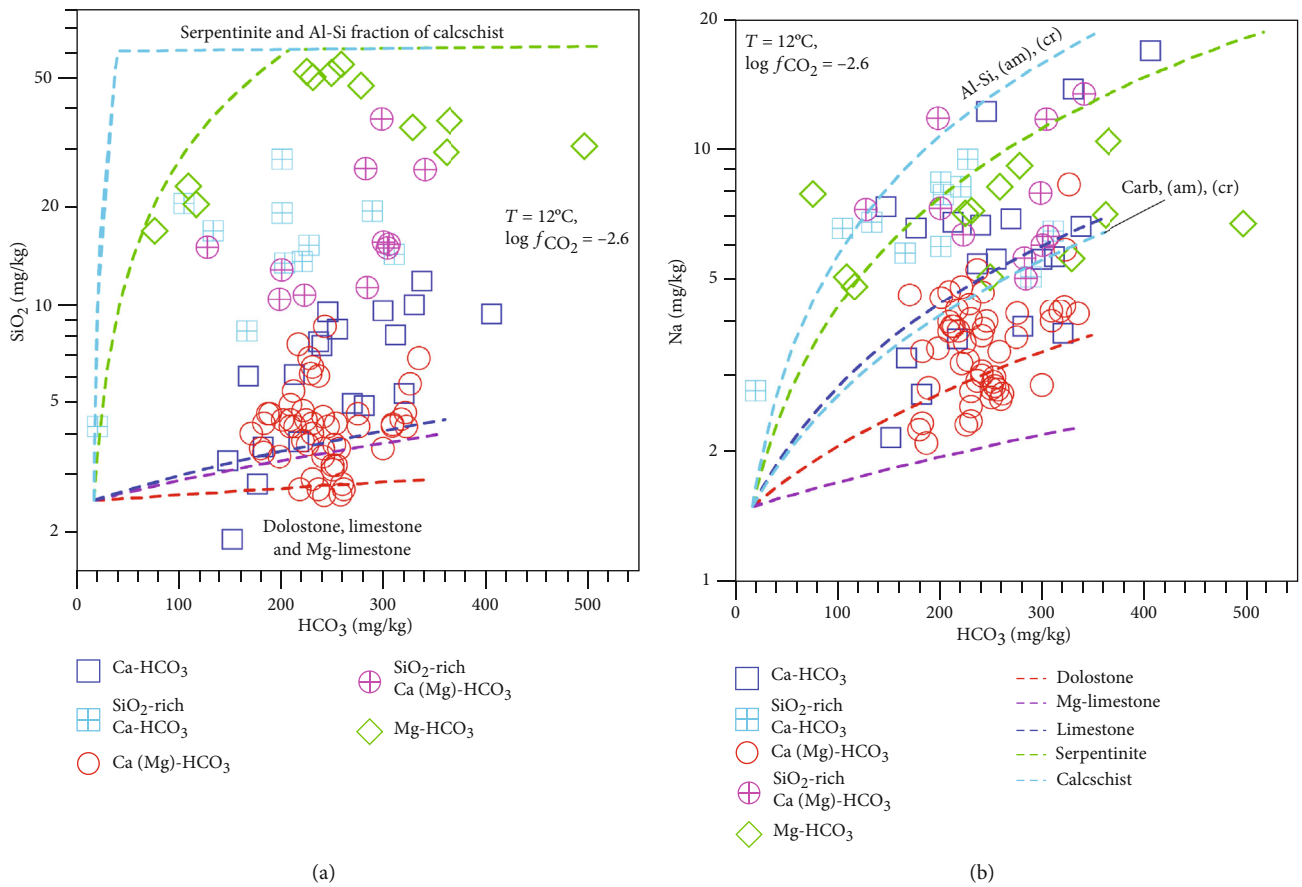

Figure 6: Correlation diagrams of alkalinity (expressed in mg HCO_3/kg) vs. (a) silica and (b) sodium during the progressive dissolution of different rocks (see legend) according to the simulations elaborated in this work.

Chalcedony precipitation never takes place, although it was allowed during the dissolution of the carbonate rocks, i.e., the dolomite, the Mg-limestone, the limestone, and the carbonate endmember of the calcschist. Evidently, the aqueous solution remains undersaturated with respect to chalcedony during the dissolution of these carbonate rocks.

4.2.2. The Aqueous Solutions

(1) Calcium and Magnesium. In the correlation diagram of alkalinity vs. calcium (Figure 5(a)), (i) the Ca-HCO_3 waters and the SiO_2-rich Ca-HCO_3 waters are found along or close to the dissolution curves of the limestone, the Mg-limestone, and the carbonate endmember of the calcschist, which are superimposed on each other, whereas (ii) the Ca(Mg)-HCO_3 waters and the SiO_2-rich Ca(Mg)-HCO_3 waters are situated between the previous curves and that describing the dissolution of the dolomite (apart from a few exceptions). Moreover, all these waters are situated far from the dissolution curve of the Al-silicate endmember of the calcschist. This spread of sample points indicates that the Ca-HCO_3, SiO_2-rich Ca-HCO_3, Ca(Mg)-HCO_3, and SiO_2-rich Ca(Mg)-HCO_3 waters are produced through the dissolution of different carbonate rocks, in variable proportions, whereas the dissolution of the Al-silicate endmember of the calcschist does not seem to contribute significantly to the mineralization of these waters. The Mg-HCO_3 waters are positioned above the serpentinite dissolution curve, probably due to the presence of small amounts of calcite, which is readily dissolved, inside these rocks and/or related soils.

In contrast to what was observed in the previous plot, the dissolution curves of the limestone, the Mg-limestone, and the carbonate endmember of the calcschist are clearly separated in the correlation diagram of alkalinity vs. magnesium (Figure 5(b)) and are all located well below the dolomite dissolution curve. As expected, the Ca(Mg)-HCO_3 and SiO_2-rich Ca(Mg)-HCO_3 waters are found close to the dolomite dissolution curve, whereas the Ca-HCO_3 and SiO_2-rich Ca-HCO_3 waters (apart from a single exception) have lower Mg concentrations and are situated below the dolomite dissolution curve and above the limestone dissolution curve. This spread of sample points confirms that all these waters are originated through the dissolution of these distinct carbonate rocks, in variable proportions. The Mg-HCO_3 waters are situated along the serpentinite dissolution curve or close to it, as expected. All in all, there is a very good correspondence between the theoretical rock dissolution curves and the analytical data of Ca, Mg, and alkalinity for the groundwaters of interest.

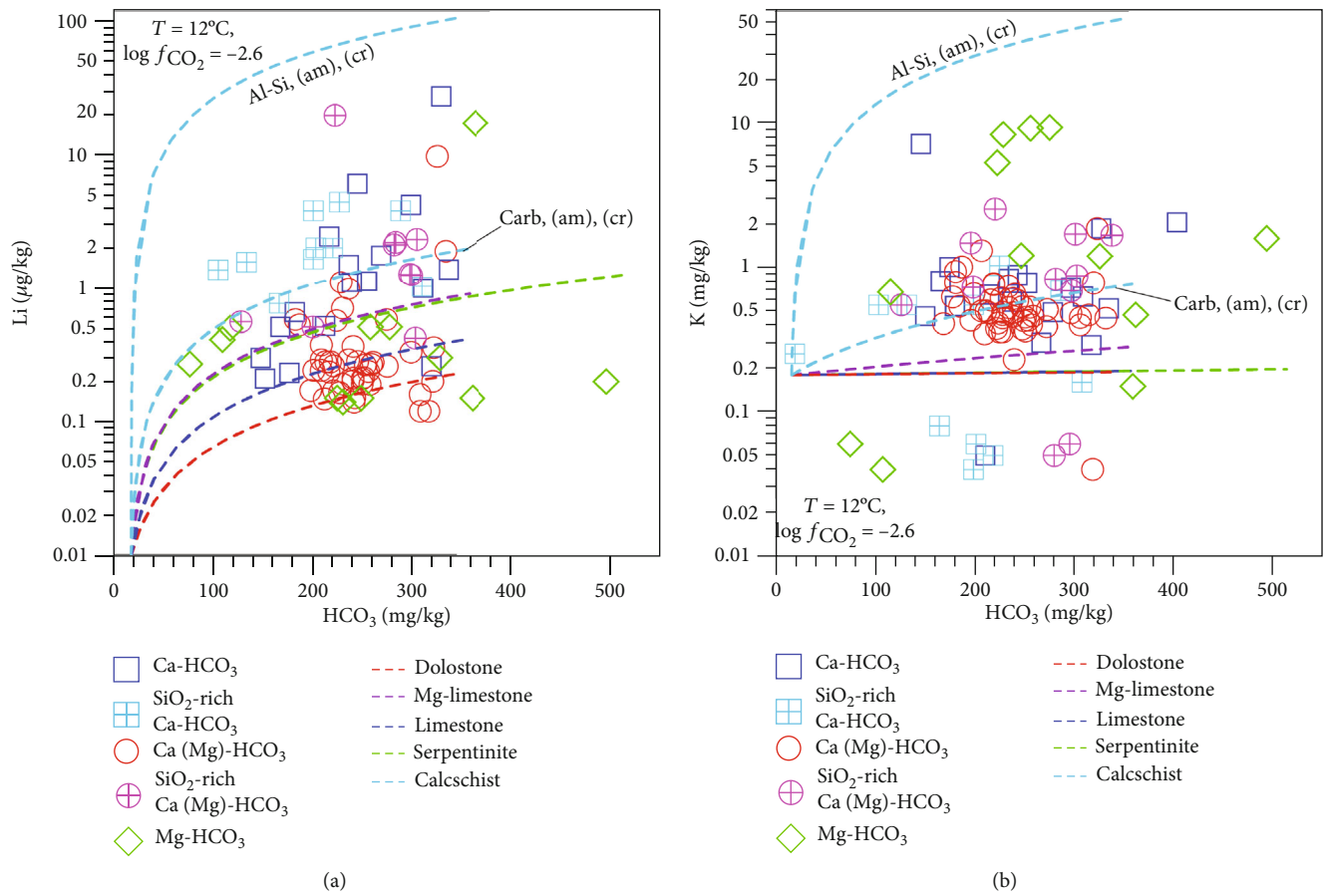

Figure 7: Correlation diagrams of alkalinity (expressed in mg HCO_3/kg) vs. (a) lithium and (b) potassium during the progressive dissolution of different rocks (see legend) according to the simulations elaborated in this work.

(2) Silica and Sodium. Relatively low concentrations of both silica and sodium are expected for dissolution of the carbonate rocks, whereas comparatively high concentrations of both silica and sodium are predicted for dissolution of the Al-silicate endmember of the calcschist and the serpentinite, as shown by the location of the dissolution curves of these different lithotypes in the correlation diagrams of alkalinity vs. silica (Figure 6(a)) and alkalinity vs. sodium (Figure 6(b)).

A major difference is that Na is expected to have conservative behavior during the dissolution of all the considered rocks, whereas SiO_2 is expected to have conservative behavior during the dissolution of the carbonate rocks but to be fixed by saturation with respect to a silica mineral during the dissolution of the Al-silicate endmember of the calcschist and the serpentinite. Saturation with opal-CT was imposed in the latter two cases, but this condition actually determines the uppermost dissolved SiO_2 concentration, which is 59.0 mg/kg at 12°C. Alternatively, attainment of saturation with respect to less soluble silica minerals, such as chalcedony or α-cristobalite or moganite, is possible, with corresponding SiO_2 concentrations of 11.8, 18.8, and 26.7 mg/kg, respectively, at 12°C.

Consistent with the location of the rock dissolution curves, most Ca-HCO_3 and Ca(Mg)-HCO_3 waters have SiO_2 and Na concentrations lower than SiO_2-rich Ca-HCO_3, SiO_2-rich Ca(Mg)-HCO_3, and Mg-HCO_3 waters. However, a few Ca-HCO_3 waters have Na concentrations higher than expected values possibly due to high contributions of the marine-atmospheric aerosols or limited anthropogenic contamination.

(3) Lithium and Potassium. The correlation diagrams of alkalinity vs. lithium (Figure 7(a)) and alkalinity vs. potassium (Figure 7(b)) show that the highest concentrations of these two alkali metals are expected for dissolution of the Al-silicate endmember of the calcschist whereas lower concentrations are foreseen for dissolution of the carbonate rocks and the serpentinite. However, the spread of the analytical data is not consistent or is not entirely consistent with these theoretical predictions, suggesting that the variability of Li and K concentrations in the rocks of interest might be larger than indicated by the available analytical data. Furthermore, the limited effects of anthropogenic contamination cannot be ruled out for potassium.

(4) Aluminum and Iron. Most groundwaters of the Pollino National Park are found between the curves of rock dissolution accompanied by precipitation of amorphous Al hydroxide and the curves of rock dissolution with concurrent production of crystalline gibbsite, indicating that Al

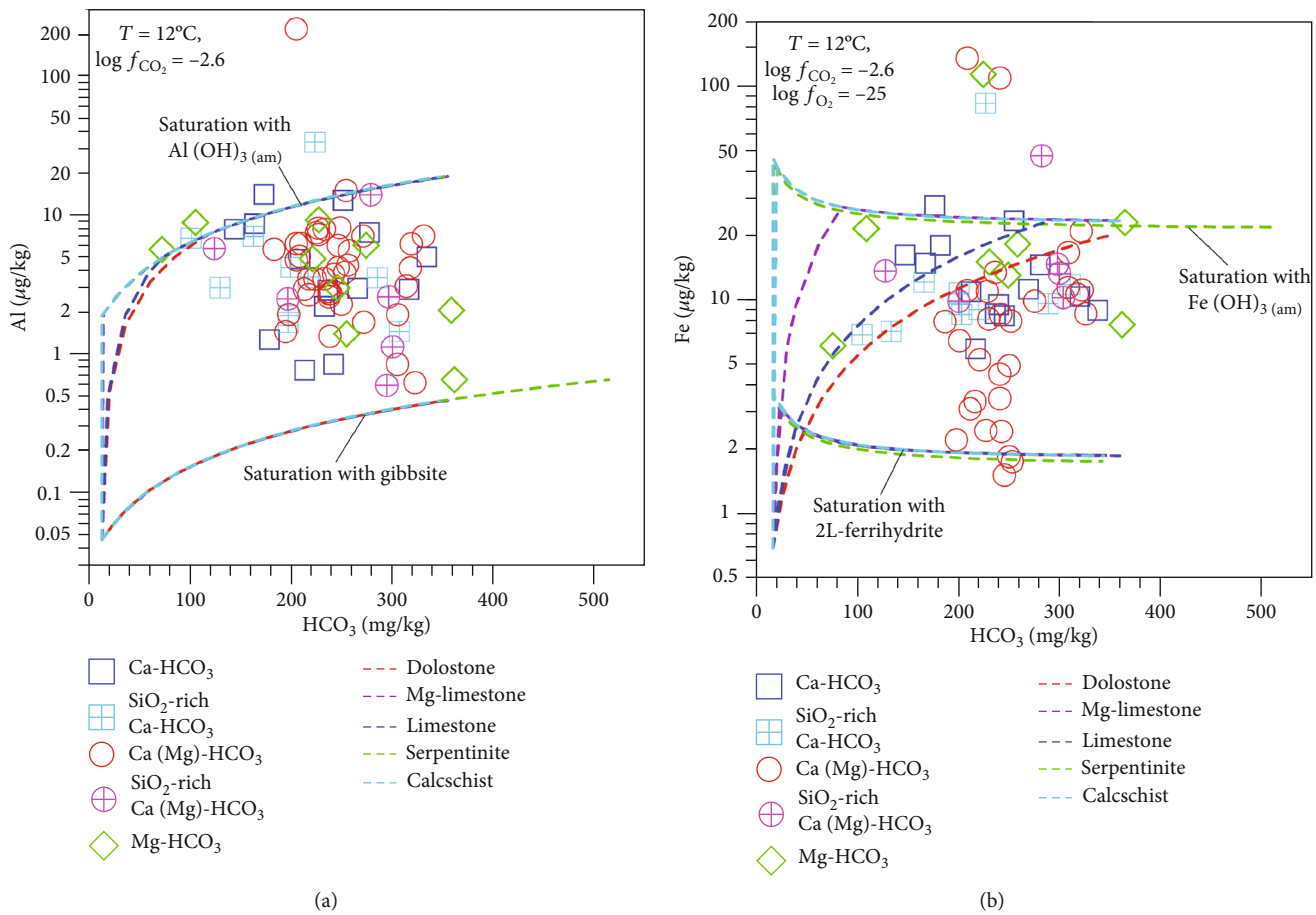

Figure 8: Correlation diagrams of alkalinity (expressed in mg HCO_3/kg) vs. (a) aluminum and (b) iron during the progressive dissolution of different rocks (see legend) according to the simulations elaborated in this work.

concentration is controlled by saturation with amorphous Al hydroxide or crystalline gibbsite or Al oxy-hydroxide of intermediate crystallinity, irrespective of the dissolving lithotype (Figure 8(a)). These Al-controlling solid phases are early-precipitating, persisting solid phases during water-rock interaction. Similarly, most waters of interest are positioned between the curves of rock dissolution accompanied by precipitation of amorphous HFO and the curves of rock dissolution with concurrent generation of crystalline HFO, suggesting that Fe concentration is governed by saturation with amorphous or crystalline HFO or HFO of intermediate crystallinity (Figure 8(b)). The saturation with HFO is attained almost immediately during the dissolution of the Al-silicate and carbonate endmembers of the calcschist and the serpentinite, whereas it is achieved at progressively later stages during the dissolution of the Mg-limestone, the limestone, and the dolomite, respectively.

4.3. Geological and Hydrogeological Evidence. In the Pollino National Park, the main springs are generally localized in the proximity of hydrogeological boundaries that play the role of the flow zone or permeability threshold. This important point that was already mentioned in Section 2 (e.g., Figure 1) can be appreciated in the schematic geological section of Figure 9 showing the stratigraphic relationships among different lithotypes and the water discharge areas of each chemical type.

In detail, Ca-HCO_3 and Ca(Mg)-HCO_3 waters are generally related to main outcrops of the Triassic dolostones and limestones and are often found close to the contact between these rocks and different lithotypes of low permeability. Both fracturing and karsting largely control the development of these carbonate aquifers often discharging through springs of high flow rates, especially near the main hydrogeological contacts. Moreover, the water transfers from limestone to dolostone reservoirs or vice versa can easily occur due to karsting and fracturing. The performed reaction path modeling and the available analytical data show clearly the occurrence of this exchange process among aquifers hosted in different carbonate rocks. In fact, there is no break of continuity in the spread of Ca-HCO_3 and Ca(Mg)-HCO_3 waters in all the previously examined diagrams, due to the interactions of these waters with different carbonate rocks, i.e., limestone, Mg-limestone, and dolostone. These waters are also characterized by small concentrations of SiO_2 (Figure 6(a)) which probably derive from Si-bearing minerals present as impurities in carbonate rocks or from a minor, time-limited interaction with the siliceous-clastic component of the Calabro-Lucano Flysch Unit (clayey-calcareous arenaceous complex) and/or the Frido Unit (peliticschist and calcschist),

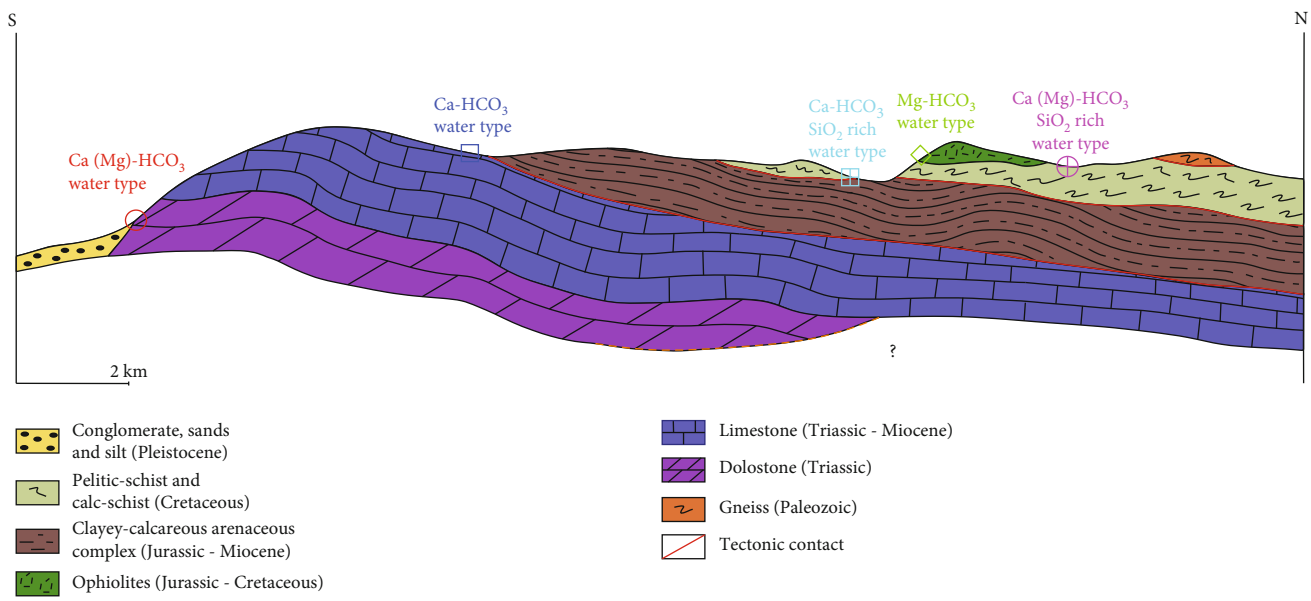

Figure 9: Schematic geological section (the trace is reported in Figure 1) representing the main units cropping out in the study area and the typical emergency area for each chemical type.

both widely present in the Pollino National Park area in a stratigraphically higher position than the carbonate complex (Figure 9). In fact, the SiO_2 concentrations explained by the theoretical dissolution trends of the carbonate rocks are lower than those by the analytical data, suggesting that Si sources external to the carbonate rocks have to be invoked to explain the analytical data.

The SiO_2-rich Ca-HCO_3 and Ca(Mg)-HCO_3 waters are influenced to a considerable extent by the dissolution of chert, quartz, and/or other Si-bearing minerals present in the rocks of the Calabro-Lucano Flysch Unit (clayey-calcareous arenaceous complex) and the Frido Unit (peliticschist and calcschist) (Figure 9), in line with the theoretical dissolution trends of the Al-silicate endmember of the calcschist. Finally, the chemical characteristics of the Mg-HCO_3 waters, generally emerging from serpentinite rocks, are controlled almost exclusively by the dissolution of this lithotype.

5. Conclusions

Reaction path modeling of rock dissolution was performed for the main lithotypes cropping out in the Pollino National Park, including limestone, Mg-limestone, dolomite, serpentinite, Al-silicate fraction of calcschist, and carbonate fraction of calcschist. Geochemical modeling was carried out adopting an innovative approach, that is, allowing the precipitation of a few secondary solid phases only, namely, opal-CT or chalcedony, amorphous or crystalline $Al(OH)_3$, and amorphous or crystalline FeOOH. In this way, it was possible to reproduce the whole range of alkalinities measured in local groundwaters, while this target would not have been achieved by allowing the precipitation of carbonate minerals.

Through the comparison of the theoretical water composition resulting from the dissolution of the considered rocks with the corresponding chemical characteristics of 105 local groundwaters, it was ascertained that major solutes, SiO_2, Li, Al, and Fe, are satisfactorily explained by the dissolution of the considered lithotypes and the detected concentrations do not exceed the threshold values established by WHO. This fact proves the effectiveness of both the reaction path modeling, in general, and, in particular, the approach adopted to deal with secondary solid phases.

The results of reaction path modeling were validated by hydrogeological evidence which highlights the occurrence of multiple interactions between the considered groundwaters and the several lithotypes. Ca-HCO_3 and Ca(Mg)-HCO_3 waters result from the dissolution of carbonate rocks with minor, time-limited interaction with the siliceous-clastic component of the Calabro-Lucano Flysch Unit and/or the Frido Unit, which are both widely present in the Pollino National Park area in a stratigraphically higher position than the carbonate complex. The dissolution of these lithotypes exerts strong control over the chemical characteristics of the SiO_2-rich Ca-HCO_3 and SiO_2-rich Ca(Mg)-HCO_3 waters, whereas the chemistry of Mg-HCO_3 waters is controlled almost exclusively by the dissolution of serpentinite rocks.

Data Availability

The manuscript is a data self-contained article, whose results were obtained from the laboratory analysis, and the entire data is presented within the article. However, if any additional information is required, these are available from the corresponding author upon request to the e-mail ilaria.fuoco@unical.it.

Conflicts of Interest

The authors declare that they have no known competing financial interests or personal relationships that could have appeared to influence the work reported in this paper.

Acknowledgments

The work has been supported by the collaboration agreement relating to the project "Acque minerali e rocce: Ogni acqua, la sua roccia." CODICE CUP D18D19005690001 was funded by UNESCO GeoparkOffice Pollino National Park Authority.

Supplementary Materials

Physical-chemical parameters of studied groundwaters. *(Supplementary Materials)*

References

[1] C. Apollaro, F. Perri, E. Le Pera, I. Fuoco, and T. Critelli, "Chemical and minero-petrographical changes on granulite rocks affected by weathering processes," *Frontiers of Earth Science*, vol. 13, no. 2, pp. 247–261, 2019.

[2] C. Apollaro, F. Perri, L. Borrelli, and T. Caloiero, "The role of water-rock interaction processes in soil formation: geochemical, mineralogical, geomorphological, and engineering-geological aspects," *Geofluids*, vol. 2019, Article ID 8453136, 4 pages, 2019.

[3] F. Perri, F. Ietto, E. Le Pera, and C. Apollaro, "Weathering processes affecting granitoid profiles of Capo Vaticano (Calabria, southern Italy) based on petrographic, mineralogic and reaction path modelling approaches," *Geological Journal*, vol. 51, no. 3, pp. 368–386, 2016.

[4] F. Perri, F. Scarciglia, C. Apollaro, and L. Marini, "Characterization of granitoid profiles in the Sila Massif (Calabria, southern Italy) and reconstruction of weathering processes by mineralogy, chemistry, and reaction path modeling," *Journal of Soils and Sediments*, vol. 15, no. 6, pp. 1351–1372, 2015.

[5] L. Elango and R. Kannan, "Chapter 11. Rock–water interaction and its control on chemical composition of groundwater," *Concepts and Applications in Environmental Geochemistry*, vol. 5, pp. 229–243, 2007.

[6] H. C. Helgeson, "Evaluation of irreversible reactions in geochemical processes involving minerals and aqueous solutions—I. Thermodynamic relations," *Geochimica et Cosmochimica Acta*, vol. 32, no. 8, pp. 853–877, 1968.

[7] H. C. Helgeson, T. H. Brown, A. Nigrini, and T. A. Jones, "Calculation of mass transfer in geochemical processes involving aqueous solutions," *Geochimica et Cosmochimica Acta*, vol. 34, no. 5, pp. 569–592, 1970.

[8] T. W. Wolery and R. L. Jarek, *Software User's Manual. EQ3/6, Version 8.0*, Sandia National Laboratories – U.S. Dept. of Energy Report, 2003.

[9] M. H. Reed, "Calculation of multicomponent chemical equilibria and reaction processes in systems involving minerals, gases and an aqueous phase," *Geochimica et Cosmochimica Acta*, vol. 46, no. 4, pp. 513–528, 1982.

[10] D. L. Parkhurst and C. A. J. Appelo, "Description of input and examples for PHREEQC version 3- a computer program for speciation, batch-reaction, one-dimensional transport, and inverse geochemical calculations," *U.S. Geological Survey Techniques and Methods, Book 6, Chap. A43*, p. 497, 2013, available only at http://pubs. https://pubs.usgs.gov/tm/06/a43//.

[11] C. Apollaro, "Geochemical modeling of water-rock interaction in the granulite rocks of lower crust in the Serre Massif (Southern Calabria, Italy)," *Geofluids*, vol. 2019, Article ID 5602648, 11 pages, 2019.

[12] C. Apollaro, I. Fuoco, G. Brozzo, and R. De Rosa, "Release and fate of Cr (VI) in the ophiolitic aquifers of Italy: the role of Fe (III) as a potential oxidant of Cr (III) supported by reaction path modelling," *Sci. Total Environ.*, vol. 660, pp. 1459–1471, 2019.

[13] C. Apollaro, L. Marini, T. Critelli et al., "Modeling of the impact of dolomite and biotite dissolution on vermiculite composition in a gneissic shallow aquifer of the Sila Massif (Calabria, Italy)," *Applied Geochemistry*, vol. 35, pp. 297–311, 2013.

[14] C. Apollaro, L. Marini, T. Critelli, and R. De Rosa, "The standard thermodynamic properties of vermiculites and prediction of their occurrence during water-rock interaction," *Applied Geochemistry*, vol. 35, pp. 264–278, 2013.

[15] C. Apollaro, L. Marini, T. Critelli et al., "Investigation of rock-to-water release and fate of major, minor, and trace elements in the metabasalt-serpentinite shallow aquifer of Mt. Reventino (CZ, Italy) by reaction path modelling," *Applied Geochemistry*, vol. 26, no. 9-10, pp. 1722–1740, 2011.

[16] C. Apollaro, M. Accornero, L. Marini, D. Barca, and R. De Rosa, "The impact of dolomite and plagioclase weathering on the chemistry of shallow groundwaters circulating in a granodiorite-dominated catchment of the Sila Massif (Calabria, Southern Italy)," *Applied Geochemistry*, vol. 24, no. 5, pp. 957–979, 2009.

[17] C. Apollaro, L. Marini, and R. De Rosa, "Use of reaction path modeling to predict the chemistry of stream water and groundwater: a case study from the Fiume Grande Valley (Calabria, Italy)," *Environmental Geology*, vol. 51, no. 7, pp. 1133–1145, 2007.

[18] C. Apollaro, L. Marini, R. De Rosa, P. Settembrino, F. Scarciglia, and G. Vecchio, "Geochemical features of rocks, stream sediments, and soils of the Fiume Grande Valley (Calabria, Italy)," *Environmental Geology*, vol. 52, no. 4, pp. 719–729, 2007.

[19] S. A. Banwart, A. Berg, and D. J. Beerling, "Process-based modeling of silicate mineral weathering responses to increasing atmospheric CO2 and climate change," *Global Biogeochemical Cycles*, vol. 23, no. 4, 2009.

[20] T. Boschetti and L. Toscani, "Springs and streams of the Taro–Ceno Valleys (Northern Apennine, Italy): reaction path modeling of waters interacting with serpentinized ultramafic rocks," *Chemical Geology*, vol. 257, no. 1-2, pp. 76–91, 2008.

[21] B. Y. Choi, S. T. Yun, K. H. Kim, H. S. Choi, G. T. Chae, and P. K. Lee, "Geochemical modeling of CO2–water–rock interactions for two different hydrochemical types of CO2-rich springs in Kangwon District, Korea," *Journal of Geochemical Exploration*, vol. 144, pp. 49–62, 2014.

[22] T. Critelli, G. Vespasiano, C. Apollaro, F. Muto, L. Marini, and R. De Rosa, "Hydrogeochemical study of an ophiolitic aquifer: a case study of Lago (Southern Italy, Calabria)," *Environmental Earth Sciences.*, vol. 74, no. 1, pp. 533–543, 2015.

[23] T. Critelli, L. Marini, J. Schott et al., "Dissolution rates of actinolite and chlorite from a whole-rock experimental study of metabasalt dissolution from 2≤ pH≤12 at 25 C," *Chemical Geology*, vol. 390, pp. 100–108, 2014.

[24] H. Hellevang, V. T. H. Pham, and P. Aagaard, "Kinetic modelling of CO_2-water-rock interactions," *International Journal of Greenhouse Gas Control*, vol. 15, pp. 3–15, 2013.

[25] K. L. Lecomte, A. I. Pasquini, and P. J. Depetris, "Mineral weathering in a semiarid mountain river: its assessment through PHREEQC inverse modeling," *Aquatic Geochemistry*, vol. 11, no. 2, pp. 173–194, 2005.

[26] D. Miriello, A. Bloise, G. M. Crisci, E. Barrese, and C. Apollaro, "Effects of milling: a possible factor influencing the durability of historical mortars," *Archaeometry*, vol. 52, no. 4, pp. 668–679, 2010.

[27] M. U. Sharif, R. K. Davis, K. F. Steele, B. Kim, T. M. Kresse, and J. A. Fazio, "Inverse geochemical modeling of groundwater evolution with emphasis on arsenic in the Mississippi River Valley alluvial aquifer, Arkansas (USA)," *Journal of Hydrology*, vol. 350, no. 1-2, pp. 41–55, 2008.

[28] G. Vespasiano, P. Notaro, and G. Cianflone, "Water-mortar interaction in a tunnel located in Southern Calabria (southern Italy)," *Environmental and Engineering Geoscience*, vol. 24, no. 3, pp. 305–315, 2018.

[29] C. Zhu, "Geochemical modeling of reaction paths and geochemical reaction networks," *Reviews in Mineralogy and Geochemistry*, vol. 70, no. 1, pp. 533–569, 2009.

[30] S. Mazzoli and M. Helman, "Neogene patterns of relative plate motion for Africa-Europe: some implications for recent central Mediterranean tectonics," in *Active Continental Margins — Present and Past*, pp. 464–468, Springer, Berlin, Heidelberg, 1994.

[31] C. Monaco, L. Tortorici, and W. Paltrinieri, "Structural evolution of the Lucanian Apennines, southern Italy," *Journal of Structural Geology*, vol. 20, no. 5, pp. 617–638, 1998.

[32] R. W. H. Butler, S. Corrado, S. Mazzoli et al., "Time and space variability of «thin-skinned» and «thick-skinned» thrust tectonics in the Apennines (Italy)," *Rendiconti Lincei*, vol. 11, no. 1, pp. 5–39, 2000.

[33] S. Critelli, F. Muto, V. Tripodi, and F. Perri, "Relationships between lithospheric flexure, thrust tectonics and stratigraphic sequences in foreland setting: the southern Apennines foreland basin system, Italy," in *New Frontiers in Tectonic Research - At the Midst of Plate ConvergenceNew Frontiers in Tectonic Research - At the Midst of Plate Convergence*, U. Schattner, Ed., pp. 121–170, InTech Open Access Publisher, 2011.

[34] S. Critelli, F. Muto, V. Tripodi, and F. Perri, "Link between thrust tectonics and sedimentation processes of stratigraphic sequences from the southern Apennines foreland basin system, Italy," *Rendiconti Online della Società Geologica Italiana*, vol. 25, pp. 21–42, 2013.

[35] J. P. Van Dijk, M. Bello, G. P. Brancaleoni et al., "A regional structural model for the northern sector of the Calabrian Arc (Southern Italy)," *Tectonophysics*, vol. 324, no. 4, pp. 267–320, 2000.

[36] F. Corbi, G. Fubelli, F. Lucà et al., "Vertical movements in the Ionian margin of the Sila Massif (Calabria, Italy)," *Bollettino della Societa Geologica Italiana*, vol. 128, no. 3, pp. 731–738, 2009.

[37] E. Turco, R. Maresca, and P. Cappadona, "La tettonica plio-pleistocenica del confine calabro-lucano: modello cinematico," *Memorie della Societa Geologica Italiana*, vol. 45, pp. 519–529, 1990.

[38] S. Catalano, C. Monaco, L. Tortorici, and C. Tansi, "Pleistocene strike-slip tectonics in the Lucanian Apennine (southern Italy)," *Tectonics*, vol. 12, no. 3, pp. 656–665, 1993.

[39] M. Schiattarella, "Quaternary tectonics of the Pollino Ridge, Calabria-Lucania boundary, southern Italy," in *Geological Society*, vol. 135, pp. 341–354, Special Publications, London, 1998.

[40] C. Tansi, F. Muto, S. Critelli, and G. Iovine, "Neogene-Quaternary strike-slip tectonics in the central Calabrian Arc (southern Italy)," *Journal of Geodynamics*, vol. 43, no. 3, pp. 393–414, 2007.

[41] A. IANNACE, S. VITALE, M. D'ERRICO et al., "The carbonate tectonic units of northern Calabria (Italy): a record of Apulian palaeomargin evolution and Miocene convergence, continental crust subduction, and exhumation of HP–LT rocks," *Journal of the Geological Society*, vol. 164, no. 6, pp. 1165–1186, 2007.

[42] R. Selli, "Sulla trasgressione del Miocene nell'Italia meridionale," *Museo Geologico" Giovanni Capellini"*, vol. 24, pp. 1–54, 1957.

[43] E. Patacca, R. Sartori, and P. Scandone, "Tyrrhenian basin and Apennines. Kinematic evolution and related dynamic constraints," in *Recent Evolution and Seismicity of the Mediterranean Region*, E. Boschi, Ed., pp. 161–171, Springer, Dordrecht, 1993.

[44] G. Bonardi, F. O. Amore, G. Ciampo, P. de Capoa, P. Miconnet, and V. Perrone, "Il complesso Liguride Auct.: Stato delle conoscenze e problemi aperti dulla sur evoluzione pre-Appenninica ed i suoli rapporti con l'Arco Calabro," *Memorie della Società Geologica Italiana*, vol. 41, pp. 17–35, 1988.

[45] E. Patacca and P. Scandone, "Geology of the southern Apennines," *Bollettino della Società Geologica Italiana*, vol. 7, pp. 75–119, 2007.

[46] F. Matano, S. Critelli, M. Barone, F. Muto, and S. Di Nocera, "Stratigraphic and provenance evolution of the Southern Apennines foreland basin system during the Middle Miocene to Pliocene (Irpinia-Sannio successions, Italy)," *Marine and Petroleum Geology*, vol. 57, pp. 652–670, 2014.

[47] C. Monaco, "Pleistocene strike-slip tectonics in the Pollino mountain range (Southern Italy)," *Ann. Tecton. 8/2, 100–112*, 1993.

[48] G. Cello and S. Mazzoli, "Apennine tectonics in southern Italy: a review," *Journal of Geodynamics*, vol. 27, no. 2, pp. 191–211, 1998.

[49] F. Muto, V. Spina, V. Tripodi, S. Critelli, and C. Roda, "Neogene tectonostratigraphic evolution of allochthonous terranes in the eastern Calabrian foreland (southern Italy)," *Italian Journal of Geosciences*, vol. 133, no. 3, pp. 455–473, 2014.

[50] S. Critelli, F. Muto, F. Perri, and V. Tripodi, "Interpreting provenance relations from sandstone detrital modes, southern Italy foreland region: stratigraphic record of the Miocene tectonic evolution," *Marine and Petroleum Geology*, vol. 87, pp. 47–59, 2017.

[51] C. Monaco and L. Tortorici, "Tectonic role of ophiolite-bearing terranes in the development of the Southern Apennines orogenic belt," *Terra Nova*, vol. 7, no. 2, pp. 153–160, 1995.

[52] V. Allocca, F. Celico, P. Celico et al., "Note illustrative della Carta idrogeologica dell'Italia meridionale," in *Istituto Poligrafico e Zecca dello Stato, ISBN 88-448-0215-5*, P. Celico, P. Vita, G. Monacelli, and G. Tranfaglia, Eds., p. 211, con carte allegate, 2007.

[53] C. Apollaro, A. Buccianti, G. Vespasiano et al., "Comparative geochemical study between the tap waters and the bottled mineral waters in Calabria (Southern Italy) by compositional data

analysis (CoDA) developments," *Applied Geochemistry*, vol. 107, pp. 19–33, 2019.

[54] C. Apollaro, G. Vespasiano, F. Muto, R. De Rosa, D. Barca, and L. Marini, "Use of mean residence time of water, flowrate, and equilibrium temperature indicated by water geothermometers to rank geothermal resources. Application to the thermal water circuits of Northern Calabria," *Journal of Volcanology and Geothermal Research*, vol. 328, pp. 147–158, 2016.

[55] G. Vespasiano, C. Apollaro, F. Muto, E. Dotsika, R. De Rosa, and L. Marini, "Chemical and isotopic characteristics of the warm and cold waters of the Luigiane Spa near Guardia Piemontese (Calabria, Italy) in a complex faulted geological framework," *Applied Geochemistry*, vol. 41, pp. 73–88, 2014.

[56] G. Vespasiano, C. Apollaro, F. Muto, R. De Rosa, E. Dotsika, and L. Marini, "Preliminary geochemical characterization of the thermal waters of the Grotta delle Ninfe near Cerchiara di Calabria (South Italy)," *Rendiconti online della Società Geologica Italiana*, vol. 39, pp. 130–133, 2016.

[57] G. Vespasiano, C. Apollaro, R. De Rosa et al., "The Small Spring Method (SSM) for the definition of stable isotope - elevation relationships in Northern Calabria (Southern Italy)," *Applied Geochemistry*, vol. 63, pp. 333–346, 2015.

[58] G. Vespasiano, L. Marini, C. Apollaro, and R. De Rosa, "Preliminary geochemical characterization of the thermal waters of Caronte SPA springs (Calabria, South Italy)," *Rendiconti online della Società Geologica Italiana*, vol. 39, pp. 138–141, 2016.

[59] V. Cotecchia, G. Nuzzo, A. Salvemini, and N. A. Ventrella, "Studi di geologia applicata ed idrogeologia finalizzati alla realizzazione della galleria di valico del Monte la Mula per l'Acquedotto dell'Abatemarco-Mezzafiumina," *Geol. Appl. e Idrogeol*, vol. 18, no. 1, pp. 451–489, 1983.

[60] D. Grassi, S. Grimaldi, F. Sdao, and G. Spilotro, "Idrogeologia dell'acquifero carbonatico di Madonna del Pollino (Basilicata)," *Mem. Soc. Geol. It.*, vol. 51, pp. 975–988, 1996.

[61] C. Apollaro, V. Tripodi, G. Vespasiano et al., "Chemical, isotopic and geotectonic relations of the warm and cold waters of the Galatro and Antonimina thermal areas, southern Calabria, Italy," *Marine and Petroleum Geology*, vol. 109, pp. 469–483, 2019.

[62] C. Apollaro, A. Caracausi, M. Paternoster et al., "Fluid geochemistry in a low-enthalpy geothermal field along a sector of southern Apennines chain (Italy)," *Journal of Geochemical Exploration*, vol. 219, p. 106618, 2020.

[63] I. Fuoco, A. Figoli, A. Criscuoli et al., "Geochemical modeling of chromium release in natural waters and treatment by RO/NF membrane processes," *Chemosphere*, vol. 254, p. 126696, 2020.

[64] A. Figoli, I. Fuoco, C. Apollaro et al., "Arsenic-contaminated groundwaters remediation by nanofiltration," *Separation and Purification Technology*, vol. 238, p. 116461, 2020.

[65] M. Vardè, A. Servidio, G. Vespasiano et al., "Ultra-trace determination of total mercury in Italian bottled waters," *Chemosphere*, vol. 219, pp. 896–913, 2019.

[66] G. Vespasiano, G. Cianflone, A. Romanazzi et al., "A multidisciplinary approach for sustainable management of a complex coastal plain: the case of Sibari Plain (Southern Italy)," *Marine and Petroleum Geology*, vol. 109, pp. 740–759, 2019.

[67] S. Margiotta, G. Mongelli, V. Summa, M. Paternoster, and S. Fiore, "Trace element distribution and Cr (VI) speciation in Ca-HCO3 and Mg-HCO3 spring waters from the northern sector of the Pollino Massif, southern Italy," *Journal of Geochemical Exploration*, vol. 115, pp. 1–12, 2012.

[68] T. W. Wolery and C. Jove-Colon, "Qualification of thermodynamic data for geochemical modeling of mineral-water interactions in dilute systems," *Sandia National Laboratories Report ANL-WIS-GS-000003 REV 01*, Yucca Mountain Project, Las Vegas, Nevada, 2007.

[69] T. J. Wolery and S. A. Daveler, "EQ 6, a computer program for reaction path modeling of aqueous geochemical systems: theoretical manual, user's guide, and related documentation (version 7.0)," *Report UCRL-MA-110662 PT IV*, Lawrence Livermore National Laboratory, United States, 1992.

[70] M. C. Dichicco, S. Laurita, M. Paternoster, G. Rizzo, R. Sinisi, and G. Mongelli, "Serpentinite carbonation for CO2 sequestration in the southern Apennines: preliminary study," *Energy Procedia*, vol. 76, pp. 477–486, 2015.

[71] G. Rizzo, M. T. Cristi Sansone, F. Perri, and S. Laurita, "Mineralogy and petrology of the metasedimentary rocks from the Frido Unit (southern Apennines, Italy)," *Periodico di Mineralogia*, vol. 85, no. 2, 2016.

[72] J. Dousma and P. L. de Bruyn, "Hydrolysis-precipitation studies of iron solutions. I. Model for hydrolysis and precipitation from Fe (III) nitrate solutions," *Journal of Colloid and Interface Science*, vol. 56, no. 3, pp. 527–539, 1976.

[73] D. K. Nordstrom, L. N. Plummer, T. M. L. Wigley et al., "A comparison of computerized chemical models for equilibrium calculations in aqueous systems," in *ACS Symposium Series*, E. A. Jenne, Ed., pp. 857–892, 1979.

[74] C. A. J. Appelo and D. Postma, *Geochemistry, Groundwater and Pollution*, A.A. Balkema, Rotterdam, 1996.

[75] R. O. Fournier, "Silica in thermal waters: laboratory and field investigations," *Proc. Int. l Symp. Hydrogeochemistry and Biogeochemistry*, 1973pp. 122–139, Tokyo, 1973.

[76] D. K. Nordstrom, "Aqueous redox chemistry and the behavior of iron in acid mine waters," *Proceedings of the Workshop on Monitoring Oxidation-Reduction Processes for Ground-water Restoration*, 2002, pp. 43–47, Environmental Protection Agency. EPA/600/R-02/002, Dallas, Texas, April 25-27, 2000 Cincinnati, OH, 2002.

[77] G. A. Brook, M. E. Folkoff, and E. O. Box, "A world model of soil carbon dioxide," *Earth Surface Processes and Landforms*, vol. 8, no. 1, pp. 79–88, 1983.

[78] W. Pohl, "Comparative geology of magnesite deposits and occurrences," *Monogr. Ser. Mineral deposits*, vol. 28, pp. 1–13, 1989.

[79] W. Pohl, "Genesis of magnesite deposits—models and trends," *Geologische Rundschau*, vol. 79, no. 2, pp. 291–299, 1990.

[80] R. M. Garrels, "Genesis of some ground waters from igneous rocks," in *Researches in Geochemistry*, P. H. Abelson, Ed., vol. 2, pp. 406–420, Wiley, 1968.

[81] F. B. Tonani, K. Nagao, J. Moore, G. Natale, and T. Sperry, "Water and gas geochemistry of the Cove-Fort Sulphurdale geothermal system," *Proceedings, Twenty-Third Workshop on Geothermal Reservoir Engineering*, 1998Stanford University, Stanford, California, 1998.

[82] World Health Organization, *Guidelines for Drinking-Water Quality: First Addendum to the Fourth Edition*, 2017, https://www.who.int/publications/i/item/9789241549950.

Hindawi
Geofluids
Volume 2021, Article ID 6654477, 11 pages
https://doi.org/10.1155/2021/6654477

Research Article

Performance Evaluation of Polyethersulfone Membranes for Competitive Removal of Cd^{2+}, Co^{2+}, and Pb^{2+} Ions from Simulated Groundwater

Salwa H. Ahmed,[1] Sama M. Al-Jubouri,[2] Nasser Zouli,[3] Ahmed A. Mohammed,[4] Hasan Shaker Majdi,[5] Issam K. Salih,[5] Muayad Al-shaeli,[6] Ayham. M. I. Al-Rahawi,[7] Qusay F. Alsalhy,[8] and Alberto Figoli[9]

[1]*Environment Engineering Department, College of Engineering, University of Tikrit, Iraq*
[2]*Department of Chemical Engineering, College of Engineering, University of Baghdad, 10071 Baghdad, Iraq*
[3]*Department of Chemical Engineering, Jazan University, P.O. Box 706, Jazan 45142, Saudi Arabia*
[4]*Environment Engineering Department, College of Engineering, University of Baghdad, 10071, Iraq*
[5]*Al-Mustaqbal University College, Babylon, Iraq*
[6]*Monash University, Department of Chemical Engineering, Clayton, VIC 3800, Australia*
[7]*Department of Engineering, GUtech, P.O. Box: 1816, PC 130, Oman*
[8]*Membrane Technology Research Unit, Department of Chemical Engineering, University of Technology, 10066 Baghdad, Iraq*
[9]*Institute on Membrane Technology, National Research Council (ITM-CNR), 87030 Rende (CS), Italy*

Correspondence should be addressed to Qusay F. Alsalhy; qusay_alsalhy@yahoo.com

Received 14 October 2020; Revised 14 December 2020; Accepted 18 December 2020; Published 4 January 2021

Academic Editor: Andrew H. Manning

This paper presents studying the performance of three types of polyethersulfone (PES) membrane for the simultaneous removal of Co^{2+} ions, Cd^{2+} ions, and Pb^{2+} ions from binary and ternary aqueous solutions. Co^{2+} ions, Cd^{2+} ions, and Pb^{2+} ions with two different initial concentrations (e.g., 10 and 50 ppm) were selected as examples of heavy metals that contaminate the groundwater as a result of geological and human activities. This study investigated the effect of types of PES membrane and metal ions concentration on the separation process. For the binary aqueous solutions, the permeation flux of the PES2 membranes was higher for the separation process of solutions containing 50 ppm of Cd^{2+} ions and 10 ppm of Co^{2+} ions (24.7 $L/m^2 \cdot h$) and Pb^{2+} ions (23.7 $L/m^2 \cdot h$). All the metals in the binary solutions had high rejection when their initial concentration was lower than the initial concentration of the other metal present in the same solution. Using PES2, the maximum rejection of Cd^{2+} ions was 61.3% when the initial concentrations were 50 ppm Pb^{2+} ions: 10 ppm Cd^{2+} ions and 55.4% for Pb^{2+} ions when the initial concentrations were 10 ppm Pb^{2+} ions: 50 ppm Cd^{2+} ions. For the ternary aqueous solutions, the rejection and the permeation flux of the PES membranes increased with decreasing the heavy metal initial concentration. Using PES2, the maximum permeation flux was 21.6 $L/m^2 \cdot h$ when the initial concentration of the metals was 10 ppm; and the maximum rejection of the metals obtained at initial concentration of 10 ppm was 50.5% for Co^{2+} ions, 48.3% for Cd^{2+} ions, and 40% for Pb^{2+} ions. The results of the filtration process using PES2 of simulated contaminated-groundwater indicated the efficient treatment of groundwater containing Co^{2+}, Cd^{2+}, and Pb^{2+} ions.

1. Introduction

Nowadays, contamination of groundwater is one of the most important environmental issues because it contains wide range of contaminants that influence water resources such as heavy metals [1]. The sources of groundwater pollution by heavy metals are mainly geological actions and human activities represented by industries and domestic activities

[2]. A potential source of groundwater pollution by heavy metals is contaminant seepage from the disposal sites as well as they are normally present in high concentrations in the landfill leachate [3]. Heavy metals such as cadmium, copper, lead, nickel, and zinc are naturally occurring elements and are actually necessary for human health when they are present in small amounts in our environment [4] However, various industrial activities release different concentrations of heavy metals in water such as textile industries, battery manufacturing, electroplating, automotive industries, mining, and metal finishing [5]. Discharges of different industrial activities are the main reasons of water pollution because they consist of different poisonous heavy metal ions that accumulate in microorganisms and aquatic fauna and flora which may enter inside the human body through a food chain causing health problems [6].

Also, the discharges of the nuclear fuel cycle and the production and applications of radioisotopes are the main reason behind pollution by radioactive waste. Besides, the other sources of radioactive waste are the byproducts resultant of exploitation of natural resources and raw materials containing radioactive isotopes that are used for the production of agricultural and medical products [7]. The waste stream of these activities may contain radionuclides of individual elements such as cesium, molybdenum, strontium, iodine, tritium, cobalt, actinides, and lanthanides [8]. The contaminated soil and water by radioactive wastes have harmful effects on the living organisms, natural resources, and the environment; thus, they are hazardous to the health and safety of the human and other creatures [7].

Because the removal of heavy metals and radioactive wastes that exist in the form of cations has become an urgent issue, different treatment technologies have been used and improved so far to achieve an effective reduction of the concentrations of the toxic pollutant such as chemical precipitation, evaporation, extraction, membrane filtration, adsorption, coagulation, flocculation, sedimentation, thermal treatment, and ion exchange [9–12]. The above techniques show some drawbacks such as the cost of flotation and chemical precipitation resulting from generating extra sludge; poor selectivity and high sensitivity to pH for the ion-exchange process, nonselective, and generating intractable sludge for adsorption process. However, both ion exchange and adsorption are relatively low-cost, easily handled, and effective for low metal concentrations [13–15].

Membrane filtration technologies including microfiltration (MF), nanofiltration (NF), membrane distillation (MD), and reverse osmosis (RO) are successfully able to offer a significant solution in the field of the environment such as reducing of pollutions, reusing of water, and recycling of the valuable elements from waste effluents [16–19]. Different membrane technologies were applied for the membrane bioreactor (MBR) technique to treat the oil refinery wastewater [20–22], ultrafiltration membrane for dye removal from leather tanning factory [23, 24], ultrafiltration membrane for treating refinery wastewater [25], ultrafiltration membrane for protein and dye removal [26], and ultrafiltration and nanofiltration membranes for produced water treatment [27]. Also, membrane technologies have been considered as promising technologies for removing heavy metals and radioactive wastes because they are highly efficient (high rejection to contaminants), easy to operation, saving space, reliable, and comparatively low energy consumption [14, 28].

Nanofiltration (NF) is theoretically more efficient than ultrafiltration (UF) and gives higher permeate than reverse osmosis (RO); therefore, it has attracted much attention in the applications including food, pharmaceutical, petrochemical industries, and wastewater treatment [15]. Separation of metal ions by NF occurs via size exclusion (sieving effect) and Donnan exclusion (electrostatic repulsion) [29]. The structural features of NF membranes create this combination of effects [30]. In the size exclusion, the species are strictly retained if they have larger hydrated size than the membrane pore size; however, the membrane pores were an obstacle to the species with a similar size. In the Donnan (charge) exclusion, the ions with the same charge (coions) are repelled by a membrane with fixed charged groups while the ions with an opposite charge (counterions) are attracted [31]. NF demands lower pressure and thus lower energy than RO, and it allows high permeate rate with selectively high rejection of divalent ions but low rejection monovalent ions which make NF recommended for treating various industrial effluents and drinking water [30, 32].

Due to the intrinsically rigid nature of lead, cadmium, and cobalt ions when they are discharged into the environment, and their major toxicity with the noxious effect on organic systems, the present work is mainly focused on using the filtration process to treat a simulated groundwater. In the current work, three types of PES membranes were prepared and examined for the removal of lead, cadmium, and cobalt ions from binary and ternary aqueous solutions at various conditions including initial metal ion concentrations and ratio of metals.

2. Chemicals and Experimental Work

Polyether sulfone (PES type Radel, provided by Solvay Advanced Polymers, Belgium) was used to prepare three different PES membranes, which were symbolized by PES1, PES2, and PES3, by the dry/wet phase inversion method. The spinning parameters were air gap distance of 5 cm, extrusion pressure of 1.5 bar, and bore fluid flow rate of 2.5 mL/min. This process required internal and external coagulants; thus, pure water was used for this purpose, and more details regarding the spinning process of hollow fibers were presented elsewhere [33, 34]. PES1, PES2, and PES3 hollow fibers were examined in treating stimulated groundwater containing combination of Cd^{2+} and Co^{2+} and Pb^{2+} ions using crossflow pattern filtration module as shown in Figure 1. The membrane pore size and pore size distribution were measured using Atomic force microscopy (AFM) (SPM AA300; Angstrom Advanced Inc., Stoughton, MA, USA). Each hollow fiber was exposed to a wide surface analysis with an appropriate silicon tip. Also, the dimensions of the PES hollow fibers were measured via scanning electron microscopy (SEM) (TESCAN VEGA3 LM (Oxford Instruments), X-Man, Czech Republic). A statistical test of the pore size

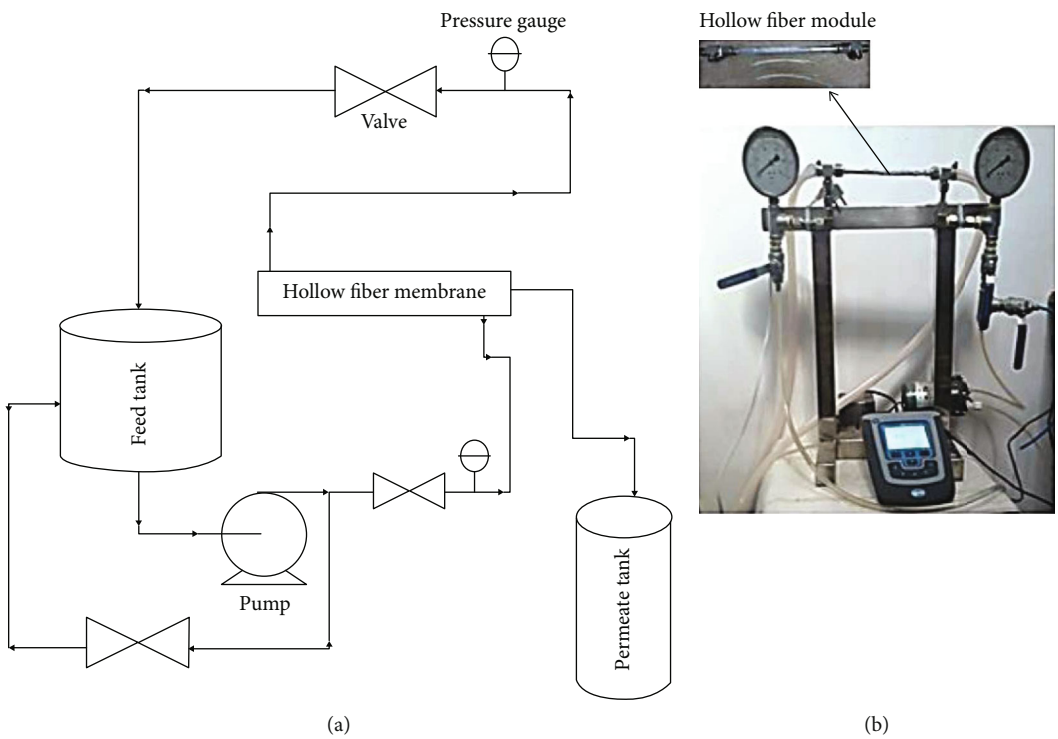

Figure 1: (a) A schematic diagram of the membrane filtration setup. (b) Photo of the membrane filtration setup and hollow fibers.

Table 1: The characteristics of the polyethersulfone (PES) membrane texture.

Membrane symbol	PES content (%)	Average pore size (nm)	Pore size distribution (nm)	Porosity (%)	Outside diameter (μm)	Inside diameter (μm)	Membrane thickness (μm)
PES1	29	52.04	25–100	52.5 ± 1.4	1012	620	196 ± 0.8
PES2	27	58.11	35–130	67.6 ± 0.9	958.4	576	191.2 ± 1.7
PES3	27	47.75	20–115	58.1 ± 1.1	1005	603.6	200.7 ± 2.1

was made for all PES hollow fiber surface via IMAGER 4.3.1 software [33].

The porosity (void fraction) of the hollow fiber ε (%) was estimated by measuring the density of the hollow fiber (e.g., weight of the sample divided by its volume). Then, the porosity of the hollow fibers was calculated by Equation (1) as follows:

$$\varepsilon = 1 - \frac{\rho_m}{\rho_p}, \tag{1}$$

where ρ_P is the density of the PES (g cm^{-3}) which was 1.370 (g cm^{-3}), and ρ_m is the hollow fiber density (g cm^{-3}).

The characteristic of the surface morphology and the other specifications of the prepared PES membranes are displayed in Table 1. The simulated wastewater was prepared from dissolving nitrate salts of Cd^{2+} ions ($Cd(NO_3)_2.6H_2O$), Co^{2+} ions ($Co(NO_3)_2.6H_2O$), and Pb^{2+} ions ($Pb(NO_3)_2.6H_2O$) ions in distilled water and stored in a polyethylene container at room temperature. The concentrations of metal ions in the solutions were prepared in the range of 10-250 ppm. The pH value of the stimulated wastewater was adjusted using 1 M HCl and 1 M NaOH to be in the range of 5.5-6.5 [5], and the temperature of the solutions were maintained 25°C ± 3°C. The PES process was chosen to run at 1 bar during the removal process due to the low concentration of the metal ions.

Each hollow fiber was pressurized for 60 minutes at 3 bar to compact the fibers before measuring the permeation flux in a crossflow filtration mode. Equation (1) was used to calculate the permeate flux (J_V, L/m^2 h).

$$J_v = \frac{V}{t.A}, \tag{2}$$

where V (L) is the volume of permeate, t (h) is time to collect permeate, and A (m^2) is the surface area of the membrane. Each hollow fiber module has 7 hollow fibers with an effective area of 4.9×10^{-3}, 5.5×10^{-3}, and 5.8×10^{-3} m^2, for PES1, PES2, and PES3, respectively. The feed flow rate was set on 0.6 (l/min) with a feed temperature of 25 ± 3°C. Moreover, Equation (2) was used to calculate the rejection percentage (R%) of metal ions.

$$R\% = \frac{C_b - C_p}{C_b} \times 100, \tag{3}$$

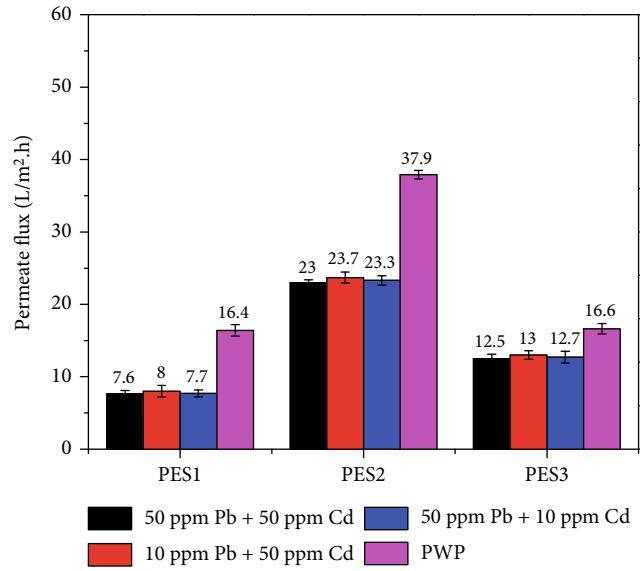

Figure 2: Effect of initial feed concentration of binary aqueous solutions containing Pb^{2+} ions and Cd^{2+} ions on permeate flux for three types of PES hollow fiber membrane (pH 6 ± 0.2 and time 30 min, feed temperature of 25°C ± 3°C, and transmembrane pressure of 1 bar).

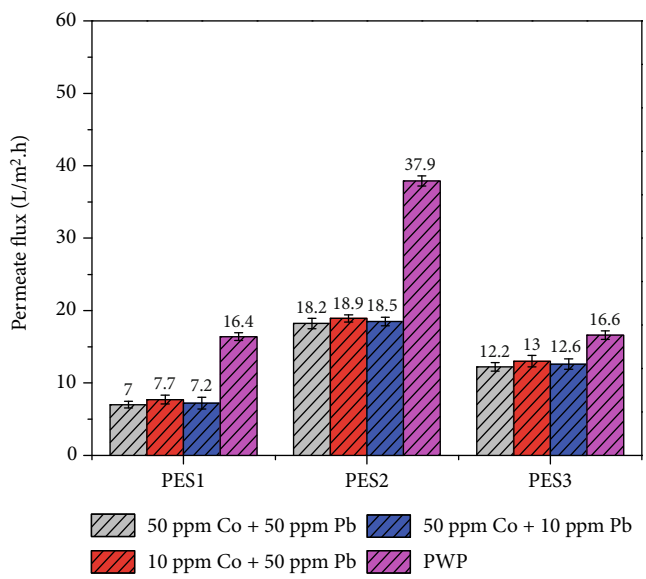

Figure 3: Effect of initial feed concentration of binary aqueous solutions containing Co^{2+} ions and Pb^{2+} ions on permeate flux for three types of PES hollow fiber membrane (pH 6 ± 0.2 and time 30 min, feed temperature of 25°C ± 3°C, and transmembrane pressure of 1 bar).

where C_p is the concentration (ppm) of metal ions in permeate, and C_b (ppm) is an average of bulk concentration of metal ions in the feed (C_f, ppm) and concentrate/retentate (C_r, ppm) and is calculated using Equation (3).

$$C_p = \frac{C_f + C_r}{2}. \quad (4)$$

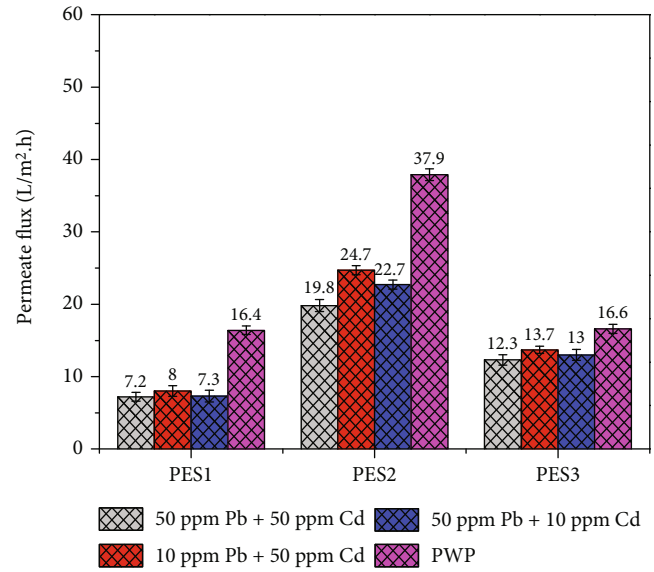

Figure 4: Effect of initial feed concentration of binary aqueous solutions containing Co^{2+} ions and Cd^{2+} ions on permeate flux for three types of PES hollow fiber membrane (pH 6 ± 0.2 and time 30 min, feed temperature of 25°C ± 3°C, and transmembrane pressure of 1 bar).

To clean the setup, distilled water was used to rinse it for 60 min at 4 bar pressure after each set of experiments. Permeate of pure water then was measured to make sure that the initial flux of the membrane is restored.

The concentrations of metal ions in the samples were measured by an AAS-6200 atomic absorption flame emission spectrophotometer (Shimadzu Company, Japan). This equipment was frequently calibrated before start measuring each set of samples.

3. Results and Discussion

3.1. The Separation Performance of PES Fibers for Binary Solutions. The performance of separation Co^{2+}, Cd^{2+}, and Pb^{2+}ions from binary solutions using PES hollow fiber membranes was studied by measuring the permeate flux (shown in Figures 2–4) and metals rejection (Figures 5–7). Comparing to the permeate flux of pure distilled water (PWP), the results presented in Figures 2–4 show that all types of PES fibers gave permeation flux lower than for pure water permeate. PES2 had significantly higher flux among the other types when they were used for simulated wastewater. These results can be illustrated as that the efficacy of hollow fiber highly depends on the texture properties of membrane such as the wall thickness of the fiber, porosity, pore size, and pore size distribution at the fiber surface shown in Table 1. The characterization of PES2, PES1, and PES3 discussed previously in [35] showed that PES2 had the lower thickness, wider pore size distribution, larger pore size, and porosity; thus, it gave the higher permeation flux.

Figure 2 displays the effect of initial Pb^{2+} ion and Cd^{2+} ion concentration on the permeate flux for three types of PES membrane used for the separation of binary aqueous

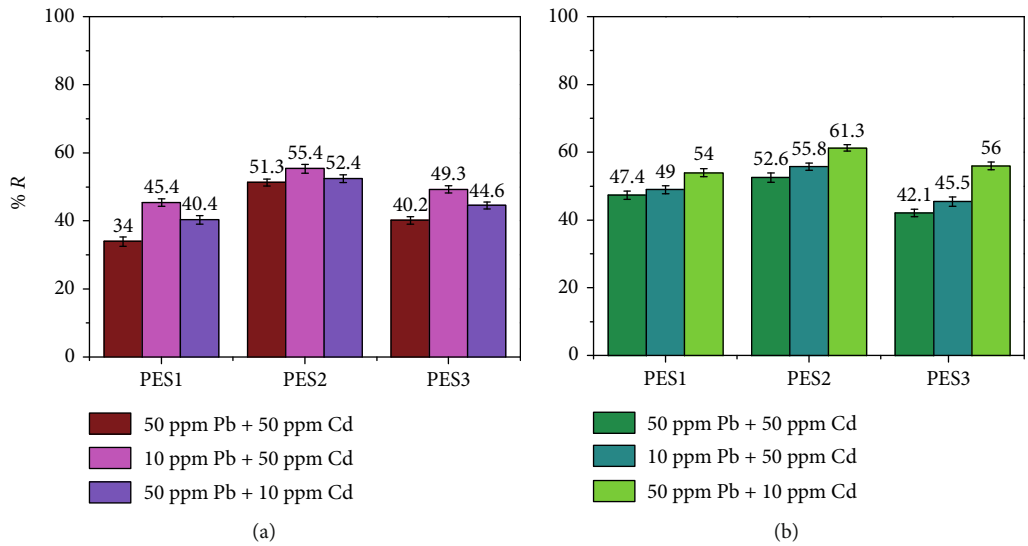

Figure 5: Effect of initial feed concentration of binary aqueous solutions containing Pb^{2+} ions and Cd^{2+} ions on rejection for three types of PES hollow fiber membrane (pH 6 ± 0.2 and time 30 min, feed temperature of 25°C ± 3°C, and transmembrane pressure of 1 bar). (a) Pb^{2+} ions. (b) Cd^{2+} ions.

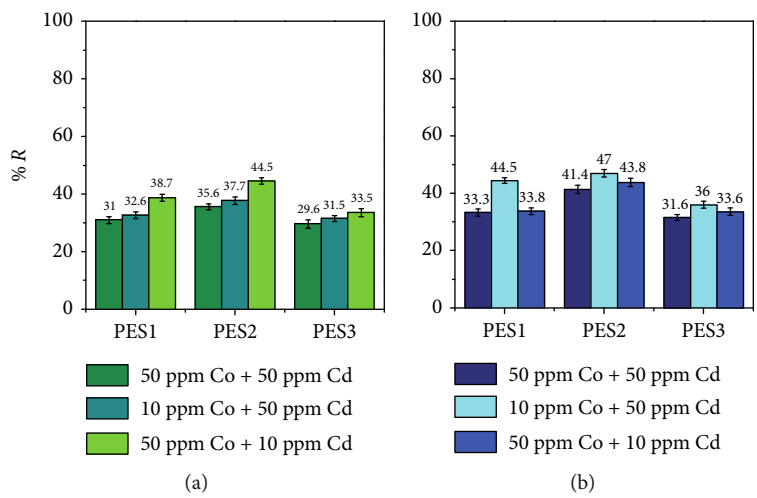

Figure 6: Effect of initial feed concentration of binary aqueous solutions containing Cd^{2+} ions and Co^{2+} ions on rejection for three types of PES hollow fiber membrane (pH 6 ± 0.2 and time 30 min, feed temperature of 25°C ± 3°C, and transmembrane pressure of 1 bar). (a) Cd^{2+} ions. (b) Co^{2+} ions.

solution at pH 6 ± 0.2 for a time of 30 min. For three types of fibers, changing the concentration ratio of Pb^{2+} ions to Cd^{2+} ions did not make change in the permeate flux in spite of reducing the concentration of Pb^{2+} ions to 10 ppm in the feed solution that slightly rose the flux. The maximum permeate flux obtained in this case was 23.7 L/m^2·h.

Figure 3 displays the effect of initial Co^{2+} ion and Pb^{2+}ion concentration on the permeate flux for three types of PES membrane used for the separation of binary aqueous solution at pH 6 ± 0.2 for a time of 30 min. A comparison based on the permeation flux, same results were obtained for the three types of fibers when the concentration ratio of Pb^{2+} ions to Co^{2+} ions was changed in the feed solution. Also, reducing the concentration of Pb^{2+} ions to 10 ppm in the feed solution caused slight increased the permeate flux to reach the maximum permeate flux of 18.9 L/m^2·h.

The same results were obtained from Figure 4 that presents the effect of initial Cd^{2+} ion and Co^{2+} ion concentration on the permeate flux of PES1 and PES3 membrane used for the separation of binary aqueous solution at pH 6 ± 0.2 for a time of 30 min. The permeate flux obtained by PES2 was obviously changed when the Pb^{2+} ion concentration to Co^{2+} ion concentration changed in the feed solution, whereas the maximum permeation flux obtained was 24.7 L/m^2·h when the concentration of Pb^{2+} ions in the feed solution was 10 ppm.

Figure 5 shows the rejection of Pb^{2+} ions and Cd^{2+} ions from binary aqueous solutions using three types of PES

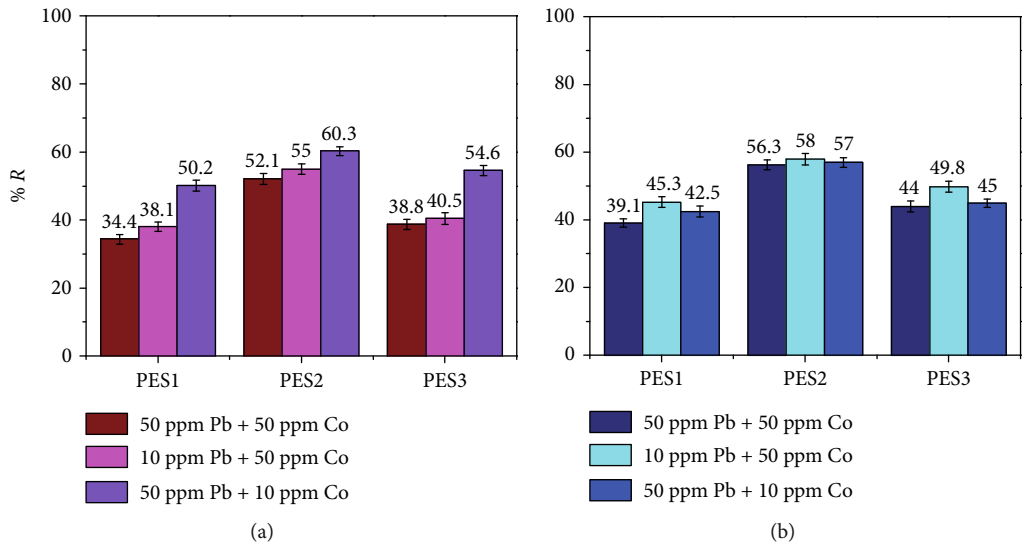

Figure 7: Effect of initial feed concentration of binary aqueous solutions containing Pb^{2+} ions and Co^{2+} ions on rejection for three types of PES hollow fiber membrane (pH 6 ± 0.2 and time 30 min, feed temperature of 25°C ± 3°C, and transmembrane pressure of 1 bar). (a) Pb^{2+} ions. (b) Co^{2+} ions.

hollow fiber membrane. In general, the rejection of Cd^{2+} ions was higher than of Pb^{2+} ions for different concentrations using all three types of membranes. The rejection of Cd^{2+} ions was higher when the initial concentration of Cd^{2+} ions was lower than the initial concentration of Pb^{2+} ions (i.e., 50 ppm Pb^{2+} ions: 10 ppm Cd^{2+} ions). Also, the rejection of Pb^{2+} ions increased when the initial concentrations were in the following sequence: 10 ppm Pb^{2+} ions : 50 ppm Cd^{2+} ions > 50 ppm Pb^{2+} ions : 10 ppm Cd^{2+} ions > 50 ppm Pb^{2+} ions : 50 ppm Cd^{2+} ions. Therefore, the higher rejection of Cd^{2+} ions (61.3%) was obtained using PES2 when the initial concentrations were 50 ppm of Pb^{2+} ions and 10 ppm of Cd^{2+} ions; however, it was 55.4% for Pb^{2+} ions when the initial concentrations were 10 ppm of Pb^{2+} ions and 50 ppm of Cd^{2+} ions using PES2.

Figure 6 shows the rejection of Co^{2+} ions and Cd^{2+} ions from binary aqueous solutions using three types of PES hollow fiber membrane. The results show that the rejection of Co^{2+} ions was higher than of Cd^{2+} ions for different concentrations using all three types of membranes, except when the initial feed contained 50 ppm Co^{2+} ions: 10 ppm Cd^{2+} ions, the rejection of both metals were convergent. The rejection of Cd^{2+} ions kept the same behavior obtained above as it was higher when the initial concentration of Cd^{2+} ions were in the following sequence: 50 ppm Co^{2+} ions : 10 ppm Cd^{2+} ions > 10 ppm Co^{2+} ions : 50 ppm Cd^{2+} ions > 50 ppm Pb^{2+} ions : 50 ppm Cd^{2+} ions. The rejection of Co^{2+} ions rose when the initial concentrations were in the following sequence: 10 ppm Co^{2+} ions : 50 ppm Cd^{2+} ions > 10 ppm Co^{2+} ions : 50 ppm Cd^{2+} ions > 50 ppm Pb^{2+} ions : 50 ppm Cd^{2+} ions. According to this, the higher rejection of Cd^{2+} ions (44.5%) was obtained using PES2 when the initial concentrations were 50 ppm Co^{2+} ions: 10 ppm of Cd^{2+} ions; but it was 47% for Co^{2+} ions when the initial concentrations were 10 ppm Co^{2+} ions and 50 ppm of Cd^{2+} ions using PES2.

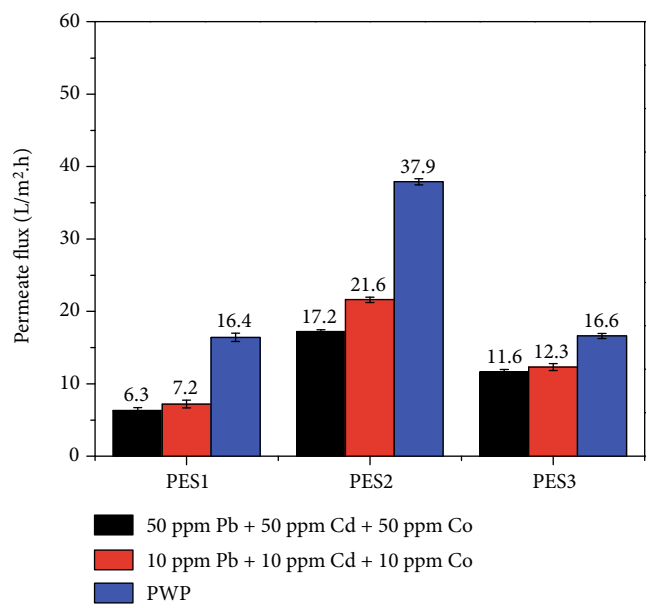

Figure 8: Effect of initial feed concentration of ternary aqueous solutions on permeate flux for three types of PES hollow fiber membrane (pH 6 ± 0.2 and time 30 min, feed temperature of 25°C ± 3°C, and transmembrane pressure of 1 bar).

The results of present rejection of Pb^{2+} ions and Co^{2+} ions from a binary solution containing using for three types of PES hollow fibers membrane are shown in Figure 7. Both the metal ions had the same behavior as before when they were incorporated with Cd^{2+} ions in binary solutions. The maximum rejection of Pb^{2+} ions (60.3%) was achieved using PES2 when the initial concentrations were 10 ppm Pb^{2+} ions: 50 ppm Co^{2+} ions, while the maximum rejection of Co^{2+} ions (58%) was achieved using PES2 when the initial concentrations were 10 ppm Pb^{2+} ions: 50 ppm Co^{2+} ions.

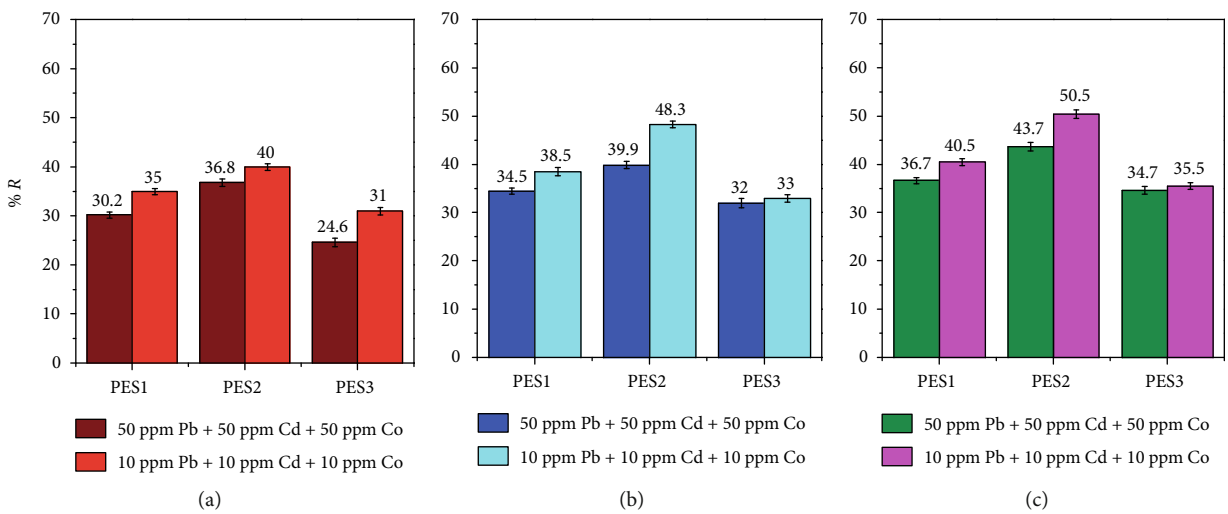

Figure 9: Effect of initial feed concentration of ternary aqueous solutions on the rejection for three types of PES hollow fiber membrane (pH 6 ± 0.2 and time 30 min, feed temperature of 25°C ± 3°C, and transmembrane pressure of 1 bar). (a) Pb^{2+} ions, (b) Cd^{2+} ions, and (c) Co^{2+} ions.

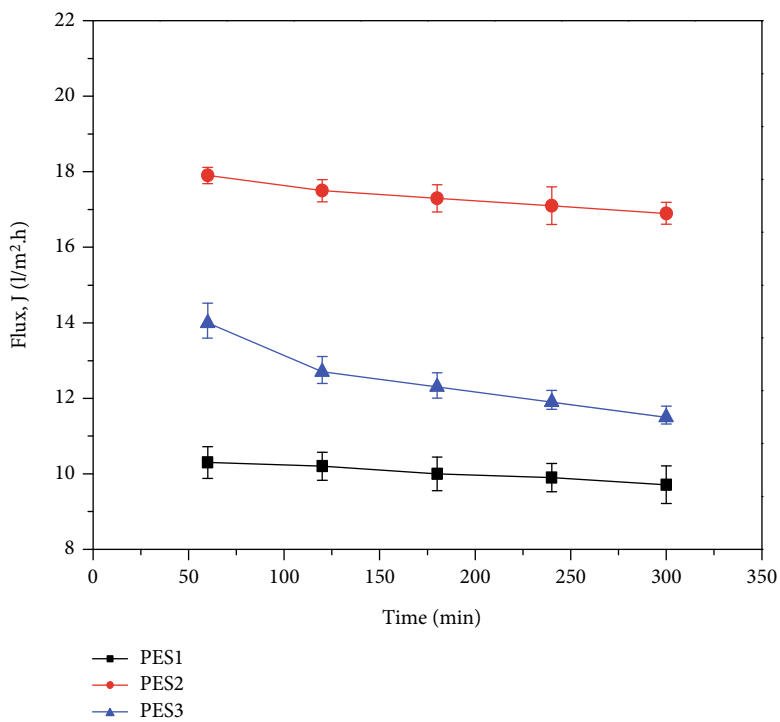

Figure 10: Effect of operating times for ternary aqueous solutions on permeate flux for three types of PES hollow fiber membrane (pH 6 ± 0.2 and time 300 min, feed temperature of 25°C ± 3°C, and transmembrane pressure of 1 bar) and concentration of metal ions 100 ppm.

In short words, for a separation of binary system using PES fibers, the higher rejection of metal can be obtained when its initial concentration was reduced to be less than the initial concentration of the other metal presenting in the same solution. Far from the effect of ionic radius of the studied metals on the removal process based on the sieving property of the membrane texture, this result can be related to the metal solubility in the aqueous solutions. Since the solubility of metal salts depends on the metal ion concentration and the pH of the solution, it is likely that the pH of a single metal solution changed when another metal ions is added which alters the solubility of metal ions in the solution [36, 37]. Increasing the solubility of metal ions due to the pH change leads to increase the tendency of metals to attach to water molecules and pass through the membrane pores within the permeate. Therefore, the rejection of the single

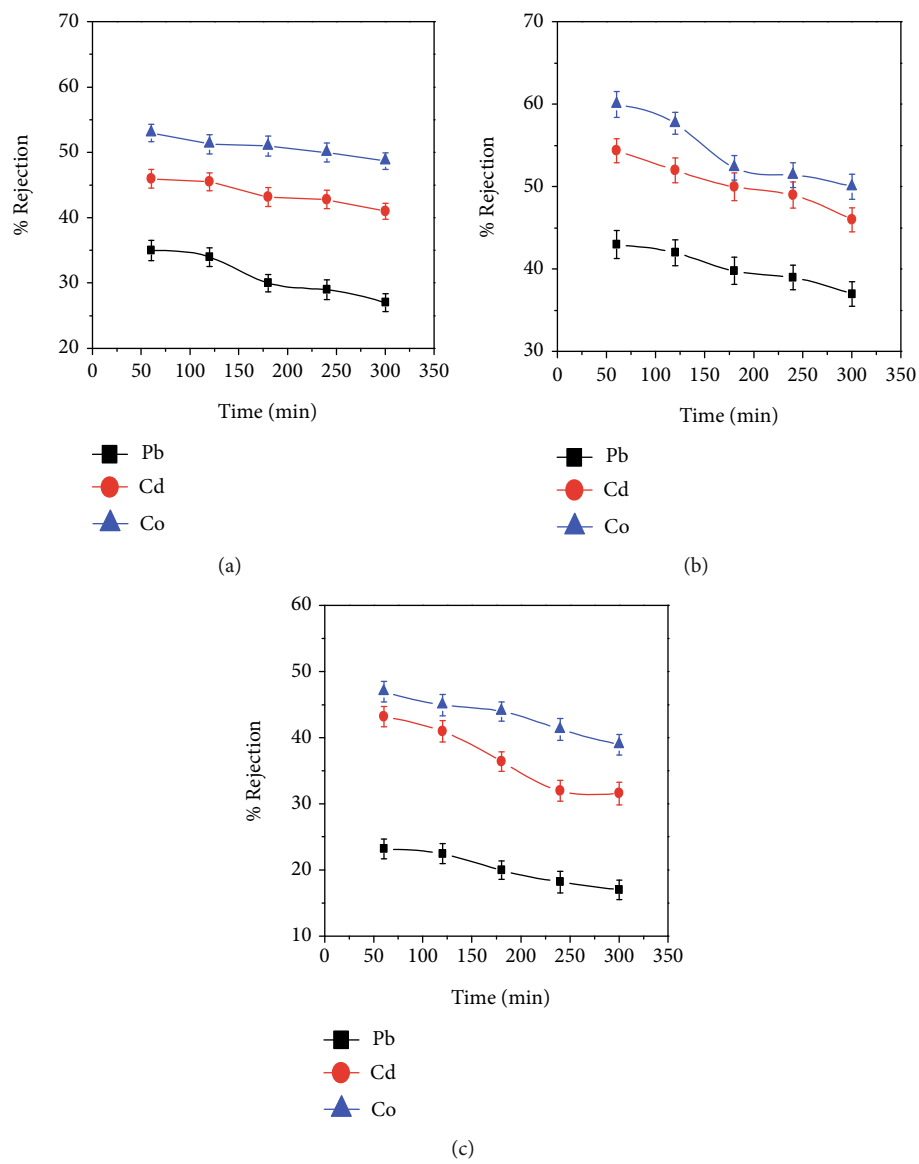

Figure 11: Effect of operating times for ternary aqueous solutions on rejection for three types of PES hollow fiber membrane (pH 6 ± 0.2 and time 300 min, feed temperature of 25°C ± 3°C, and transmembrane pressure of 1 bar) and concentration of metal ions 100 ppm. (a) PES1, (b) PES2, and (c) PES3.

metals using the prepared PES fibers was significantly higher the rejection of them when they were incorporated in binary solutions in the current study [35].

3.2. The Separation Performance of PES Fibers for Ternary Solutions. Figure 8 shows the performance of the three prepared PES membranes during the separation process of the metal ions from ternary solution of two different initial metal concentrations (10 and 50 ppm). PES2 gave higher permeate flux than other membranes followed by PES3 and PES1, which can be attributed to the distinguished texture properties of PES2. The permeation flux of PES2 was 21.6 ($L/m^2 \cdot h$) when the initial metal concentrations was 10 ppm; however, it obviously dropped to 17.2 ($L/m^2 \cdot h$) when the initial metal concentrations increased to 50 ppm. The permeate flux given by both PES1 and PES3 did not significantly vary when the initial metal concentrations changed from 10 to 50 ppm.

Figure 9 shows the rejection of the studied heavy metals from a ternary solution by three types of PES membranes in the separation process at a feed temperature of 25°C, pH = 6 ± 0.2, and transmembrane pressure of 1 bar. According to the increasing of the rejection of the metals ions, the membranes were in the following order: PES2 > PES1 > PES3. Despite the ionic radius of these metals (Co^{2+} ions of 79 pm, Cd^{2+} ions of 97 pm, Pb^{2+} ions of 133 pm) [38], the tendency of each membrane towards the selected metals ions was as follows: Co^{2+} ions > Cd^{2+} ions > Pb^{2+} ions. This result can be attributed to that presence of Cd^{2+} ions and Co^{2+} ions in the solution containing Pb^{2+} ions led to change

Table 2: Comparison results of the present work and other membranes found in the literature that used for rejection of metal ions by considering the different parameters.

Membrane	Process	Heavy metals	Pressure (bar)	Heavy metal concentration	pH value	Rejection (%)	PWF (L/m^2 h)	Ref.
PES (dead-end mode)	Complexation and UF-filtration with poly(itaconic acid)	Pb^{2+} Sn^{2+} Zn^{2+} Cu^{2+} Cd^{2+}	-	20 (ppm)	7	83.8 63.9 57.1 61.4 36.5	46.1	[39]
PVDF/APTES functionalized halloysite-magnetic graphene oxide/metformin	NF	Cu^{2+} Cd^{2+} Cr^{2+}	5	5 (ppm)	5.5	47.9 44.2 52.3	14.2	[40]
Dual layer polybenzimidazole/PES	NF	Cr^{2+} Pb^{2+} Cd^{2+}		200 (ppm)	12 2.2 7	98 93 70	8.3	[41]
DL provided by SEPA CF GE Osmonics, Florida, USA	NF (crossflow mode)	Cd^{2+} Zn^{2+} Cu	3	0.001 Mol/l	6.83	48 60 65	20	[42]
Polyamide flat sheet, spiral wound	Flat-sheet, spiral wound NF	Pb^{2+} Ni^{2+}	6	1	3-4	86 93	-	[43]
NF270 commercial membrane	Flat-sheet NF	Pb^{2+} Cd^{2+} Mn As	5	2000 (ppm)	1.5-5	74 99	12-33.8	[44]
PES membrane	Hollow fiber UF	Ternary Pb^{2+} Cd^{2+} Co^{2+}	1	10-50 (ppm)	6	40 48.3 50.5	16.4 37.9 16.6	This study
PES membrane	Hollow fiber UF	Binary Pb^{2+} Co^{2+} Cd^{2+}	1	10-50 (ppm)	6	60.3 58 44.5		This study

the pH of the solution and increase the solubility of Pb^{2+} ions in the solution. Also, increasing the initial metal concentration reduced the rejection of all metals using three types of PES membranes. This behavior is obvious for PES2 membranes for Co^{2+} ions and Cd^{2+} ions; however, it was obvious for PES3 for Pb^{2+} ions.

Figure 10 shows the permeate flux for the three types of PES fibers with time of separation ternary aqueous solutions. The figure shows a slightly reduction in the permeate flux of the three types of PES fibers with operation time which can be due to the metal ion deposition on the fiber surface.

Figure 11 shows the rejection of Co^{2+} ions, Cd^{2+} ions, and Pb^{2+} ions from a ternary solution containing 100 ppm of each metal and pH of 6 ± 0.2 using three different PES membranes with operating time. The rejection of Cd^{2+} ions and Co^{2+} ions reduced sharply by both PES2 and PES3; however, the rejection of Pb^{2+} ions reduced similarly for the three membrane types. The maximum rejection obtained by PES2 was 60% for Co^{2+} ions, 54.4% for Cd^{2+} ions, and 43% for Pb^{2+} ions after 50 min. The minimum rejection obtained by PES2 was 50% for Co^{2+} ions, 46% for Cd^{2+} ions, and 37% for Pb^{2+} ions after 300 min.

From the results of the current work, it can be observed that the rejection of the Co^{2+} ions was higher than Pb^{2+} ions. Both Co^{2+} and Pb^{2+} are co-ions; however, Pb^{2+} has a larger ability than Co^{2+} to move through the membrane under the effect of electrical potential gradient, and thus low rejection of Pb^{2+} ions was obtained. This can be because of the higher diffusivity that Pb^{2+} ions have (e.g., DPb^{2+}, $\infty = 9.45 \times 10^{-10}$ m^2/s and DCo^{2+}, $\infty = 7.32 \times 10^{-10}$ m^2/s). Also, the rejection of Co^{2+} ions was higher than that of the Cd^{2+} ions due to the slower movement of Co^{2+} within the membrane than Cd^{2+} under the effect of electrical potential gradient; therefore, lower cadmium rejected was obtained. This trend can be because of the higher diffusivity that Cd^{2+} ions have (e.g., DCd^{2+}, $\infty = 14.4 \times 10^{-10}$ m^2/s and DCo^{2+}, $\infty = 7.32 \times 10^{-10}$ m^2/s). Regarding the rejection mechanism of Pb^{2+}/-Cd^{2+} aqueous solution, it can be noticed that lower rejection of Pb^{2+} than Cd^{2+} because of the lower hydration energy of Pb^{2+} ions (e.g., -1755 kJ/mol of $Cd^{2+} > -1425$ kJ/mol of

Pb^{2+}). The competitive removal of heavy metals for each membrane was reduced with increasing of the initial metal ion concentration due to the Donnan effect. When the pH value is higher than the isoelectric point (e.g., pH>5.5), the membrane surface has negative charge, whereas the metal ions are positively charged which increase the attraction between them. Also, increasing the metal ion initial concentrations leads to increasing the accumulation of ions on the surface of the membrane which causes clogging of pores, formation of cake layer, increasing the concentration polarization, and thus low ions rejection.

3.3. Comparative Study. Table 2 shows comparison results between the present work and other membranes found in the literature that are used for metal ion removal with considering different parameters. Also, this table presents the most important operating parameters such as feed solution pH, initial concentration of the heavy metals ions, and *trans*-membrane pressure. The performance factor of the three PES membranes used in the present work simultaneously has reasonable values of the metal ion (Pb^{2+}, Cd^{2+}, and Co^{2+}) rejection in comparison with that of different membrane separation processes selected from the literature. Moreover, it can be observed that the rejection of most of the heavy metals present simultaneously in a solution reduced in the same way of their rejection from solutions in which they individually present.

4. Conclusions

The current work studied the removal of Co^{2+} ions, Cd^{2+} ions, and Pb^{2+} ions from binary and ternary solutions using three types of PES membranes. PES2 proved its performance in the separation process for the binary and ternary solutions at different initial concentrations. The performance of the selected metal ions during the separation process changed when they were incorporated in binary or ternary aqueous solutions. For binary solutions, all the metals had high rejection when their initial concentration was lower than the initial concentration of the other metal present in the same solution. However, for ternary solution, the tendency of the three types of fibers tended to remove the metal ions according to this sequence: Co^{2+} ions > Cd^{2+} ions > Pb^{2+} ions. Also, the rejection of metals ions was higher when their initial concentrations reduced from 50 ppm to 10 ppm. Finally, the groundwater containing Co^{2+} ions, Cd^{2+} ions, and Pb^{2+} ions can be efficiently treated by the filtration process using PES hollow fibers.

Data Availability

The underlying data used to support the findings of the current work are included within the text of the manuscript.

Conflicts of Interest

The authors declare no conflict of interest.

References

[1] M. A. Momodu and C. A. Anyakora, "Heavy metal contamination of ground water: the Surulere case study," *Research Journal of Environmental and Earth Sciences*, vol. 2, pp. 39–43, 2010.

[2] E. Vetrimurugan, K. Brindha, L. Elango, and O. M. Ndwandwe, "Human exposure risk to heavy metals through groundwater used for drinking in an intensively irrigated river delta," *Applied Water Science*, vol. 7, no. 6, pp. 3267–3280, 2017.

[3] Y. Sang, F. Li, Q. Gu, C. Liang, and J. Chen, "Heavy metal-contaminated groundwater treatment by a novel nanofiber membrane," *Desalination*, vol. 223, no. 1-3, pp. 349–360, 2008.

[4] W. Qiu and Y. Zheng, "Removal of lead, copper, nickel, cobalt, and zinc from water by a cancrinite-type zeolite synthesized from fly ash," *Chemical Engineering Journal*, vol. 145, no. 3, pp. 483–488, 2009.

[5] S. Bouranene, P. Fievet, A. Szymczyk, M. El-Hadi Samar, and A. Vidonne, "Influence of operating conditions on the rejection of cobalt and lead ions in aqueous solutions by a nanofiltration polyamide membrane," *Journal of Membrane Science*, vol. 325, no. 1, pp. 150–157, 2008.

[6] A. Bhatnagar, A. K. Minocha, and M. Sillanpää, "Adsorptive removal of cobalt from aqueous solution by utilizing lemon peel as biosorbent," *Biochemical Engineering Journal*, vol. 48, no. 2, pp. 181–186, 2010.

[7] D. Rana, T. Matsuura, M. A. Kassim, and A. F. Ismail, "Radioactive decontamination of water by membrane processes – A review," *Desalination*, vol. 321, pp. 77–92, 2013.

[8] R. D. Ambashta and M. E. T. Sillanpää, "Membrane purification in radioactive waste management: a short review," *Journal of Environmental Radioactivity*, vol. 105, pp. 76–84, 2012.

[9] Y. Park, Y.-C. Lee, W. S. Shin, and S.-J. Choi, "Removal of cobalt, strontium and cesium from radioactive laundry wastewater by ammonium molybdophosphate–polyacrylonitrile (AMP–PAN)," *Chemical Engineering Journal*, vol. 162, no. 2, pp. 685–695, 2010.

[10] T. K. Hussein, "Comparative study for removal of Zn+2 ions from aqueous solutions by adsorption and forward osmosis," *Iraqi Journal of Chemical and Petroleum Engineering*, vol. 18, pp. 125–138, 2017.

[11] D. A. de Haro-Del Rio, S. M. Al-Jubouri, and S. M. Holmes, "Hierarchical porous structured zeolite composite for removal of ionic contaminants from waste streams," *Chimica Oggi-Chemistry Today*, vol. 35, pp. 26–29, 2017.

[12] S. M. Al-Jubouri and S. M. Holmes, "Immobilization of cobalt ions using hierarchically porous 4A zeolite-based carbon composites: ion-exchange and solidification," *Journal of Water Process Engineering*, vol. 33, article 101059, 2020.

[13] A. Ahmad, J. A. Siddique, M. A. Laskar et al., "New generation Amberlite XAD resin for the removal of metal ions: a review," *Journal of Environmental Sciences*, vol. 31, pp. 104–123, 2015.

[14] Y. Cui, Q. Ge, X. Y. Liu, and T. S. Chung, "Novel forward osmosis process to effectively remove heavy metal ions," *Journal of Membrane Science*, vol. 467, pp. 188–194, 2014.

[15] Y. C. Xu, Z. X. Wang, X. Q. Cheng, Y. C. Xiao, and L. Shao, "Positively charged nanofiltration membranes via economically mussel-substance-simulated co-deposition for textile wastewater treatment," *Chemical Engineering Journal*, vol. 303, pp. 555–564, 2016.

[16] A. Hashlamon, A. W. Mohammad, and A. Ahmad, "The effect of wastewater pre-treatment on nanofiltration membrane performance," *Journal of Water Reuse and Desalination*, vol. 7, no. 1, pp. 45–52, 2017.

[17] M. Said, A. Ahmad, A. W. Mohammad, M. T. M. Nor, and S. R. Sheikh Abdullah, "Blocking mechanism of PES membrane during ultrafiltration of POME," *Journal of Industrial and Engineering Chemistry*, vol. 21, pp. 182–188, 2015.

[18] E. Ellouze, N. Tahri, and R. B. Amar, "Enhancement of textile wastewater treatment process using nanofiltration," *Desalination*, vol. 286, pp. 16–23, 2012.

[19] X. Liu, J. Wu, C. Liu, and J. Wang, "Removal of cobalt ions from aqueous solution by forward osmosis," *Separation and Purification Technology*, vol. 177, pp. 8–20, 2017.

[20] Q. F. Alsalhy, R. S. Almukhtar, and H. A. Alani, "Oil refinery wastewater treatment by using membrane bioreactor (MBR)," *Arabian Journal for Science and Engineering*, vol. 41, no. 7, pp. 2439–2452, 2016.

[21] Q. F. Alsalhy, F. H. al-Ani, and A. E. al-Najar, "A new Sponge-GAC-Sponge membrane module for submerged membrane bioreactor use in hospital wastewater treatment," *Biochemical Engineering Journal*, vol. 133, pp. 130–139, 2018.

[22] Q. F. Alsalhy, F. H. al-Ani, A. E. al-Najar, and S. I. A. Jabuk, "A study of the effect of embedding ZnO-NPs on PVC membrane performance use in actual hospital wastewater treatment by membrane bioreactor," *Chemical Engineering and Processing - Process Intensification*, vol. 130, pp. 262–274, 2018.

[23] M. Y. Ghadhban, H. S. Majdi, K. T. Rashid et al., "Removal of dye from a leather tanning factory by flat-sheet blend ultrafiltration (UF) membrane," *Membranes (Basel)*, vol. 10, no. 3, p. 47, 2020.

[24] D. M. Al-Ani, F. H. Al-Ani, Q. F. Alsalhy, and S. S. Ibrahim, "Preparation and characterization of ultrafiltration membranes from PPSU-PES polymer blend for dye removal," *Chemical Engineering Communications*, vol. 208, no. 1, pp. 41–59, 2021.

[25] F. H. Al-Ani, Q. F. Alsalhy, R. S. Raheem, K. T. Rashid, and A. Figoli, "Experimental investigation of the effect of implanting TiO_2-NPs on PVC for long-term UF membrane performance to treat refinery wastewater," *Membranes (Basel)*, vol. 10, no. 4, p. 77, 2020.

[26] A. Abdel-Karim, S. Leaper, M. Alberto et al., "High flux and fouling resistant flat sheet polyethersulfone membranes incorporated with graphene oxide for ultrafiltration applications," *Chemical Engineering Journal*, vol. 334, pp. 789–799, 2018.

[27] A. A. Shawkat, Z. W. Rashad, A. A. Rashad et al., "Produced water treatment using ultrafiltration and nanofiltration membranes," *Al-Khwarizmi Engineering Journal*, vol. 12, pp. 10–18, 2016.

[28] F. Fu and Q. Wang, "Removal of heavy metal ions from wastewaters: a review," *Journal of Environmental Management*, vol. 92, no. 3, pp. 407–418, 2011.

[29] Z. Thong, G. Han, Y. Cui et al., "Novel nanofiltration membranes consisting of a sulfonated pentablock copolymer rejection layer for heavy metal removal," *Environmental Science & Technology*, vol. 48, no. 23, pp. 13880–13887, 2014.

[30] C.-V. Gherasim, K. Hancková, J. Palarčík, and P. Mikulášek, "Investigation of cobalt (II) retention from aqueous solutions by a polyamide nanofiltration membrane," *Journal of Membrane Science*, vol. 490, pp. 46–56, 2015.

[31] R. Epsztein, E. Shaulsky, N. Dizge, D. M. Warsinger, and M. Elimelech, "Role of ionic charge density in Donnan exclusion of monovalent anions by nanofiltration," *Environmental Science & Technology*, vol. 52, no. 7, pp. 4108–4116, 2018.

[32] G. Basaran, D. Kavak, N. Dizge, Y. Asci, M. Solener, and B. Ozbey, "Comparative study of the removal of nickel(II) and chromium(VI) heavy metals from metal plating wastewater by two nanofiltration membranes," *Desalination and Water Treatment*, vol. 57, no. 46, pp. 21870–21880, 2016.

[33] Q. F. Alsalhy, K. T. Rashid, S. S. Ibrahim et al., "Poly(vinylidene fluoride-co-hexafluoropropylene) (PVDF-*co*-HFP) hollow fiber membranes prepared from PVDF-*co*-HFP/PEG-600Mw/DMAC solution for membrane distillation," *Journal of Applied Polymer Science*, vol. 129, no. 6, pp. 3304–3313, 2013.

[34] Q. F. Alsalhy, A. Merza, K. Rashid et al., "Preparation and characterization of poly(vinyl chloride)/polystyrene/poly(ethylene glycol) hollow-fiber ultrafiltration membranes," *Journal of Applied Polymer Science*, vol. 130, no. 2, pp. 989–1004, 2013.

[35] S. Hadi, A. A. Mohammed, S. M. Al-Jubouri et al., "Experimental and theoretical analysis of lead Pb^{2+} and Cd^{2+} retention from a single salt using a hollow fiber PES membrane," *Membranes (Basel)*, vol. 10, no. 7, p. 136, 2020.

[36] S. M. al-Jubouri, H. A. Sabbar, H. A. Laft, and B. I. Waisi, "Effect of synthesis parameters on the formation 4A zeolite crystals: characterization analysis and heavy metals uptake performance study for water treatment," *Desalination and Water Treatment*, vol. 165, pp. 290–300, 2019.

[37] H. Karimi, "Effect of pH and initial pb(II) concentration on the lead removal efficiency from industrial wastewater using $Ca(OH)_2$," *International Journal of Water and Wastewater Treatment*, vol. 3, no. 2, 2017.

[38] R. Petrucci and F. G. Herring, *General Chemistry Principle and Modern Aplication*, Prentice Hall, Upper Saddle River: NJ, USA, 6th edition, 1993.

[39] H. Rezania, V. Vatanpour, and S. Faghani, "Poly(itaconic acid)-assisted ultrafiltration of heavy metal ions' removal from wastewater," *Iranian Polymer Journal*, vol. 28, no. 12, pp. 1069–1077, 2019.

[40] G. Zeng, Y. He, Y. Zhan et al., "Novel polyvinylidene fluoride nanofiltration membrane blended with functionalized halloysite nanotubes for dye and heavy metal ions removal," *Journal of Hazardous Materials*, vol. 317, pp. 60–72, 2016.

[41] W. P. Zhu, S. P. Sun, J. Gao, F. J. Fu, and T. S. Chung, "Dual-layer polybenzimidazole/polyethersulfone (PBI/PES) nanofiltration (NF) hollow fiber membranes for heavy metals removal from wastewater," *Journal of Membrane Science*, vol. 456, pp. 117–127, 2014.

[42] C. Fersi Bennani and O. M'hiri, "Comparative study of the removal of heavy metals by two nanofiltration membranes," *Desalination and Water Treatment*, vol. 53, pp. 1024–1030, 2013.

[43] A. Maher, M. Sadeghi, and A. Moheb, "Heavy metal elimination from drinking water using nanofiltration membrane technology and process optimization using response surface methodology," *Desalination*, vol. 352, pp. 166–173, 2014.

[44] B. A. M. al-Rashdi, D. J. Johnson, and N. Hilal, "Removal of heavy metal ions by nanofiltration," *Desalination*, vol. 315, pp. 2–17, 2013.

Hindawi
Geofluids
Volume 2020, Article ID 8836908, 10 pages
https://doi.org/10.1155/2020/8836908

Research Article

Environmental Evaluation of Coal Mines Based on Generalized Linear Model and Nonlinear Fuzzy Analytic Hierarchy

Xueming Du,[1,2,3] **Hongyuan Fang**,[1,3] **Kang Liu**,[1,3] **Binghan Xue**,[1,3] **and Xin Cai**[2]

[1]*College of Water Conservancy Engineering, Zhengzhou University, Zhengzhou 450001, China*
[2]*School of Resources and Safety Engineering, Central South University, Changsha, Hunan 410083, China*
[3]*National Local Joint Engineering Laboratory of Major Infrastructure Testing and Rehabilitation Technology, Zhengzhou 450001, China*

Correspondence should be addressed to Hongyuan Fang; 18337192244@163.com and Binghan Xue; zzuhan@163.com

Received 24 March 2020; Revised 5 August 2020; Accepted 26 August 2020; Published 23 September 2020

Academic Editor: Ilaria Fuoco

To create a good working environment for workers in coal mines and ensure that they can work safely and comfortably, environmental assessments of coal mines represent an important method used to achieve this goal. In this paper, a comprehensive environmental evaluation model of coal mines was established based on generalized linear theory and fuzzy analytic hierarchy processes. First, the importance degree of each index factor was obtained by analyzing the statistical source data of air, water, soil, ecological compensation, and other indexes that affect the ecological environmental safety of coal mines using generalized linear theory. Based on the importance degree of each index factor, a pairwise comparison matrix was constructed by the logarithmic fuzzy preference programming method, and the influence weight value of each index factor was accurately obtained through MATLAB software. The results indicated that the model can effectively reduce the impact of expert subjectivity on the evaluation results, which is consistent with the reality of coal mines. In addition, in the process of environmental assessment of coal mines, the model is proven to be convenient, precise, and easy to operate.

1. Introduction

Resource safety is an important part of national strategic safety, and the development of mineral resources is always an important mission [1–3]. In particular, in the past 30-40 years, the development of mineral resources has provided strong support and protection for the rapid development of the economy and society. Due to technological reasons and the pursuit of high profits, the strength of mine ecological protection and restoration management has not been as strong as people would prefer, leading to the intensification of the contradiction between the coal mine development and ecological safety, e.g., the high production rate of three wastes of coal mines, the long potential harm of radiation, and the serious pollution to the air, water and soil [2]. In particular, the disordered development in some areas has led to geological disasters, such as surface collapse and debris flow, which have intensified land desertification and led to the degradation of ecological environmental quality [3]. Therefore, it is urgent to explore a new technology of mine geological environmental governance and ecological restoration to prevent the further degradation of ecological health. The current ecological environmental safety assessment of coal mines can not only measure the overall status of the ecological quality of coal mines but also reflect the governance of the ecological environmental pollution. Additionally, it can quickly identify the important factors that cause the deterioration of the mine environment, allowing for the quick adoption of the most effective measures to control the "culprits" that make the mine environment worse.

Currently, many scholars have constructed a series of safety evaluation models, e.g., analytic hierarchy process, fuzzy comprehensive evaluation, grey theory, and neural network method, and applied them to mine ecological environmental safety evaluations. For instance, Zhao et al. [4] established an evaluation index system of the mine geological environment using the analytic hierarchy process (AHP) and applied this method to the mining field of Hainan Island; the

Table 1: Scale of triangular numbers with different importance.

Logical variable	Scale of TFN	Reciprocal scale of TFN
Equally important	(1, 1, 1)	(1, 1, 1)
Weakly important	(1/2, 1, 3/2)	(2/3, 1, 2)
Fairly important	(1, 3/2, 2)	(1/2, 2/3, 1)
Strongly important	(3/2, 2, 5/2)	(2/5, 1/2, 2/3)
Very strongly important	(2, 5/2, 3)	(1/3, 2/5, 1/2)
Extremely important	(5/2, 3, 7/2)	(7/2, 1/3, 2/5)

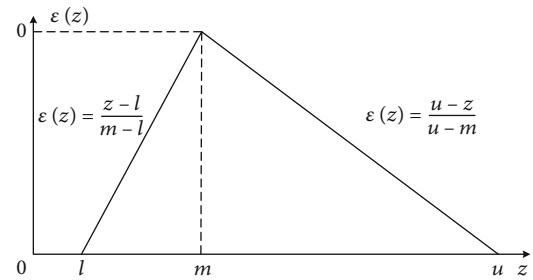

Figure 1: Triangular fuzzy number.

authors found that the evaluation value basically conformed to the situation of the mine site. Bascetin et al. [5] constructed a decision support system based on an analytical hierarchy process to evaluate the production of coal mines in Turkey. Samantra et al. [6] created an improved decision method based on fuzzy set theory and distinguished the ranges of evaluated risk ratings, ultimately suggesting an action requirement plan to guide the management of the mine environment. Yang et al. [7] selected four factors that affect the mine environment, including the water environment, atmospheric environment, geological disaster, and ecological environmental characteristics, as the evaluation factors to build a fuzzy comprehensive evaluation model of the mine environment for the quantitative study of the mine environment. Su et al. [8] established an engineering geological evaluation model based on grey mathematics theory and evaluated the engineering geological situation of typical mines by determining the evaluation weight index. Zhao et al. [9] used the principle of BP neural networks and the random interpolation method to build an evaluation model of the BP artificial neural network on mine ecological safety.

Each evaluation model has its own shortcomings. To fully consider the influence of all factors and present the comprehensive evaluation results scientifically and accurately, many scholars have combined various models to carry out comprehensive evaluations according to the characteristics of the different models, namely, the combined comprehensive evaluation model. For instance, based on fuzzy theory, Chen et al. [10] collected the key factors influencing the mine environment by remote sensing technology, determined the influence weight of the environmental evaluation factors by using AHP, and finally built the AHP-fuzzy mine environment evaluation model. Besides, Wei et al. [11] established the comprehensive evaluation of the underground heat source based on the AHP and fuzzy comprehensive evaluation (FCE) to construct the evaluation model, and some suggestions on thermal stress control are put forward. Based on the theories of uncertainty measurement evaluation (WME) and AHP, Dong et al. [12] established the comprehensive risk evaluation of underground goafs using multiple indexes. Dong et al. [13] also established and calibrate the comprehensive models using the random forest, support vector machine, Bayes' classifier, Fisher's classifier, logistic regression, and neural networks. Based on grey system theory, Wei et al. [14] used the analytic hierarchy process to determine the weight of each influencing factor and constructed a grey comprehensive evaluation model of the mine geological environment. To scientifically and accurately obtain the membership degree of each influencing factor, Liu et al. [15] built a fuzzy-grey combination evaluation model based on grey correlation analysis and fuzzy evaluation theory.

However, there are many factors that affect ecological environmental safety, and the relationship between the evaluation factors and the safety level is fuzzy, which makes the shortcomings of the current evaluation model more obvious. For instance, although the neural network model can overcome the subjectivity of expert experience and ensure a higher accuracy of evaluation results, it is easy to fall into the dilemma of a local minimum and slow convergence speed in the calculation process of weight, and this method cannot address the relationships between various index factors clearly. Although the AHP and grey theory evaluation methods can deal with the relationship of each index well, they rely on the experience of experts for evaluation when determining the weight of influencing factors; therefore, they cannot avoid subjectivity. The fuzzy analytic hierarchy process is the best method to address the fuzzy relationship of all factors; however, it also cannot avoid the evaluation of experts when building the comparison matrix.

To overcome the subjectivity of evaluation experts in the evaluation of the influence degree of each index factor and to further improve the uncertainty of data processing, in this paper, a comprehensive evaluation model of the coal mine environment is established based on generalized linear theory and fuzzy level theory. First, the importance of each index in relation to the target index is obtained by the initial statistics of the source data of each lowest level index based on generalized linear theory. Then, according to the statistical value obtained by generalized linear theory, the pairwise comparison matrix is constructed by the logarithmic fuzzy preference programming method (LFPP). Finally, the influence weight value of each index factor is accurately obtained through MATLAB software. The model is applied to a coal mine for an environmental assessment.

2. Methodology

2.1. Triangular Fuzzy Number Theory. There are many kinds of distribution functions used to imitate probability theory, such as the normal distribution function, trapezoid distribution function, triangular fuzzy number, k-th parabola distribution, Cauchy distribution, and S-type distribution. The triangular fuzzy numbers (TFN) is widely adopted to express the decision perception of alternatives' performances with respect to each criterion [16]. In order to easy the judgment

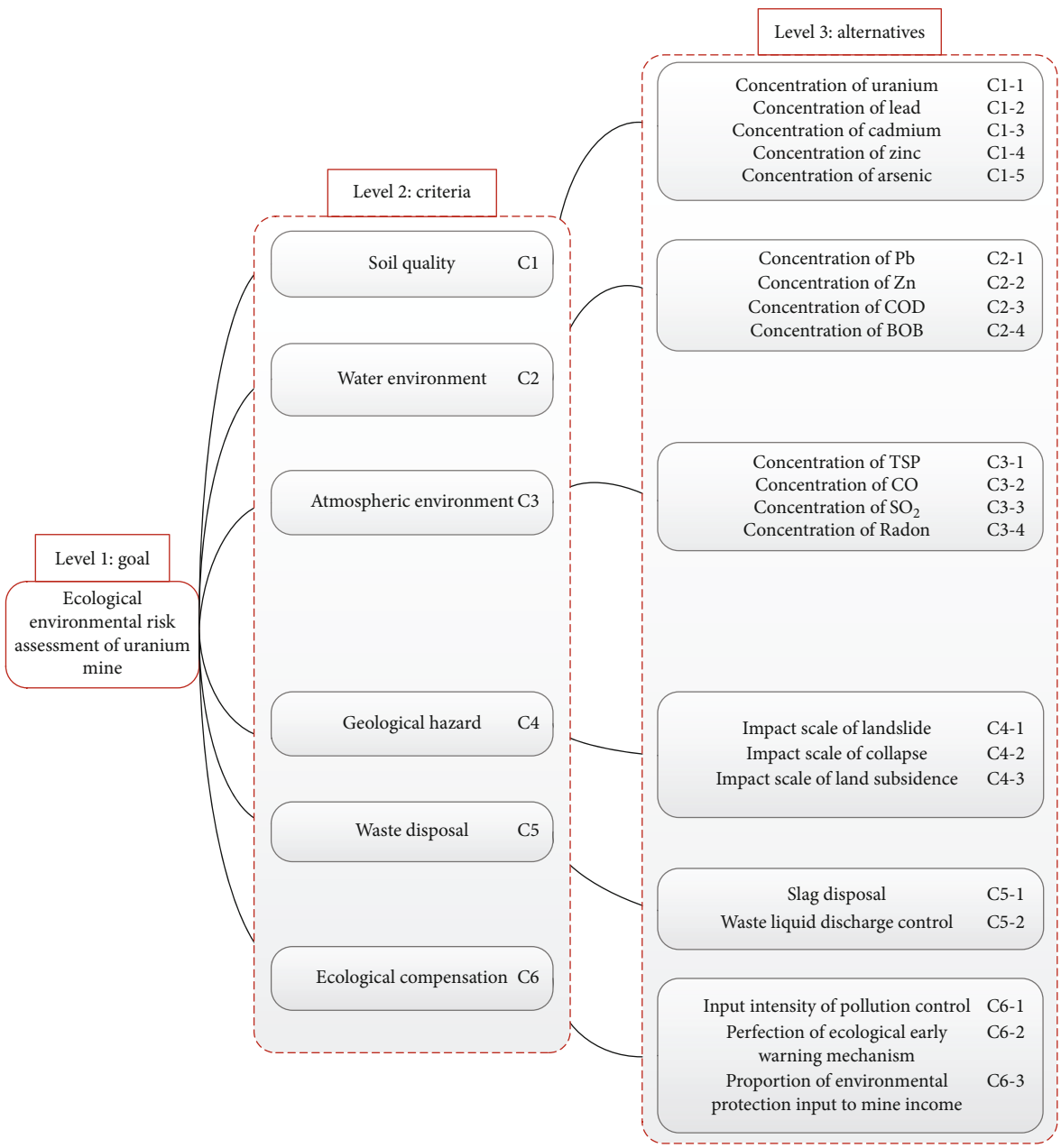

Figure 2: The diagram of environmental safety level analysis in coal mines.

Table 2: Statistical compensation indexes for mine ecological safety.

Year	Input intensity of pollution control	Improvement of ecological early warning system	Proportion of environmental protection investment to total income	Synthetic index of compensation
2005	40.7	1.72	3.88	0.27
2006	39.5	1.76	4.2	0.21
2007	38.6	1.76	4.48	0.20
2008	37.7	1.8	4.76	0.21
2009	36.8	1.8	5.08	0.23

process, linguistic variables are introduced (section 2.3), and it is a kind of variable whose values are not numbers but words and sentences [17]. Therefore, the triangular fuzzy theory is mainly used to build a model to evaluate the ecological environment of coal mines in this paper.

In a given region Z, for any $z \in Z$, the fuzzy set A can be defined as

$$A = \{(z, \varepsilon_A(z)) | z \in Z\}, \tag{1}$$

where ε_A is the membership degree of z to A and $\varepsilon_A(x) \in (0, 1)$.

Let l, m, and u be the minimum possible value, the intermediate value, and the maximum possible value of a certain

Table 3: Statistics of influencing factors of atmosphere, soil, and water in coal mines.

Point	Atmosphere				Synthetic index of atmosphere	Soil					Surface water				Synthetic index of water
	TSP	CO	SO_2	Rn		Pb	Zn	Cd	As	U	Pb^{2+}	Zn^{2+}	COD	BOD	
1	0.41	5.1	0.05	26.2	0.775	167.5	368	0.1	13.54	64.4	0.48	3.68	3.92	5.5	0.51
2	0.23	3.12	0.09	34.4	0.625	234.9	888	0.3	10.96	62.9	0.66	5.32	14.3	12.7	0.45
3	0.2	5.5	0.12	35	0.6	220	2339	0.6	9.63	56.8	0.57	4.43	15.6	17.1	0.26
4	0.3	4.4	0.11	133	0.45	224.8	1521	0.7	14.47	54.7	0.60	4.31	22	16.8	0.2
5	0.2	3.6	0.13	37.3	0.65	263.2	1267	0.4	12.1	60.3	0.52	5.07	24	19.1	0.2
6	0.2	4.4	0.04	35.2	0.64	223.2	401.9	0.4	14.34	63.5	0.57	4.37	4.03	14.3	0.43
7	0.15	3.2	0.13	38.1	0.51	244.8	986	0.3	12.76	61.7	0.56	5.22	14.3	10.7	0.49
8	0.25	5.3	0.10	25.4	0.61	236.7	2021	0.8	14.63	53.9	0.61	3.83	16.7	19	0.27
9	0.13	5.0	0.20	135	0.43	171.3	1320	0.7	12.87	56.3	0.47	4.03	23	21.1	0.21
10	0.3	3.1	0.15	124	0.41	200.7	1268	0.5	12.1	62.3	0.58	5.11	21	20.2	0.2

Synthetic index of soil.

Table 4: Importance of indicators at all levels to objectives.

First level index		Weight	Second level index	Weight
Soil quality indicators	C1	0.393	Pb C1-1	0.319
			Zn C1-2	0.103
			Cd C1-3	0.117
			As C1-4	0.104
			U C1-5	0.357
Water environmental quality	C2	0.385	Pb^{2+} C2-1	0.397
			Zn^{2+} C2-2	0.183
			COD C2-3	0.207
			BOD C2-4	0.213
Atmospheric environmental	C3	0.091	SO_2 C3-1	0.238
			Rn C3-2	0.344
			CO C3-3	0.217
			TSP C3-4	0.201
Ecological compensation indicators	C6	0.131	Input intensity of pollution control C6-1	0.416
			Improvement of ecological early warning system C6-2	0.302
			Environmental protection investment/total income C6-3	0.282

Table 5: The grading standard of the relative importance of the corresponding index to the goal.

Logical variable	Grade corresponding to factor weight ratio
Equally important	0.96
Weakly important	0.8
Fairly important	0.64
Strongly important	0.48
Very strongly important	0.32
Extremely important	0.16

fuzzy variable z, respectively, all of which are real numbers. Then, the three numbers (l, m, u) constitute a triangular fuzzy number, $\tilde{A}$. Let $\tilde{A} = (l, m, u)$ and $l \le m \le u$, and the function diagram of the triangular fuzzy number is shown in Figure 1. The membership function [18] is

$$\varepsilon(z) = \begin{cases} 0 & z < l \\ \dfrac{z-l}{m-l} & l \le z \le m \\ \dfrac{u-z}{u-m} & m \le z \le u \\ 0 & z \ge u \end{cases}, \tag{2}$$

where the parameter m denotes the maximum possible value describing a fuzzy event, and l and u represent the upper and lower bounds of the boundary, respectively.

Table 6: The comparison matrix with respect to the goal.

	Present method			
	C1	C2	C3	C6
C1	(1, 1, 1)	(2/3, 1, 2)	(2, 5/2, 3)	(3/2, 2, 5/2)
C2	(1/2, 1, 3/2)	(1, 1, 1)	(2, 5/2, 3)	(3/2, 2, 5/2)
C3	(1/3, 2/5, 1/2)	(1/3, 2/5, 1/2)	(1, 1, 1)	(2/3, 1, 2)
C6	(2/5, 1/2, 2/3)	(2/5, 1/2, 2/3)	(1/2, 1, 3/2)	(1, 1, 1)

$\lambda = 0.4798$, $M = 1015$.

2.2. Generalized Linear Model Theory. The generalized linear model is a direct extension of the normal linear model, which is suitable for continuous data and discrete data; that is, the independent variable can be a continuous variable, classified variable, or ordered variable. Its basic form can be expressed as

$$\mu_i = E[Y_i] = g^{-1}\left(\sum_j X_{ij}\beta_j + \xi_i\right), \tag{3}$$

where μ_i is the mathematical expectation; Y_i is the dependent variable vector; $g(x)$ is the connection function; X_{ij} is the independent variable matrix; β_j is the model parameter vector to be estimated; and ξ_i is the interference term.

Combined with equation (3), the observed value of the dependent variable can be connected with the expected value of the explanatory variable by linear addition; therefore, the relationship between the mathematical expectation μ_i and the linear factors can be expressed as

$$g(\mu_i) = X_i\beta', \tag{4}$$

where $g(\mu_i)$ is a strictly monotonic function and is differentiable, which is called a continuous function.

The expected value of the observed value of the dependent variable is related to the explanatory variable by equation (4-1). It is assumed that there are N sets of observation data, i.e., $(y|X_i) = (y|x_1, x_2, \cdots, x_k)$ and $(i = 1, 2, \cdots, n)$. $y_i \in (0, 1, \cdots, j)$ is a multicategory dependent variable with j categories, indicating that the conclusion of the safety evaluation model has j grades. $X = (x_1, x_2, \cdots, x_k)$ is the explanatory variable, i.e., the influencing factor affecting the conclusion grade of the model.

It is assumed that ω_i is the cumulative influence weight of a certain level y_i under the condition of the index factor variable

$$\omega_i = \omega(y_i \le j|X_i), \omega_i = \omega_{i+1} - \omega_i, \tag{5}$$

where $\bar{\omega}_i$ is the influence weight of an evaluation level.

To better describe the relationship between the cumulative influence weight of the level and the index factor variables, in this paper, the relationship is transformed by logistic transformation, that is

$$\log it(\omega_i) = \ln\left[\frac{\omega_i(y_i \le j|x_i)}{1 - \omega_i(y_i \le j|x_i)}\right] = \beta_0 + \sum_{i=0}^{k}\beta_i x_i, \tag{6}$$

where the relationship between the logit (ω) transformed and the independent variable is linear, and its value range is (- ∞, + ∞), which is conducive to its estimation.

The regression equation can be obtained by substituting the estimated value of parameter β into equation (6)

$$\omega'\left(y_i \le j\middle|(x_1, x_2, \cdots, x_k)_i\right) = \frac{\exp\left(\beta_0' + \sum_{i=0}^{k}\beta_0' x_i\right)}{1 + \exp\left(\beta_0' + \sum_{i=0}^{k}\beta_0' x_i\right)}. \tag{7}$$

2.3. The Fuzzy Analytic Hierarchy Process. First, the weight value of each index influencing the target value is determined by generalized linear theory, and then the importance of each pair of factors is judged by the weight of each index factor. According to the linguistic variable in Table 1, the relative importance of each pair of factors can be obtained. Then, the comparison matrix $\tilde{U}$ can be created.

$$\tilde{U} = \left(\tilde{u}_{ij}\right)_{n\times n} = \begin{bmatrix} 1 & (l_{12}, m_{12}, u_{12}) & \cdots & (l_{1n}, m_{1n}, u_{1n}) \\ (l_{21}, m_{21}, u_{21}) & 1 & \cdots & (l_{2n}, m_{2n}, u_{2n}) \\ \vdots & \vdots & \vdots & \vdots \\ (l_{n1}, m_{n1}, u_{n1}) & (l_{n2}, m_{n2}, u_{n2}) & \cdots & 1 \end{bmatrix}, \tag{8}$$

where if $i \ne j$, then $\tilde{u}_{ij} = (l_{ij}, m_{ij}, u_{ij}) = \tilde{u}_{ij}^{-1} = (1/u_{ji}, 1/m_{ji}, 1/l_{ji})$, $(i = 1, 2, \cdots, n)$, and $(j = 1, 2, \cdots, n)$.

To facilitate the research, the comparison matrix $\tilde{U}$ is processed by the logarithmic transformation [19, 20]

$$\ln \tilde{u}_{ij} \approx \left(\ln l_{ij}, \ln m_{ij}, \ln u_{ij}\right). \tag{9}$$

By substituting equation (9) into equation (2), the following can be obtained

$$\mu_{ij}\left(\ln\left(\frac{s_i}{s_j}\right)\right) = \begin{cases} 0 & \ln\left(\frac{s_i}{s_j}\right) < \ln l_{ij} \\ \dfrac{\ln\left(s_i/s_j\right) - \ln l_{ij}}{\ln m_{ij} - \ln l_{ij}} & \ln l_{ij} \le \ln\left(\frac{s_i}{s_j}\right) \le \ln m_{ij} \\ \dfrac{\ln u_{ij} - \ln\left(s_i/s_j\right)}{\ln u_{ij} - \ln m_{ij}} & \ln m_{ij} \le \ln\left(\frac{s_i}{s_j}\right) \le \ln u_{ij} \\ 0 & \ln\left(\frac{s_i}{s_j}\right) > \ln u_{ij} \end{cases}. \tag{10}$$

Table 7: The comparison matrix with respect to the soil quality.

	Present method				
	C1-1	C1-2	C1-3	C1-4	C1-5
C1-1	(1, 1, 1)	(2, 5/2, 3)	(3/2, 2, 5/2)	(2, 5/2, 3)	(2/3, 1, 2)
C1-2	(1/3, 2/5, 1/2)	(1, 1, 1)	(2/3, 1, 2)	(2/3, 1, 2)	(1/3, 2/5, 1/2)
C1-3	(2/5, 1/2, 2/3)	(1/2, 1, 3/2)	(1, 1, 1)	(1/2, 1, 3/2)	(2/5, 1/2, 2/3)
C1-4	(1/3, 2/5, 1/2)	(1/2, 1, 3/2)	(2/3, 1, 2)	(1, 1, 1)	(1/3, 2/5, 1/2)
C1-5	(1/2, 1, 3/2)	(2, 5/2, 3)	(3/2, 2, 5/2)	(2, 5/2, 3)	(1, 1, 1)

$\lambda = 0.8200$, $M = 1018$.

Table 8: The comparison matrix with respect to the water environmental quality.

	Present method			
	C2-1	C2-2	C2-3	C2-4
C2-1	(1, 1, 1)	(3/2, 2, 5/2)	(1, 3/2, 2)	(1, 3/2, 2)
C2-2	(2/5, 1/2, 2/3)	(1, 1, 1)	(1/2, 2/3, 1)	(1/2, 2/3, 1)
C2-3	(1/2, 2/3, 1)	(1, 3/2, 2)	(1, 1, 1)	(2/3, 1, 2)
C2-4	(1/2, 2/3, 1)	(1, 3/2, 2)	(1/2, 1, 3/2)	(1, 1, 1)

$\lambda = 0.6230$, $M = 1017$.

Table 9: The comparison matrix with respect to the atmospheric environment.

	Present method			
	C3-1	C3-2	C3-3	C3-4
C3-1	(1, 1, 1)	(2/3, 1, 2)	(1/2, 1, 3/2)	(1, 3/2, 2)
C3-2	(1/2, 1, 3/2)	(1, 1, 1)	(1, 3/2, 2)	(1, 3/2, 2)
C3-3	(2/3, 1, 2)	(1/2, 2/3, 1)	(1, 1, 1)	(1/2, 1, 3/2)
C3-4	(1/2, 2/3, 1)	(1/2, 2/3, 1)	(2/3, 1, 2)	(1, 1, 1)

$\lambda = 0.4819$, $M = 1015$.

In this paper, to solve the problem that a specific value λ results in an inconsistency between weights and fuzzy judgements in U, the nonnegative deviation parameters of γ_{ij} are introduced [17, 18].

$$\begin{aligned} &Minimize K = (1-\lambda)^2 + G\sum_{i=1}^{n-1}\sum_{j=i+1}^{n}\left(\gamma_{ij}+\varsigma_{ij}\right)^2 S.t. \\ &\cdot\begin{cases} \ln s_i - \ln s_j - \lambda \ln\left(\dfrac{m_{ij}}{l_{ij}}\right) + \gamma_{ij} \geq \ln l_{ij} \\ i = 1, \cdots, n-1\,; j = i+1, \cdots, n \\ -\ln s_i + \ln s_j - \lambda \ln\left(\dfrac{u_{ij}}{m_{ij}}\right) + \varsigma_{ij} \geq -\ln u_{ij} \\ i = 1, \cdots, n-1\,; j = i+1, \cdots, n \\ \lambda \geq 0, y_i \geq 0, i = 1, \cdots, n-1 \\ \gamma_{ij} \geq 0, \varsigma_{ij} \geq 0, i = 1, \cdots, n-1\,; j = i+1, \cdots, n \end{cases}, \end{aligned} \tag{11}$$

Table 10: The comparison matrix with respect to ecological compensation.

	Present method		
	C6-1	C6-2	C6-3
C6-1	(1, 1, 1)	(1/2, 1, 3/2)	(1, 3/2, 2)
C6-2	(2/3, 1, 2)	(1, 1, 1)	(1/2, 1, 3/2)
C6-3	(1/2, 2/3, 1)	(2/3, 1, 2)	(1, 1, 1)

$\lambda = 0.6017$, $M = 1012$.

where G is a specific constant, which is used to determine the weights in the fuzzy judgements.

The normalized priority calculation of the fuzzy pairwise comparison matrix $\tilde{U}$ can be expressed by

$$\omega_i^* = \frac{\exp\left((\ln s_i)^*\right)}{\sum_{j=1}^{n}\exp\left((\ln s_j)^*\right)}. \tag{12}$$

3. Application

3.1. Determination of Index Factors. According to the survey, the main indicators affecting the ecological safety of coal mines are atmospheric environmental indicators, water environmental quality indicators, soil quality indicators, geological hazard damage indicators, waste disposal indicators of coal mines, and ecological compensation indicators of coal mines. Among them, atmospheric environmental indicators mainly include factors affecting atmospheric environmental safety, e.g., TSP, CO, SO_2, and radon. Water environmental quality indicators mainly include the concentrations of Pb, Zn, COD, and BOB. Soil quality indicators mainly refer to the concentrations of coal, lead, cadmium, zinc, and arsenic. The index of the degree of destruction of geological hazards mainly refers to the proportion of all kinds of geological hazards in the total area of mines, i.e., the impact scale of landslides, collapses, and land subsidence. The waste disposal indexes of coal mines mainly include slag disposal and waste liquid controlled discharge. The ecological compensation index of coal mines includes the input intensity of pollution control, the perfection of ecological early warning mechanisms, and the proportion of environmental protection input to mine income.

3.2. Determine the Weights of the Responding Index Factors. The decision problem in the hierarchical structure is decomposed, as shown in Figure 2. The hierarchy consists of three levels, including goals, criteria and alternatives. This goal

Table 11: The priorities of risk factors to the coal mine.

Factors	Local weight	Global weight	Ranking
Soil quality C1		0.6655	I
Concentration of coal C1-1	0.4521	0.3009	1
Concentration of lead C1-2	0.1481	0.0986	4
Concentration of cadmium C1-3	0.1827	0.1215	3
Concentration of zinc C1-4	0.1085	0.0722	6
Concentration of arsenic C1-5	0.1086	0.0723	5
Water environmental quality C2		0.2293	II
Concentration of Pb C2-1	0.7002	0.1606	2
Concentration of Zn C2-2	0.1339	0.0308	8
Concentration of COD C2-3	0.1060	0.0242	9
Concentration of BOB C2-4	0.0599	0.0137	11
Atmospheric environment C3		0.0679	III
Concentration of TSP C3-1	0.7754	0.0526	7
Concentration of CO C3-2	0.1871	0.0127	12
Concentration of SO2 C3-3	0.0322	0.0022	15
Concentration of radon C3-4	0.0053	0.0004	16
Ecological compensation indicators C6		0.0373	IV
Input intensity of pollution control C6-1	0.3790	0.0141	10
Perfection of ecological early warning mechanism C6-2	0.3313	0.0124	13
Proportion of environmental protection input to mine income C6-3	0.2896	0.0108	14

Table 12: The consistency of each fuzzy comparison matrix.

Hierarchy	Consistency λ
Soil quality indicators (Table 7)	0.8200
Water environmental quality (Table 8)	0.6230
Atmospheric environment (Table 9)	0.4819
Ecological compensation indicators (Table 10)	0.6017

layer is mainly used to assess the ecological environmental risk of coal mines. The criteria and alternatives are located at the second level and the third level, respectively.

The ecological environment monitoring data of several typical coal mines in China are selected to evaluate the ecological environmental safety. The ecological compensation index is generally calculated by comprehensively considering the benefits of the mine, the income expectations of leaders and miners, and the laws and regulations. The data of influencing factors of air, soil, and water indexes are mainly collected from the concentration of some harmful substances specified in relevant national standards. Based on the analysis of the evaluation indexes of the coal mine according to references [21–26], the ecological safety compensation index value and the index factor index value of air, soil, and water indexes of the coal mine are obtained, as shown in Tables 2 and 3.

The cumulative influence weight of the corresponding grade of the first level indicator and the influence weight of each grade under the second level indicator factor are obtained through the analysis of the generalized linear model (the influence weight of each grade indicator is mainly obtained through the Statistical Analysis System (SAS), as shown in Table 4), and then the maximum value of the influence weight of each grade is taken as the influence weight of the corresponding category. The weight of each index factor is used to judge the relative importance of each index factor. The maximum likelihood ratio of each category is 42.684, 35.033, 43.556, and 41.022, respectively, all of which are within the allowable error range, indicating that the generalized linear model has a good fit.

The influence weight of the grade corresponding to the second level index and its corresponding first level index is analyzed through the generalized linear model, and the comparison matrix of the first level index and the second level index can be obtained according to Table 5, as shown in Tables 6–10.

4. Results and Discussion

4.1. Results. The results of local and global weights on the environmental impact factors of coal mines obtained by the present evaluation model based on the generalized linear and fuzzy analytic hierarchy process are shown in Table 11, which shows that the soil quality has the most important index influence on the environmental risk of coal mines among the four influencing factors, followed by water environmental quality, atmospheric environment, and ecological compensation indicators. Therefore, it is necessary to monitor the dangerous elements in soil and water on a regular basis and take timely measures to prevent exceeding the standard to control the dangerous sources during the early risk stage.

Table 13: The priorities of risk factors to the coal mine [27].

Factors	Local weight	Global weight	Ranking
Soil quality C1		0.478	I
Concentration of coal C1-1	0.5588	0.2671	1
Concentration of lead C1-2	0.0967	0.0462	6
Concentration of cadmium C1-3	0.2219	0.1061	3
Concentration of zinc C1-4	0.0663	0.0317	9
Concentration of arsenic C1-5	0.0563	0.0269	10
Water environment quality C2		0.363	II
Concentration of Pb C2-1	0.6903	0.2506	2
Concentration of Zn C2-2	0.1493	0.0542	5
Concentration of COD C2-3	0.1118	0.0406	7
Concentration of BOB C2-4	0.0485	0.0176	13
Atmospheric environment C3		0.0831	III
Concentration of TSP C3-1	0.7449	0.0619	4
Concentration of CO C3-2	0.2358	0.0196	12
Concentration of SO2 C3-3	0.0168	0.0014	15
Concentration of radon C3-4	0.0025	0.0002	16
Ecological compensation indicators C6		0.0759	IV
Input intensity of pollution control C6-1	0.4598	0.0349	8
Perfection of ecological early warning mechanism C6-2	0.3083	0.0234	11
Proportion of environmental protection input to mine income C6-3	0.2319	0.0176	14

In addition, Table 11 shows that the concentration of coal (C1-1), concentration of Pb (C2-1), concentration of cadmium (C1-3), and concentration of lead (C1-2) have a great influence on the environmental risk of coal mines. However, the perfection of an ecological early warning mechanism (C6-2), proportion of environmental protection input to mine income (C6-3), concentration of SO_2 (C3-3), and concentration of radon (C3-4) have little influence on the environmental risk of coal mines. Table 11 also reveals that the environmental investment management of coal mines in the later stage has little impact on the environmental assessment. This result is mainly because in the later stage, the environment of coal mines has caused many irreversible losses and has had many human and financial costs. From a sustainable point of view, the compensation and management of the mine environment in the later period are definitely not a good long-term strategy.

4.2. Verification of the model's Validity. According to the literature, the validity of a model is usually verified by calculating the value of consistency and the nonnegative deviation variable of the fuzzy pairwise comparison matrices, i.e., the consistency λ and nonnegative deviation variable γ are the key parameters to determine the validity of a model. There are two cases in which $\lambda = 0$ and $\lambda \neq 0$. When λ is not equal to zero, the greater the value of parameter λ is, the better the consistency of the model is. When λ is equal to zero, if $\gamma = 0$, the consistency of the model is still good. If $\gamma \neq 0$, it indicates that the model is inconsistent. The greater the nonnegative deviation variable γ is, the worse the consistency of the model is. With the help of MATLAB software, the value of λ in every matrix is obtained, as shown in Table 12. From the consistency index aspect, the proposed model is confirmed to be acceptable.

In the second perspective, we compare the results of the present method we used in this paper with the results of the representative comprehensive evaluation method [27]. The results of the representative comprehensive evaluation method are shown in Table 13. We have obtained similar results on some factors. In particular, the impact of the first level index factors on the safety environment of uranium mines is basically the same. From all above, the proposed model was proven to be valid.

4.3. Advantages and Disadvantages of the Present Model. Based on generalized linear theory, the influence value of index factors on the environmental evaluation of coal mines was obtained using SAS software to count the original data of the index factors. Then, the fuzzy pairwise comparison matrices were established according to the influence value of index factors on the environmental evaluation, which greatly reduced the influence of human subjectivity on the construction of the comparison matrix. In addition, the linguistic variables and the TFN were introduced in the process of solving the factor weight, which enabled managers to quickly determine the relative importance of each pair of factors through the linguistic variables.

However, in the present model, although the importance degree of each factor was obtained using a linear generalized model to count the original data of each factor, the relative importance degree of each factor was judged by experts. Therefore, it is urgent to establish an evaluation formula and basis for the relative importance degree of each factor. In addition, according to the literature, although the

comparison matrices are consistent, the fuzzy number of the comparison matrix can lead to inconsistent results to some extent.

5. Conclusions

This paper develops a comprehensive environmental evaluation model of coal mines based on generalized linear theory and fuzzy analytic hierarchy processes.

(1) The model is consistent with the results of literature [27] and let the evaluation process more efficient

(2) In this paper, the linguistic variables are a kind of variable whose values are not numbers but words or sentences, and they are closer to the feelings of the decision makers. Therefore, the present model can effectively solve the problem of multiclassification in safety evaluations

(3) In addition, in the environmental evaluation model, based on prior knowledge of the sample statistical source, the importance degree of each index factor on the environmental factor index is preliminarily obtained through generalized linear theory, and the influence weight value of each index factor was accurately obtained based on the logarithmic fuzzy preference programming method, which overcomes the defect of artificial empowerment and has more accurate evaluation results

Data Availability

The data used to support the findings of this study are included within the article.

Conflicts of Interest

The authors declare that they have no conflicts of interest.

Acknowledgments

This work was supported by the Postdoctoral research projects in Henan Province (201901012), the National Key Research and Development Program of China (No. 2017YFC1501204), the National Basic Research Program of China (No. 2015CB060200), the National Natural Science Foundation of China (No. 51678536, 41404096), the Program for Science and Technology Innovation Talents in Universities of Henan Province (Grant No. 19HASTIT043), the Outstanding Young Talent Research Fund of Zhengzhou University (1621323001), and the Program for Innovative Research Team (in Science and Technology) in University of Henan Province (18IRTSTHN007). We would also like to acknowledge the reviewers for their invaluable comments.

References

[1] L. Dong, X. Tong, X. Li, J. Zhou, S. Wang, and B. Liu, "Some developments and new insights of environmental problems and deep mining strategy for cleaner production in mines," *Journal of Cleaner Production*, vol. 210, pp. 1562–1578, 2019.

[2] A. M. R. Neiva, P. C. S. Carvalho, I. M. H. R. Antunes et al., "Assessment of metal and metalloid contamination in the waters and stream sediments around the abandoned uranium mine area from Mortórios, Central Portugal," *Journal of Geochemical Exploration*, vol. 202, pp. 35–48, 2019.

[3] L. Dong, D. Sun, W. Shu, and X. Li, "Exploration: safe and clean mining on earth and asteroids," *Journal of Cleaner Production*, vol. 257, article 120899, 2020.

[4] Y. Zhao, "Study and applications of analytic hierarchy process of mine geological environment: a case study in Hainan Island," *Remote Sensing for Land and Resources*, pp. 1–9, 2020.

[5] A. Bascetin, "A decision support system using analytical hierarchy process (AHP) for the optimal environmental reclamation of an open-pit mine," *Environmental Geology*, vol. 52, no. 4, pp. 663–672, 2007.

[6] C. Samantra, S. Datta, and S. Mahapatra, "Analysis of occupational health hazards and associated risks in fuzzy environment: a case research in an Indian underground coal mine," *International Journal of Injury Control and Safety Promotion*, vol. 24, no. 3, pp. 311–327, 2016.

[7] M. Yang, L. Liu, and G. Gao, "Application of fuzzy synthesis evaluation to the environmental influence of the west-mineral exploration," *Journal of Xi'an University of Science and Technology*, vol. 26, no. 4, pp. 439–442, 2006.

[8] X. Su, F. Cheng, S. Guo, and J. Zhou, "Evaluation model of mine engineering geological conditions based on grey mathematics theory," *Mining Technology*, vol. 16, no. 5, pp. 87–89, 2016.

[9] W. Zhao, M. Xu, J. Zhang, and S. Qi, "Application of BP neural network in mine ecological security evaluation," *Coal Technology*, vol. 38, no. 1, pp. 172–175, 2019.

[10] Z. Chen, J. Wu, Y. Guo, and T. Lin, "Application of AHP and fuzzy mathematics in comprehensive assessment of mine environment," *East China Geology*, vol. 39, no. 4, pp. 305–310, 2018.

[11] D. Wei, C. Du, Y. Lin, B. Chang, and Y. Wang, "Thermal environment assessment of deep mine based on analytic hierarchy process and fuzzy comprehensive evaluation," *Case Studies in Thermal Engineering*, vol. 19, article 100618, 2020.

[12] L. Dong, W. Shu, X. Li, Z. Zhou, F. Gong, and X. Liu, "Quantitative evaluation and case study of risk degree for underground Goafs with multiple indexes considering uncertain factors in mines," *Geofluids*, vol. 2017, Article ID 3271246, 15 pages, 2017.

[13] L. Dong and X. Li, "Comprehensive models for evaluating rockmass stability based on statistical comparisons of multiple classifiers," *Mathematical Problems in Engineering*, vol. 2013, Article ID 395096, 9 pages, 2013.

[14] Y. Wei, G. Tong, and Z. Ji, "Fuzzy hierarchy analysis model for the mine management based on grey correlation degree," *China Molybdenum Industry*, vol. 19, no. 3, pp. 28–32, 1995.

[15] F. Liu, *Research on the Combination Evaluation Model of Mine Geological Environment Based on Grey Correlation Degree, AHP and Fuzzy*, Chang'an University, 2014.

[16] T. Padma and P. Balasubramanie, "A fuzzy analytic hierarchy processing decision support system to analyze occupational menace forecasting the spawning of shoulder and neck pain," *Expert Systems with Applications*, vol. 38, no. 12, pp. 15303–15309, 2011.

[17] Q. Wang, H. Wang, and Z. Qi, "An application of nonlinear fuzzy analytic hierarchy process in safety evaluation of coal mine," *Safety Science*, vol. 86, pp. 78–87, 2016.

[18] M. Naghadehi, R. Mikaeil, and M. Ataei, "The application of fuzzy analytic hierarchy process (FAHP) approach to selection of optimum underground mining method for Jajarm bauxite mine, Iran," *Expert Systems with Applications*, vol. 36, no. 4, pp. 8218–8226, 2009.

[19] L. Zadeh, "The concept of a linguistic variable and its application to approximate reasoning," *Learning Systems and Intelligent Robots*, vol. 8, pp. 199–249, 1974.

[20] M. Dağdeviren and I. Yüksel, "Developing a fuzzy analytic hierarchy process (AHP) model for behavior-based safety management," *Information Sciences*, vol. 178, no. 6, pp. 1717–1733, 2008.

[21] Y. Zhang, "Ecological security evaluation and policy suggestions of coal industry in China," *Theory Monthly*, vol. 2, pp. 163–165, 2011.

[22] F. Zhang, *Assessment on Wetland Ecosystem Based on 3S Image-Taking the Heihe Rivesource Qilian Mountains as an Example*, Qinghai Normal University, Xining, 2011.

[23] K. Yang, "Application of fuzzy mathematics in mine environmental impact assessment," *Sichuan Environment*, vol. 29, no. 3, pp. 127–130, 2010.

[24] GB 3095-2012, "Ambient air quality standard," http://www.cssn.net.cn/cssn/front/listpage.jsp.

[25] GB 15618-1995, "Soil environmental quality standard," http://www.cssn.net.cn/cssn/front/listpage.jsp.

[26] GB 3838-2002, "Environmental quality standard for surface water," http://www.cssn.net.cn/cssn/front/listpage.jsp.

[27] L. Dong, W. Shu, X. Li, and J. Zhang, "Quantitative evaluation and case studies of cleaner mining with multiple indexes considering uncertainty factors for phosphorus mines," *Journal of Cleaner Production*, vol. 183, pp. 319–334, 2018.